# Discrete Element Model Simulations of Failure Processes of Cohesive Granular Material

**Yuta Yamaguchi**

A thesis submitted in partial fulfilment of the requirements of Nottingham Trent University for the degree of Doctor of Philosophy

October 8, 2022

# Abstract

Granular materials, such as powder and sand, are all around us and are studied in engineering, industry and many other fields. For example, the rheological behaviour of rocks and soils are important in geology. Similarly, predicting internal deformation and failure of building materials consisted of granular particles is important in civil engineering. This thesis focuses on how emergent phenomena, such as shear failure, compaction failure or cluster formation in granular materials can be captured in a minimal model. In particular, I explore the effects of cohesion when an external force is applied to a granular aggregate, using discrete element model (DEM) simulations. I deal with two types of cohesiveness. The first project investigates cemented cohesive aggregates, which include solid, brittle bonds between grains, simulating porous rocks. While constraining all the simulation parameters by related experiments, I succeed in reproducing and extending the experimental observations on this material's mechanical response to uniaxial compression. Then, I explore its failure processes, applied to brittle, ductile and low-density materials. I also show how machine learning can predict the failure timing of the material. The second project addresses the rheology of cohesive granulates. I investigate the effects of density and cohesion strength for a granular system under a constant pressure condition and shear deformation, by a combination of 2D and 3D simulations. Both simulations show cluster formation and shear localisation due to cohesion, and suggest that these phenomena are intrinsic to cohesive granular materials. I also measure a decrease in shear stress accompanying cluster formation. Finally, I also identified the existence of a critical nuclei size for cluster formation. Generally, this work together shows the strengths of a minimal, experimentally-informed model that can reproduce the emergent phenomena of cohesive granular materials and identify the key physical quantities that control these phenomena.

# Acknowledgments

I would like to express my sincere gratitude to my supervisor, Lucas Goehring, for his warm guidance and encouragement throughout this research. Despite being PhD student at distance, I receive tremendous advice and can summarise my research activities at the University of Tokyo and Osaka University as this thesis. I would also like to thank Soumyajyoti Biswas for supporting my research as a teaching team. During my internship at Max Planck Institute, he not only supported my research but also took care of my daily life, for which I am sincerely grateful.

I want to thank Arnaud Hemmerle for sharing his experimental results. His work on cohesive granular material inspire my research on modelling the cemented granular system in this thesis.

I want to thank Sumanta Kundu and Anca Opris and acknowledge the daily discussion during my stay at Osaka University. I would also like to thank Takahiro Hatano for giving me the freedom to focus on my research activities.

I want to thank Satoshi Takada for his great help in my master's work and for teaching me much knowledge about the scientific input to my work on shear simulations of cohesive granular particles under a constant pressure. I would like to express my deepest gratitude to him.

Finally, I would like to express my deepest gratitude to my family members and friends for their support.

# List of Publications

## Published Papers

Yuta Yamaguchi, Satoshi Takada, and Takahiro Hatano. Rheology of cohesive granular particles under constant pressure. *Journal of the Physical Society of Japan*, **87**, 094802, 2018.

Yuta Yamaguchi, Soumyajyoti Biswas, Takahiro Hatano, and Lucas Goehring. Failure processes of cemented granular materials, *Physical Review E*, **102**, 052903, 2020.

Arnaud Hemmerle*, Yuta Yamaguchi*, Marcin Makowski, Oliver Bäumchen, and Lucas Goehring. Measuring and upscaling micromechanical interactions in a cohesive granular material. *Soft Matter*, **17**, 5806–5814, 2021.

*These authors contributed equally to this study.

# Table of Contents

# List of Figures

# List of Symbols

| | | |
|---|---|---|
| $d$ | diameter of a cohesive bond | m |
| $D$ | bead diameter | m |
| $e_n$ | restitution coefficient | |
| $E_g$ | shear modulus of PDMS | N m$^{-2}$ |
| $E_p$ | Young's modulus of PDMS | N m$^{-2}$ |
| $F^{\mathrm{c}}$ | contact force | N |
| $F^{\mathrm{diss}}$ | dissipative force | N |
| $F^n$ | translational inter-particle force | N |
| $\boldsymbol{F}^t$ | tangential inter-particle force | N |
| $G$ | surface energy | N m$^{-1}$ |
| $h$ | time increment | s |
| $H$ | system height | m |
| $I$ | non-dimensionalised shear rate | |
| $I_i$ | moment of inertia | kg m$^2$ |
| $k_n^{\mathrm{bond}}$ | spring constant of a cohesive bond, normal | N m$^{-1}$ |
| $k_n^{\mathrm{glass}}$ | spring constant of a glass bead, normal | N m$^{-1}$ |
| $k_t^{\mathrm{bond}}$ | spring constant of a cohesive bond, shear | N m$^{-1}$ |
| $k_t^{\mathrm{glass}}$ | spring constant of a glass bead, shear | N m$^{-1}$ |
| $l_{ij}$ | height of a cohesive bond | m |
| $m$ | bead mass | kg |
| $\boldsymbol{n}$ | normal unit vector | |
| $N$ | number of broken bonds | |
| $P$ | normal pressure | N m$^{-2}$ |
| $q_i$ | fraction of microcracks | |
| $\boldsymbol{r}$ | position of bead | m |
| $R$ | system radius | m |
| $R_{gp}$ | ratio between spring constants | |
| $S$ | normalised configuration entropy | |
| $S_0$ | equipartition entropy | |
| $t$ | time unit | s |
| $u$ | strength of cohesive force | |

| | | |
|---|---|---|
| $U$ | inter-particle potential | N m |
| $U_n$ | strain energy in the normal direction | N m |
| $U_s$ | energy needed to peel a bond | N m |
| $U_t$ | strain energy in the shear direction | N m |
| $\boldsymbol{v}$ | relative velocity of particles | m $s^{-2}$ |
| $V$ | volume of a cohesive bond and shear velocity | $m^3$ and m $s^{-1}$ |
| $\tilde{V}$ | volume of Voronoi cell | $m^3$ |
| $W$ | matrix content | |
| $W^*$ | critical value of matrix content | |
| $x, y, z$ | Cartesian coordinates | m |
| $Z$ | coordination number | |
| $\dot{\gamma}$ | shear rate | $s^{-1}$ |
| $\delta^0$ | surface distance | m |
| $\delta^n$ | overlap distance in normal direction | m |
| $\delta^t$ | overlap distance in tangential direction | m |
| $\Delta$ | integrated mean displacement | m |
| $\epsilon$ | energy unit | kg $m^2$ $s^{-2}$ |
| $\epsilon_n$ | normal strain | |
| $\epsilon_t$ | shear strain | |
| $\zeta$ | dissipation rate | kg $s^{-1}$ |
| $\mu$ | friction coefficient | |
| $\mu_c$ | friction coefficient at zero shear-rate limit | |
| $\sigma$ | normal stress | N $m^{-2}$ |
| $\sigma_p$ | peak stress | N $m^{-2}$ |
| $\nu$ | Poisson ratio | |
| $\phi$ | packing fraction | |
| $\phi_l$ | local packing fraction | |
| $\boldsymbol{\omega}$ | angular velocity | $s^{-1}$ |

# Chapter 1

# Introduction

## 1.1 Emergent phenomena in cohesive granular materials

Given the ubiquity of granular particles, such as grains, flour, and sand, granular physics has been one of the leading research topics of non-linear physics for decades [1–3]. Granular particles are many-body systems of numerous discrete particles, and they have specific effects that cannot be described by continuum mechanics, for example, Reynolds dilatancy, by which the volume of a system increases under shear [4]. In particular, the energy dissipation, which occurs when particles are in contact, is a characteristic feature of granular materials, making the system dissipative. There exists a critical density that represent a state that has characteristics of either a solid or liquid, depending on conditions [5]. Below the critical density, the granular system behaves like a liquid. Above it, the system behaves as solid. As many of these responses have been found to be surprisingly generic, the study of granular media has become the basis for gaining understanding of a wide variety of more complex systems.

Under certain conditions, cohesion can generate non-negligible forces between granular particles. For example, there are at least three origins of cohesive forces: van der Waals forces [6–8], capillary forces on wetted granular particles [9–14], and Coulomb interactions with different electric charges [15]. The van der Waals force only becomes dominant for particle diameters less than a few microns, such as atoms, molecules, ions and even fine cohesive powders [8]. Modellings of fine powders have been done by Refs. [6–8] for example. In contrast, cohesive forces acting between wetted particles appear only when the particles are slightly moistened. However, as the water content increases, the system tends to be approximated instead by the two-phase flow of powder and liquid, and the cohesive interactions cease to act. Detailed theoretical modelling has been developed for weakly wetted particles [9, 11].

Cohesive granular materials can be observed in many fields at a wide range of scales, such as sandstone, nests of birds [16], snow [17], and sintered glass [18] (see Fig. 1.1). The mechanical behaviour of these materials depends on the local contacts between their components [16, 19–21]. When cohesive granular materials experience an external deformation, there have been observed various emergent phenomena. Typical examples under compressive deformation are brittle failure

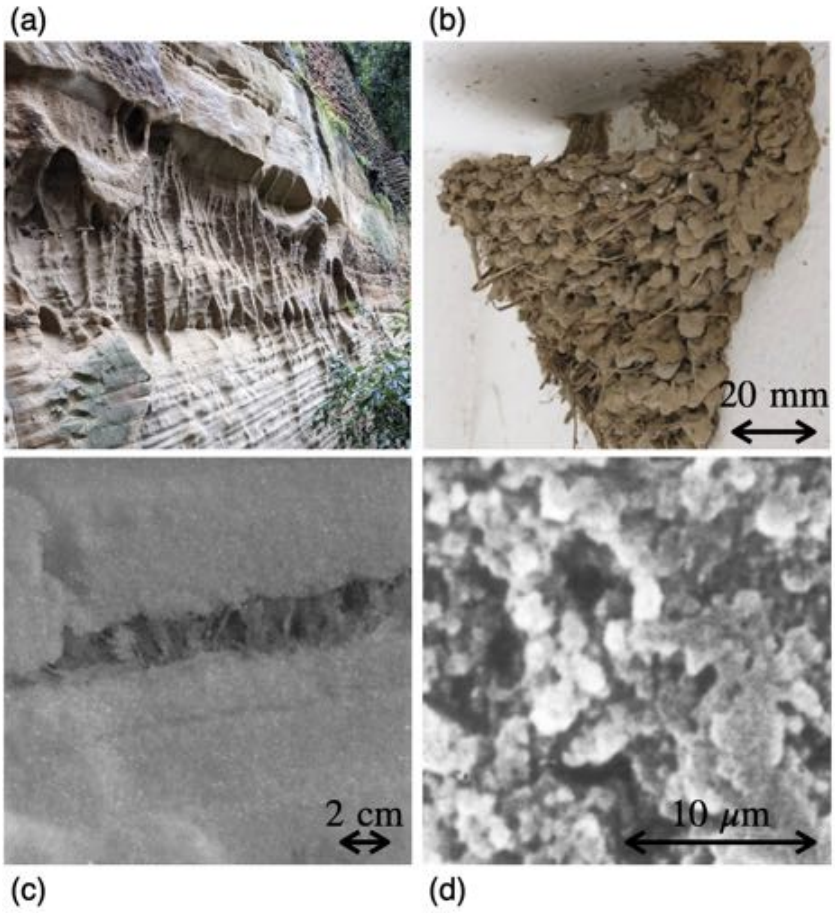


Figure 1.1: Examples of cohesive materials: (a) sandstone at Nottingham Castle (copyright by Lucas Goehring), (b) avian mud nest [16], (c) interface layer of seasonal snow [17], and (d) sintered glass [18].

in sandstone, ductile failure in marble or metal, and compaction banding in snow or porous rock. I show snapshots of these failure modes in Fig. 1.2. In these materials, stress localisation due to damage [22] and damage scattering due to disorder [23] determine the fracture mode. For example, the porosity of a system can control how the cohesive granular system fails [17, 24–26].

As another example, emergent phenomena of cohesive granular materials under shear have also been reported. Through a numerical work, Ref. [30] showed the formation of clusters of granular particles and the occurrence of dilatancy as the cohesion increases, as shown in Fig. 1.3(c). They also observed that strong cohesion causes a decrease in the homogeneity of the system and shear localisation, as shown in Fig. 1.3(d).

In this thesis, I will explore some examples of emergent phenomena in cohesive granular materials. More specific elements of literature review will be discussed in each of the following chapters.

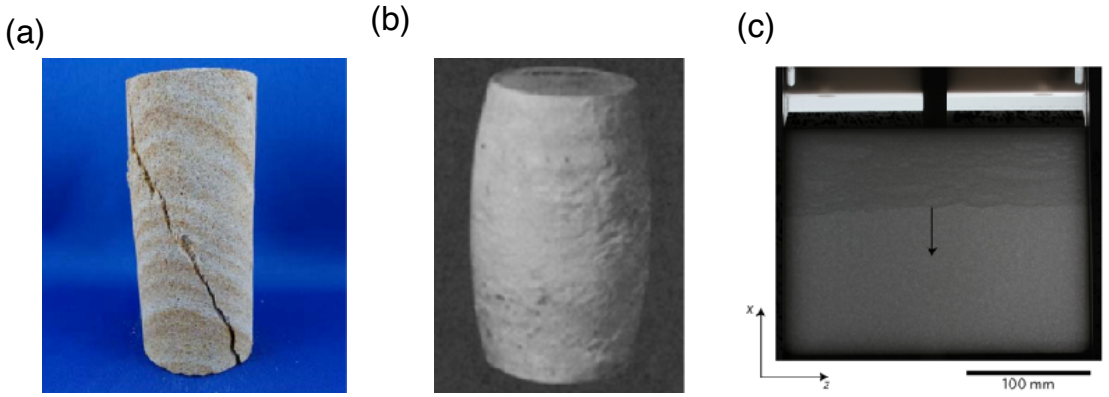


Figure 1.2: Emergent phenomena of cohesive granular materials under compression: (a) brittle failure with a shear band [27], (b) ductile failure in marble [28], and (c) compaction band in artificial snow [29].

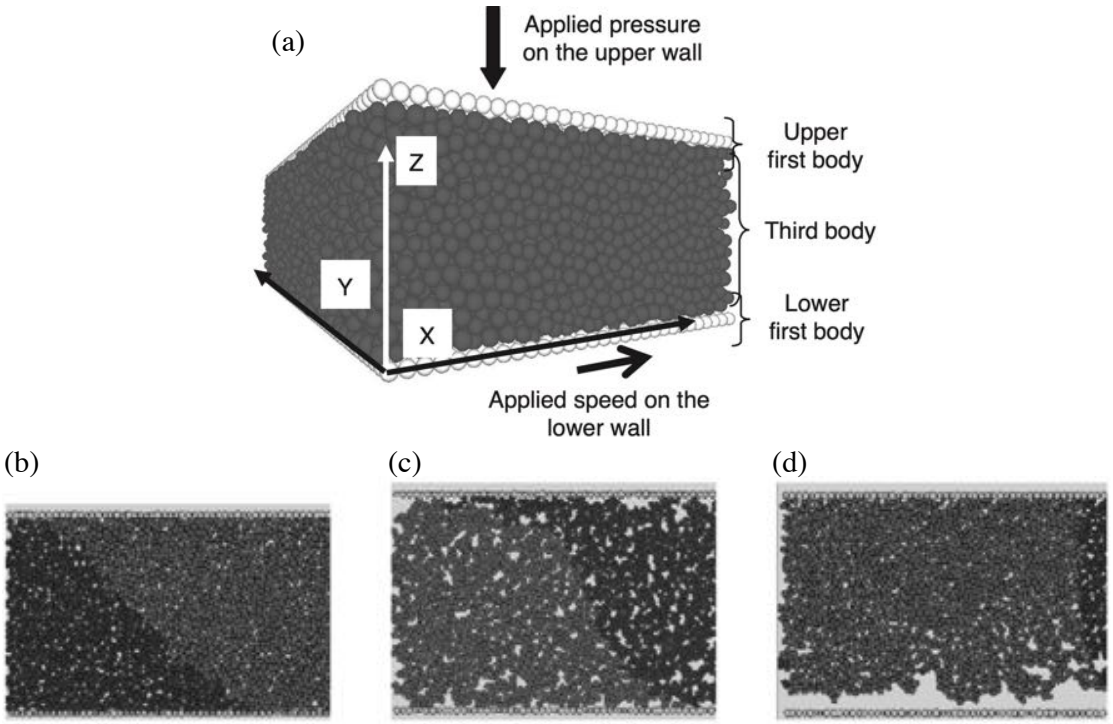


Figure 1.3: (a) 3D shear simulation at constant pressure with a simplified cohesion model: (b) uniform shear deformation with a weak cohesion, (c) dilatancy with a medium cohesion, and (d) shear localisation with a strong cohesion cases. This figure is reproduced from Ref. [30].

## 1.2 Cemented granular materials

In Chapter 3, I will consider a cemented granular system, which is consisted of densely packed granular particles attached to each other by solid bonds. Some related systems have been studied

in the past decade [31–35]. As a particularly innovative case, Ref. [16] studied a familiar system of cemented granular system: they measured the mechanical strength of the mud nests of birds, which are constructed from mud granules attached by saliva. They also made an artificial nest by a 3D printer, and then compared the stiffness between natural and artificial nests. Artificial cemented granular systems have also been created and investigated for their mechanical and fracture properties in uniaxial compression tests in laboratory experiments [36–39] and simulations [40, 41].

Relevant to the work I will discuss in Chapter 3, Ref. [36] developed a cemented granular system using aluminium rods attached by epoxy and investigated the stress-strain curve and failure process of the system under uniaxial compression tests. They also performed DEM simulations to reproduce the experiments and compared their results in terms of the Mohr-Coulomb failure criterion. Ref. [37] built on this work and modelled a cemented granular system by silicone particles bonded with joint seal paste and measured the stress-strain relationship. By changing the volume fraction of matrix, they investigated the effects of the volume of matrix contents on the compressive strength and showed a linear relation between them.

For this kind of material, the DEM simulation technique is a good candidate to see the internal fracture mechanics and their statistics. For example, Refs. [40,41] have used 3D DEM simulations to model cemented granular systems. They observed the mechanical properties and brittle failure of the system under uniaxial compression tests. In particular, their particles are glued together by beams to construct a cemented granular system. They also measured the statistics of the broken beams. They defined the event size of the breaking events as the summation of the breaking energy of the beams and quantitatively compared the event size distribution with the statistical law of earthquakes (i.e. Gutenberg–Richter law). I will develop on these ideas in the DEM simulations presented in this thesis.

Furthermore, recent studies on a cemented granular system have addressed how changes in the mechanical properties of the microscopic matrix content affect the mechanical properties of the whole macroscopic system [38, 39]. As work that directly inspired models in this thesis, Ref. [38] constructed an artificial cemented granular system consisting of glass beads and polymer bonds (PDMS) between beads (see Fig. 1.4(a)). The mechanical response of the system under uniaxial compression is controlled by the elastic properties of the matrix bonds between glass beads. By controlling the composition of the bonds, they adjusted the stiffness of the polymer bonds, and consequently succeeded in changing the hardness of the whole system. They also observed a failure process of the system. When a large strain is applied, the system experiences brittle failure accompanied by shear bands, as shown in Fig. 1.4(b). In a subsequent paper of Ref. [39], the same group carried out experiments to investigate the fracture toughness of the

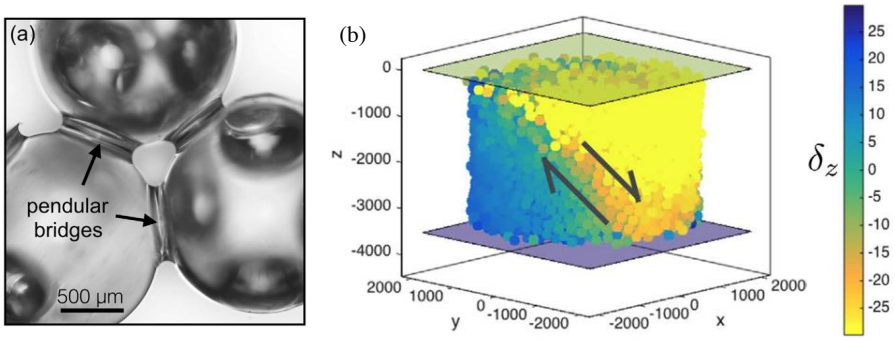


Figure 1.4: Motivating experimental results: (a) Glass beads are connected by polymer bonds (PDMS). (b) Schematic diagram of brittle failure of a larger block of this material via a shear-banding. The colour map shows the relative vertical displacements $\delta_z$ under a uniaxial compression test. This figure is reproduced from Ref. [38].

same artificial cemented granular system. They showed that they could control the fracture toughness of the system by more than one order of magnitude through adjusting the polymer bond stiffness. In addition, they investigated the details of the bond breaking during the failure process by using X-ray tomography.

As mentioned above, previous studies have investigated artificial systems including granular particles bonded with matrix contents and have measured their macroscopic mechanical properties. Beside this work, the microscopic fracture behaviour has also been measured through DEM simulations [40, 41]. Furthermore, in recent studies, the relationship between the mechanical properties of the matrix content and the elastic response of the whole systems has been investigated [38, 39]. The flexibility of the system to reproduce a wide range of elastic moduli by modifying the mechanical properties of the matrix content suggests that it can simulate a wide range of phenomena, not just brittle failure. Numerical representation of the system and its subsequent parameter studies will allow us to extend the applicability of the system and this is a major aim of this thesis. Furthermore, it is possible to investigate the correlation between the microscopic fracture and the catastrophic failure of the system by defining the bond rupture as a microscopic fracture within the system, as in previous studies [40, 41]. In Sec. 3.1, I will develop a DEM simulation for this artificial cemented granular system, based on experimental results on the elastic properties and fracture behaviour of two particles adhered to each other through a polymer bond. The developed model can reproduce the relationship between the elastic modulus of the matrix content and the elastic response of the system, as confirmed by the experiments. Furthermore, in Sec. 3.2, beyond reproducing the experimental observations through simulations, I will perform a parameter study on the density of the system to see and

show a variety of emergent phenomena from this kind of material.

## 1.3 Rheology of cohesive granular materials

The rheology or flow of granular particles is one of the main research topics in granular physics. Rheological behaviour of granular particles can be observed in nature, for example, earthquake faults. In practice, field observations can only show the results of a dynamical process of granular flow. Similarly, laboratory experiments cannot track each motion and deformation of all the granular particles in the many-body system. To track the time evolution of individual particles at a particle level, DEM is a powerful tool.

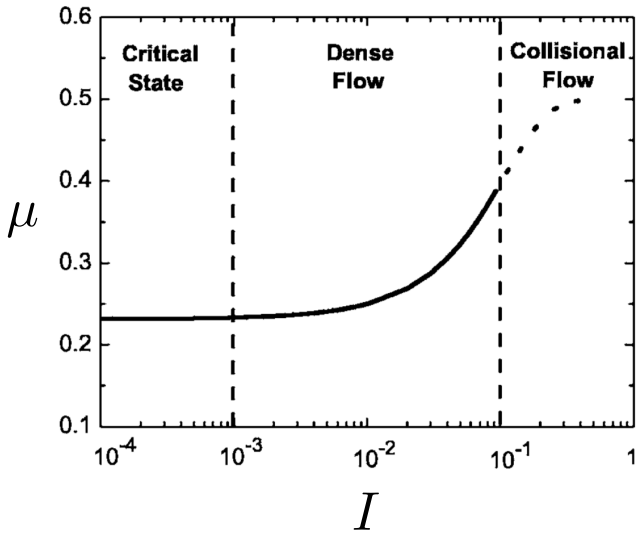


Figure 1.5: Rheology of hard disks under shear deformation and constant pressure conditions. The $\mu$-$I$ curve with the friction coefficient $\mu$, which is defined as the ratio of the shear stress to the pressure inside the material, and the non-dimensionalised shear rate $I$ have three regimes: critical state, dense flow, and collisional flow, depending on $I$. This figure is reproduced from Ref. [42].

Previous studies on granular rheology of hard disks at a constant pressure have been made [42–44]. For example, three regimes appear depending on a non-dimensional shear rate $I(\propto \dot{\gamma}/\sqrt{P})$ described by the shear rate $\dot{\gamma}$ and the normal pressure $P$ [42]; (1) collisional flow, where the friction coefficient has a constant value, at the high shear rate regime; (2) dense flow, where the friction coefficient is proportional to the shear rate with frictional particles or the square root of shear rate with frictionless particles, at intermediate shear rates [43], and (3) a critical state, where the friction coefficient has a constant value at the zero shear-rate limit. In Sec. 2.2.5, I

introduce the frictional coefficient into the model.

Introducing simplified cohesion forces, DEM simulations of rheology have been carried out. Refs. [45, 46] performed 2D shear simulations using a simplified inter-particle potential with a short-range cohesive force [47, 48]. They investigated the rheology in the vicinity of the jamming transition point. As a result, they found that a fragile solid develops at a small cohesion regime and shear localisation, in contrast to the rheology of repulsive systems.

Research on the rheology of cohesive granular particles has also been carried out for weakly wetted powders and fine powders, respectively. It is common in both origins of cohesion that cohesive forces can change the rheology and that yielding stresses at zero shear-rate limits remain, even below the jamming transition point [45, 46, 49, 50]. The phase in the steady state can be determined not only by shear strain but also by the strength of cohesive forces [15,30,45,46,51–53]. However, there is no unified understandings of the process of how the shear localisation appears and the effects of the cohesion on the friction coefficient. Therefore, in Chapter 4, I implemented the model cohesive granular system by introducing weak cohesion [45–48]. By applying shear deformation at a constant pressure condition, I will observe the emergence of shear-banding and other phases related to cohesive forces. I will also investigate the effect of cohesion on the friction coefficient in both 2D (Sec. 4.1) and 3D (Sec. 4.2).

## 1.4 Recent developments on machine learning

Finally, here, I briefly review the recent studies on machine learning applied for granular physics which will be relevant to Sec. 3.3. Machine learning is a data analysis method. A machine learning algorithm is fed by training data to discover or predict rules or patterns behind the data, and then the algorithm is deployed to make predictions on subsequent data or inputs. For past several years, the method has been used in granular physics [54–59].

First of all, a machine learning algorithm can be adopted to improve DEM simulations. For example, Ref. [54] uses graph neural networks to estimate the maximum contact forces of granular particles under uniaxial compression, using DEM simulations. Ref. [55] applied the same algorithm to predict trajectories of simulated granular flow. The method could predict the trajectories over short times, but could not predict accurately for long times. Ref. [56] developed an accelerated DEM simulation by replacing the direct calculation of inter-particle interactions by the convolutional neural network. They achieved a speedup of 78 times compared to the traditional DEM software, while maintaining high accuracy.

The machine learning algorithm has also be applied to extract essential features in DEM simulations. Ref. [57] relates microslips and slip avalanches in sheared granular gouges reproduced

by DEM simulations. They extracted feature importance through the machine learning and concluded that the spatial distribution of microslips is one of the essential features to reveal the stress state of granular gouge.

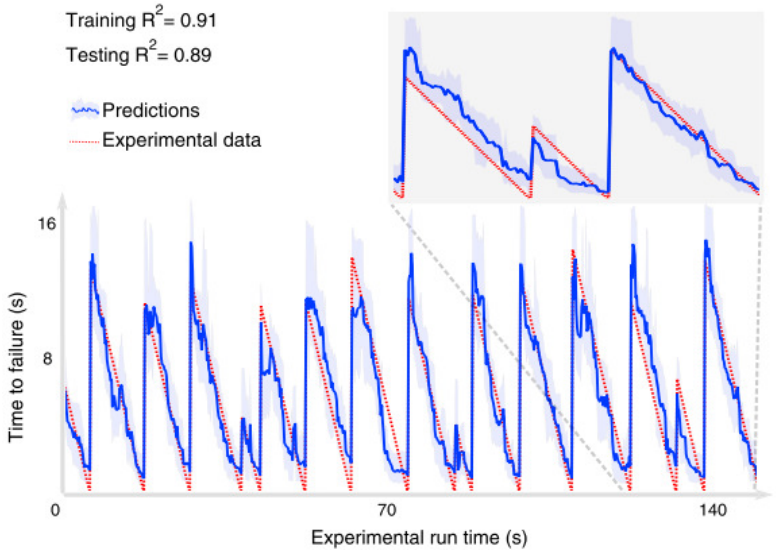


Figure 1.6: Predicted time to failure by the random forest algorithm in laboratory rock shear experiments. This figure is reproduced from [58].

Finally, recent studies have been able to predict the timing of the failure or slippage of system by using machine learning. Ref. [58] applied the random forest algorithm to predict the failure timing of stick-slip behaviour observed in experiments. The stick-slip behaviour is relatively periodic and simple enough to be predicted correctly. The predicted results are shown in Fig. 1.6. Furthermore, Ref. [59] uses XGBoost algorithm to predict the frictional stick-slip dynamics in a sheared granular fault with DEM simulations. They show that the velocities of microscopic particles have predictive information for macroscopic friction. However, these applications of the machine learning algorithms are only applied to predict simple behaviour such as periodic stick-slips. Here, in Sec. 3.3, I will explore the use of machine learning algorithms to predict compressional failure of cohesive granular media.

## 1.5 Research aims and Objectives

The research aim of this thesis is to reveal how emergent phenomena, such as shear failure, compaction failure, or cluster formation, can be captured in a minimal model of cohesive granular media. I will explore the unique effects of cohesion when cohesive granular aggregates experience an external force. In particular, this thesis deals with two types of cohesive forces. The first

system, which has solidified bonds that will break irreversibly, simulates porous rocks. As an example of such a material, a cohesive granular system developed by co-workers will be utilised to reveal the mechanical properties and fracture process when subjected to uniaxial compression [38, 39]. In the second case, cohesive forces can also be observed between fine granular powders, for example, in powdery rock layers formed by abrasion on tectonic faults. I will investigate the effect of cohesive forces on the rheology of granular particles when subjected to shear deformation and where the bonds can reform on a rapid timescale.

Here, I will present the more detailed research objectives of this research work:

- Model cohesive granular system by using parameters gained from similar experiments, aiming for a simple minimal model, yet one with broad predictive power.
- Develop and perform discrete element method simulations of the cohesive granular system when subjected to uniaxial compression.
- Compare simulation results on mechanical properties with experimentally validated results.
- Explore mechanical properties and failure processes of cohesive granular systems beyond the similar experiments by performing parameter studies on system density.
- Predict the failure timing of the cohesive granular system by using the random forest algorithm.
- Develop and perform molecular dynamics simulations in 2D including a weakly attractive potential, to mimic fine powders at the micron-scale.
- Investigate the effect of cohesive forces on the rheology of the cohesive granular system.
- Refine the molecular dynamics simulation of cohesive granular to investigate the details of cluster formation, which is observed as a unique effect of cohesive force.

# Chapter 2

# The simulation model and method

In this chapter, I will describe the governing equations of the discrete element method simulations (hereinafter referred to as DEM simulations). I will introduce the contact forces and the frictional force and briefly summarise the representative contact forces between granular particles in terms of particle size. I will derive the relation between the restitution coefficient and the energy dissipation, which is a characteristic feature of granular particles. I will also explain the general model of the capillary bond, which connects neighbouring particles through the cohesive force and derive the peeling condition of the bond or how bonds fail. The equations introduced in this chapter are the basis for the individual theory in Chapters 3 and 4.

## 2.1 Introduction to the model

The realistic modelling of real sands in contact is complicated [60–65]. For the simplest case, particles can be regarded as ideal spheres. The overlap of particle pairs can be calculated from the particle radii and particle positions. For a more realistic case, a polygonal shape of particles was developed in a recent study [66]. However, the method has only been applied to 2-dimensional systems. Nevertheless, I adopt the spherical shape for granular particles in this thesis since I want to focus on general features of granular physics.

In nature, particle sizes have a wide distribution. For example, the fracture zone where slip happens during earthquakes along faults shows a power law distribution [67–69]. This means that smaller particles are abundant. To duplicate this effect in DEM simulations, an enormous number of particles should be prepared [70–72]. Performing simulations with such a huge number of particles is not reasonable on a realistic time scale, especially when more complex inter-particle interactions are considered. Thus, either a mono-disperse distribution, a bi-disperse distribution, or a poly-disperse distribution with a small variance can be used in practice (eg [73, 74]). In this thesis, I use bi-dispersed particles or poly-dispersed particles with a small variation ($\sim 1\%$) to

perform simulations efficiently and to avoid the crystallisation of particles which can be observed in mono-disperse particle systems [75, 76].

## 2.2 Discrete element method simulation

### 2.2.1 Discrete particles

DEM is a particle-based simulation method [60, 62, 64]. Particles have physical quantities, such as radii, masses, centres of gravity, velocities, accelerations, and angular velocities. Through the updates of these quantities, the time evolution of a particle ensemble can be described in each time step.

### 2.2.2 Equation of motions

I consider the dynamics of a collection of spherical particles that can interact with each other through contact forces. The equations of motion are adapted from studies of granular media, in particular Ref. [7]. The particles are indexed such that particle $i$ has diameter $D_i$, mass $m_i$, centre position $\boldsymbol{r}_i$, angular velocity $\boldsymbol{\omega}_i$ and moment of inertia $I_i = m_i D_i^2/10$. The equations of motion of any individual particle involve the translational and rotational degrees of freedom, and are described as

$$m_i \frac{d^2 \boldsymbol{r}_i}{dt^2} = \sum_{j \neq i} (F_{ij}^n \boldsymbol{n}_{ij} + \boldsymbol{F}_{ij}^t), \tag{2.1}$$

$$I_i \frac{d\boldsymbol{\omega}_i}{dt} = \frac{D_i}{2} \sum_{j \neq i} \boldsymbol{n}_{ij} \times \boldsymbol{F}_{ij}^t. \tag{2.2}$$

The right hand sides of these equations give the inter-particle forces and torques felt between particle $i$ and all other particles. For an interaction between particles $i$ and $j$ the force components $F_{ij}^n$ and $\boldsymbol{F}_{ij}^t$ are defined, respectively, as the projections of the total inter-particle force onto the line connecting the centres of the two particles (*i.e.* with normal unit vector $\boldsymbol{n}_{ij} = (\boldsymbol{r}_i - \boldsymbol{r}_j)/|\boldsymbol{r}_i - \boldsymbol{r}_j|$), and the plane normal to that line.

The normal component of the interaction has a couple of possible contributions: a contact force $F_{ij}^c$ and a dissipation force $F_{ij}^{\mathrm{diss}}$, which is summarised as

$$F_{ij}^n = F_{ij}^c + F_{ij}^{\mathrm{diss}}. \tag{2.3}$$

Tangential forces will be discussed in Sec. 2.2.5.

### 2.2.3 Contact forces

Both components $F_{ij}^c$ in Eq. (2.3) and $\boldsymbol{F}_{ij}^t$ in Eq. (2.1) derive from the contact of adjacent beads pressing on each other. A choice of the contact force depends on the particle scale under consideration. For example, inter-particle interactions on atomic scale particles are well-approximated by the interaction force obtained by differentiating the Lennard-Jones potential [77–79] or the Morse potential [80]. For the micron scale, the Derjaguin, Muller, and Toporov (DMT) theory [81, 82] or the Johnson, Kendall, and Roberts (JKR) theory [83] are used empirically to simulate a cohesive force. On the other hand, interactions between macroscopic particles are often described through a linear spring or the Hertzian contact theory [84] as a function of the overlap distance between particles. Some of these models are shown in Fig. 2.1.

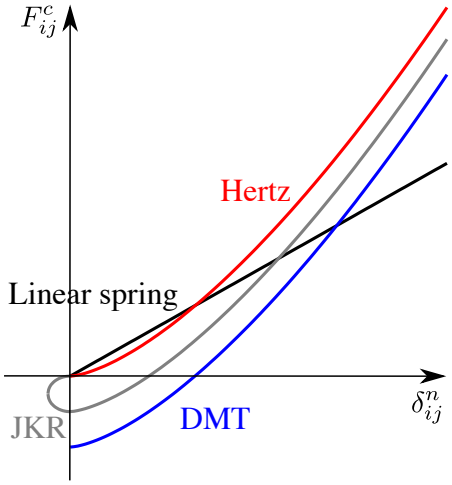


Figure 2.1: Plot of the inter-particle force $F_{ij}^c$, versus particle overlap $\delta_{ij}^n$ for the various models.

The contact forces in the normal direction $F_{ij}^c$ to the particle overlap $\delta_{ij}^n$ are depicted in Fig. 2.1. Here, the positive $F_{ij}^c$ corresponds to a repulsive interaction and the negative $F_{ij}^c$ to an attractive interaction. The positive $\delta_{ij}^n$ means that there is an overlap between the particles. In most models, the contact force begins to have a finite value after particle-particle contact begins. The JKR theory incorporates an attractive interaction that exists over a small distance from the particle contact only when the particles are separated as a result of van der Waals forces [6, 8]. While the linear spring has a linear contact force $F_{ij}^c \propto \delta_{ij}^n$, the force described by the Hertz contact, the DMT theory, and the JKR theory acts with $F_{ij}^c \propto (\delta_{ij}^n)^{2/3}$ [8]. Thus, when the overlap between the particles is larger, the non-linear repulsive force gets stronger than the one from the linear spring.

In Chapter 3, I will consider macroscopic glass beads to be the constituent granular materials. There, I also introduce polymer bonds whose stiffness is softer than that of the glass beads. To

avoid numerical instability and to focus on the strong interactions provided by the beads, I will choose the contact force as a linear spring with a large spring constant to mimic hard-sphere interaction. To achieve the hard-sphere contacts, I will use a ten-time stiffer spring constant of glass beads than one of the polymer bonds.

In Chapter 4, I want instead to deal with sub-micron granulates with cohesion. At this scale, it is often reasonable to describe the particle interactions with the DMT or the JKR model as mentioned above. However, I first model the inter-particle interaction with a linear spring including a short-range attractive force to perturbatively take into account the weak attractive interaction. After a qualitative discussion with this model, I will address the need to perform DEM simulations with the DMT interaction, in order to extend the model to a more realistic one.

### 2.2.4 Energy dissipation and restitution coefficient

Next, I explain the dissipation force $F_{ij}^{\mathrm{diss}}$ in Eq. (2.3). When particles collide, they can experience not only elastic deformation but also inelastic deformation. To include the inelasticity in normal contacts, an energy dissipation with viscous damping is considered between colliding particles, which is modelled as

$$F_{ij}^{\mathrm{diss}} = \begin{cases} -\zeta v_{ij}^n & \delta_{ij}^n \leq 0, \\ 0 & \delta_{ij}^n > 0, \end{cases} \tag{2.4}$$

where $\zeta$ is a dissipation rate. The dissipation depends on the relative velocity at the contact point, which is computed as

$$\boldsymbol{v}_{ij} = \frac{d\boldsymbol{r}_i}{dt} - \frac{d\boldsymbol{r}_j}{dt} - \boldsymbol{n}_{ij} \times \frac{1}{2}(D_i\boldsymbol{\omega}_i + D_j\boldsymbol{\omega}_j). \tag{2.5}$$

Note that here, for simplicity, I ignore the effects of any small overlap when computing velocities (*i.e.* in Eq. (2.5), I consider $D_i$ rather than $D_i + \delta_{ij}^n$). As with forces, I project $\boldsymbol{v}_{ij}$ onto the normal direction connecting the centres of the interacting particles, $v_{ij}^n = \boldsymbol{v}_{ij} \cdot \boldsymbol{n}_{ij}$, and onto the plane orthogonal to this line, $\boldsymbol{v}_{ij}^t = \boldsymbol{v}_{ij} - v_{ij}^n \boldsymbol{n}_{ij}$.

The viscous damping written in Eq. (2.4) is not simulating an actual plastic deformation, which should have a rate dependency [85]. However, this energy dissipation is practically used in DEM simulations since it is easily implemented [86], and the rate dependency is negligible under the manifestation of the transition from an elastic collision to a pure plastic regime [87]. The energy dissipation rate relates to the restitution coefficient $e_n$ by [88]

$$\zeta = -\frac{\sqrt{2mk_n}\ln(e_n)}{\sqrt{\ln^2(e_n) + \pi^2}}. \tag{2.6}$$

Here, $m$ is the reduced mass described as $m = 1/(1/m_i + 1/m_j)$ with mass $m_i$ and $m_j$, and $k_n$ is the spring constant in the normal direction due to the linear spring contact force. I can find the energy dissipation rate by substituting the material properties $k_n$ and $e_n$ into this equation. For example, I used the typical value of $e_n$ as 0.8 for particles, which represents relatively elastic materials such as glass or quartz.

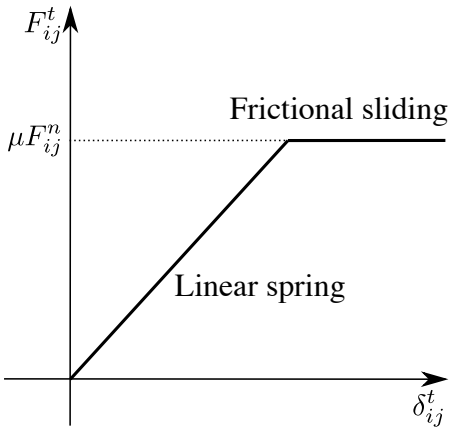


Figure 2.2: Plot of the tangential force for the linear spring model.

### 2.2.5 Frictional force

One of the main features of the DEM is that it includes rotational motion and frictional sliding into the particle interactions, which makes the model differ from more typical molecular dynamics simulations [89]. Here, I explain the frictional sliding and the tangential component of the inter-particle forces, as shown in Fig. 2.2. In particular, I consider the linear spring model for normal and tangential contact models [60].

After two particles have a contact, there is an elastic restoring force acting to return them to their original configuration and a damping force,

$$\boldsymbol{F}_{ij}^t = -(k_t \boldsymbol{\delta}_{ij}^t + \zeta \boldsymbol{v}_{ij}^t), \tag{2.7}$$

where $k^t$ is the tangential spring constant and $\zeta$ is the same dissipation factor considered for normal forces (see Eq. (2.4)). $\boldsymbol{\delta}_{ij}^t$ is the relative tangential displacement away from the initial contact point, and is measured by integrating $\boldsymbol{v}_{ij}^t$ over time. This force is limited by Coulomb friction to have a maximum magnitude of $\mu|F_{ij}^n|$ with a friction coefficient $\mu$, which means that the contact point slips with a frictional sliding after the force reaches the maximum value. The tangential displacement is tracked until particles lose contact.

### 2.2.6 Boundary conditions

Depending on the physical phenomena of interest and the system size, it is necessary to impose boundary conditions appropriately. For example, the periodic boundary condition does not require a physical wall and is suitable to examine the bulk properties. However, when the system size is not sufficiently large, a particle may interact directly or indirectly with its own image on the other side of the boundary, causing physically unnatural results. In the case of preparing a physical wall, there are the options of a clamped boundary, where buffer regions consisting of particles are prepared and the regions are regarded as a wall, and a rigid wall boundary, where walls are prepared without particles and it is required that the interaction between the bulk and the walls is defined properly. Some of these boundary conditions are shown in Fig. 2.3.

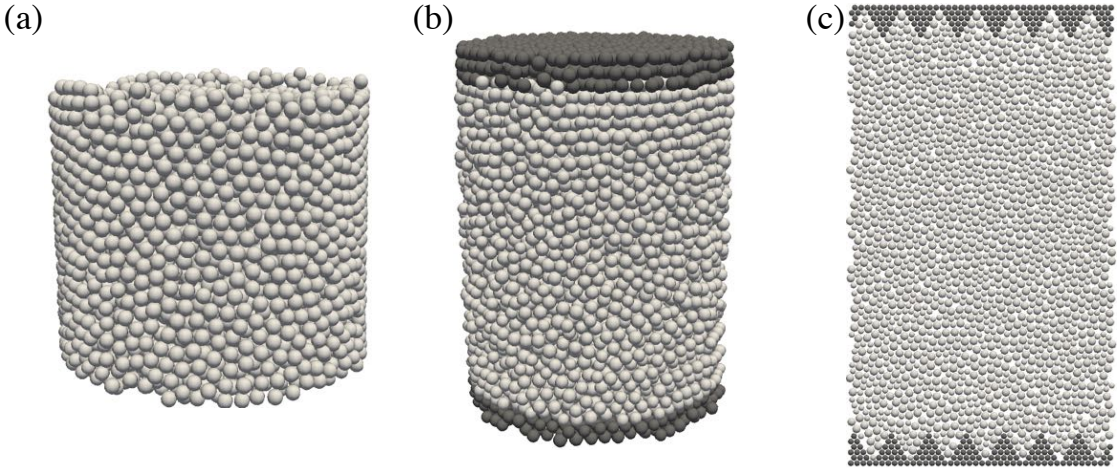


Figure 2.3: Initial configurations and boundary conditions for modelling: (a) a cylindrical system with the rigid wall boundary condition, to be discussed in Sec. 3.1.2; (b) a cylindrical system with the clamped boundary condition, seen in Sec. 3.2.2; and (c) a 2D system with zigzag walls as will be used in Sec. 4.1.2. For each figure, bulk particles are coloured by light grey and boundaries are coloured by dark grey.

In Chapter 3, I adopt either the rigid wall boundary shown in Fig. 2.3(a) or clamped boundary conditions shown in Fig. 2.3(b) for the following reasons. At first, to reproduce an experimental [38] setup which uses the flat and rigid boundaries to apply a uniaxial compression into the bulk, I prepare the boundary condition with the rigid wall boundary. Furthermore, when I investigate the failure of more general materials under uniaxial compression, I use the clamped boundary condition to remove the effects of the boundary condition as much as possible.

In Chapter 4, in contrast, I want to observe the motion of particles under shear at a constant pressure to reproduce corresponding experimental conditions [90] or the condition in a natural

fault [67–69]. Some methods [91] have been proposed to apply a simple shear flow into the bulk with the periodic boundary conditions. The methods impose shear flow to particles when the particles cross borders. However, I consider that it is unrealistic for particles to move back and forth across the wall under constant pressure conditions. Thus, I provide zigzag-shaped walls, which has a larger roughness than the particle scale, composed of particles to provide shear deformation to the bulk. The geometry of the system with boundaries are depicted in Fig. 2.3(c).

These boundary conditions will be described in more detail in the subsequent chapters.

### 2.2.7 Initial conditions: particle packing

The setup of an initial particle configuration is also an important factor in the implementation of the DEM simulations. For example, the too dense packing of mono-disperse particles can allow the particles to form a crystalline structure which can change its mechanical properties [92, 93]. Or, if the packing density is heterogeneous, deformation can be localised in low density regions when the system is subjected to external forces [30, 94, 95]. It is therefore desirable to have a homogeneous distribution of particles when creating an initial configuration for the DEM simulation. This uniform particle arrangement can be achieved by using random hard sphere packing [96, 97].

To prepare for the initial configuration of particles at a high density, the computational cost of either dynamically or statically distributing the particles is quite different. Dynamic particle arrangement requires an additional simulation to be run to make the initial conditions, and a long simulation time is needed to drain the energy from the system and achieve a stable and static initial condition [98]. On the other hand, to find the particle configuration with a local minimum energy, there are static numerical methods that can be used to find a near-optimal solution without running DEM simulations, for example, the steepest descent method [99, 100] or the conjugate gradient method [100]. These methods have been used here to create initial configurations for DEM simulations of packings of hard spheres at various packing fractions $\phi < 0.645$ in 3D. As the method I used to create the initial conditions varies widely on a case-by-case basis, I will explain the detail in the following chapters, specifically in Secs. 3.1.2, 3.2.2, 4.1.2, and 4.2.2.

### 2.2.8 Nature of the bond

In this thesis, I deal with granular particles with cohesive interactions. The cohesive interactions effectively construct a bond between the granular particles, which is either reconstructable or

not. An example of a bond that can be rebuilt is a liquid capillary bridge between weakly wetted particles [10]. As the particles approach each other, the liquid coatings touch up between them, and an attractive interaction acts in a direction that prevents the particles from moving away. When the particles are separated, the liquid bond can be broken, but the bond can be built up again if the particles approach again. Reconstructable bonds are not only observed due to liquid bonds but also come from surface forces, for example due to van der Waals forces acting between tiny particles [6, 8]. To implement these rebuildable bonds in simulations in Secs. 4.1.2, and 4.2.2, I incorporate the effect of the attractive interaction over short distances when there is no overlap between particles [45, 46, 81–83].

For a bond that cannot be reconstructed, I am modelling a cemented granular system. The experiments that are simulated [38,39] have dealt with the construction of liquid bridges between particles with polymers, which are subsequently cross-linked into solid polymer bridges through temperature changes. In this thesis, I have therefore implemented this effect in simulations, paying attention to the following points. Firstly, I distinguish between the properties of the polymer bond and the particles: the polymer is much softer. In the experiments [38, 39], the bond is made of polymer and the particles are made of glass beads. It is therefore necessary to set different values of stiffness and spring constant for each. The next point is about the breaking of the bond. For the polymer bond, the energy needed to break the bond with a mode-I crack is 250 J/m$^2$ [101]. On the other hand, the energy required to peel the bond from the glass beads is only 7 J/m$^2$ [102], which is two orders of magnitude less than the former. Therefore, I incorporate into the model the effect that the bond breaks when the strain energy accumulated in the bond due to deformation exceeds the peeling energy of the bond. Details of the bond failure condition are given in Sec. 3.1.2. For simplicity, I do not further consider the geometry of the broken bonds, although it should remain attached around the particles in real experiments [39].

### 2.2.9 Time-stepping scheme

Finally, I will explain the time-stepping scheme used in my simulations. Here, I will focus on a single particle $i$, which has position $\boldsymbol{r}_i$, velocity $\boldsymbol{v}_i \equiv d\boldsymbol{r}_i/dt$, and acceleration $d\boldsymbol{v}_i/dt = \boldsymbol{F}_i/m_i$ with $\boldsymbol{F}_i \equiv \sum_{j\neq i}(F^n_{ij}\boldsymbol{n}_{ij} + \boldsymbol{F}^t_{ij})$.

The time evolution of the equation of motion Eq. (2.3) was calculated to second-order accuracy of the time increment $h$ for the time integration. For the time evolution of the particle velocity,

I used the two-step Adams-Bashforth method [103], which is a multi-step method, defined by

$$\begin{aligned}\boldsymbol{v}_i(t+h) &= \boldsymbol{v}_i(t) + \frac{h}{2}\left\{3\frac{d\boldsymbol{v}_i(t)}{dt} - \frac{d\boldsymbol{v}_i(t-h)}{dt} + \mathcal{O}(h^3)\right\}, \\ &= \boldsymbol{v}_i(t) + \frac{h}{2m_i}\left\{3\boldsymbol{F}_i(t) - \boldsymbol{F}_i(t-h) + \mathcal{O}(h^3)\right\}. \end{aligned} \tag{2.8}$$

Here, the forces $\boldsymbol{F}_i(t)$ at the current time and $\boldsymbol{F}_i(t-h)$ at one previous time step are required to solve the time evolution of velocity $\boldsymbol{v}_i(t)$. For the time evolution of particle position, I used the two-step Adams-Moulton method [104], which is a similar type of multi-step method, where

$$\boldsymbol{r}_i(t+h) = \boldsymbol{r}_i(t) + \frac{h}{2}\left\{\boldsymbol{v}_i(t+h) - \boldsymbol{v}_i(t) + \mathcal{O}(h^3)\right\}. \tag{2.9}$$

Here, $\boldsymbol{v}_i(t+h)$ can be updated with the Adams-Bashforth method given in Eq. (2.8). By combining these two schemes, I just need to store particle position $\boldsymbol{r}_i$, velocity $\boldsymbol{v}_i$, and the forces acting on the particle at the current time step $\boldsymbol{F}_i(t)$ and the one prior time step $\boldsymbol{F}_i(t-h)$ to compute the time evolution, reducing the computational cost.

In particular, I use $h = 0.001$ in this thesis. This satisfies the Courant condition, which is the stability condition used in DEM simulations [60], described by

$$h < 2\sqrt{\frac{m_i}{k_n}}. \tag{2.10}$$

### 2.2.10 High speeding technique: neighbour-list

In the DEM simulations, the main bottleneck of the computational cost is the calculation of inter-particle forces. I used the neighbour-list method [61, 105, 106] to reduce the computational cost in this thesis.

If I calculate inter-particle forces for all possible pairs of particles, regardless of their distance from each other, it costs $\mathcal{O}(N^2)$ with a particle number $N$. However, in the current simulations, I do not need to take into account the long-range interactions since particles have only the contact force when two neighbouring particles have an overlap or a short-range cohesive force. Therefore, the number of particles with which each particle can potentially interact is limited to those that are present in its vicinity at each time. With this in mind, the neighbour-list method consists in making a list of particle pairs that could possibly interact and utilise and update the list over several successive time steps. The effective length of the interaction on which to base this list is chosen as

$$\boldsymbol{r}_{\text{eff}} = r_c + \Delta r, \tag{2.11}$$

where $r_c$ is the cutoff length for inter-particle force, for example, comparable to the summation of the particle radius and the cohesive interaction range. Here, I assume that particle positions

are not dramatically changing within a single time step. Under this assumption, the list of neighbouring particles is robust for typically $10 - 20$ time steps with a relatively small value of $\Delta r$ [61]. When $\Delta r$ gets longer, the frequency to update the neighbour list can be reduced. However, neighbouring lists can contain a large number of particles, which makes simulation inefficient in terms of time processing and storage requirements. On the other hand, with a shorter value of $\Delta r$, I must update the list more frequently. Therefore, careful tuning of $\Delta r$ is significant with the trade-off between the simulation cost and the frequency of updating the list. Practically, when the following condition is fulfilled, the neighbouring list will be updated [61]:

$$\sum_{\text{time}} (\max|\boldsymbol{v}_i|) > \frac{\Delta r}{2h}. \tag{2.12}$$

Typically, $\Delta r \simeq 0.3 - 0.4 D_i$ is empirically used in DEM simulations in general and I use $0.3 D_i$ in my simulations. With this acceleration method, the calculation cost of inter-particle force can be reduced to $\mathcal{O}(N)$ [61, 106].

# Chapter 3

# Uniaxial compression of cohesive granular materials

In the previous chapter, I outlined a general model for studying granular media with attractive interactions. Here, I will focus on cohesive materials with a brittle bond between particles. This work was done in connection with Dr. Arnaud Hemmerle, who performed laboratory experiments to reveal the connection between macroscopic elasticity and microscopic elasticity originally in References [38, 39]. There, they devised a new type of material made of glass beads connected by polymer bridges. Collaboration with them inspired me to simulate the experimental works by using the discrete element method simulations (hereinafter referred to as DEM simulations). I want to address the scaling properties (Sec. 3.1), the failure process (Sec. 3.2), and the failure prediction (Sec. 3.3) of this type of cohesive material through the DEM simulations. To this end, I performed simulations by putting parameters gained from the collaborators' microscopic experiments into the model. In this chapter, all of the experimental works were conducted by mainly Arnaud Hemmerle, Marcin Makowski, and Alexander Schmeink. Arnaud also performed COMSOL simulations, and I implemented and performed DEM simulations. The results described in this chapter formed the basis of references [107, 108].

Based on the above, I will focus on modelling the artificial cohesive materials developed by our collaborators in numerics. Since the cohesive materials have a tunable elasticity and can be applied in many fields, I can address the fracture process of this kind of material in detail through the model, from both micro and macro perspectives. To this end, I will first describe the results of micromechanical experiments conducted by my collaborators. They directly measured the constitutive relationships of cohesive bonds between individual glass beads in cohesive granular materials. Next, I will show how these measurements can be used to predict such materials' elastic properties. I then construct a macroscopic scale discrete element model (DEM) using the model parameters obtained from the microscopic experiments. In both the experiment and the numerical model, I will show that the properties and geometry of the bridges are critical parameters for upscaling the mechanical properties of the system. I will then show that simulation

can reproduce the essential features observed in the experiments, such as the results of uniaxial compression tests.

## 3.1 Measuring and upscaling micromechanical interactions in a model cohesive granular materials

I can find cohesive materials through nature, as shown in Fig. 1.1. Understanding the mechanical response of these materials, e.g. their elastic properties and failure processes, is essential in many fields such as materials science, earth science, and engineering [16, 20, 21, 40, 41, 109–113]. Additionally, I can observe such materials at a wide range of scales. For example, as mentioned in Sec. 2.1, grain sizes in rock layers formed by abrasion during faulting have a power-law distribution ranging from nanometres to centimetres [67–69]. The layers are composed of porous sandstones, mainly quartz. As a very different example, swallow nests are formed through saliva-induced cohesive bonding between mud grains [16]. In both cases, the mechanical behaviour of these materials depends on the local contacts between their components [16, 19–21].

It is difficult to link the mechanical properties of macroscopic cohesive materials to the local structure of their constituents. For example, the failure mode can change from brittle to ductile, depending on the system's density, plasticity, and local strength of contacts [108, 114–116]. Therefore, while various bottom-up approaches using model systems have emerged in the last decade [37–39, 117, 118], much of this type of research has been conducted in numerical simulations [40, 41, 109–111, 119].

Recently, my collaborators have developed a tunable experimental model for cohesive granular materials [38, 39]. The system consists of spherical glass beads connected by elastic bridges of a solidified elastomer, polydimethylsiloxane (PDMS). The Young's modulus of the system can be controlled by changing the composition of the PDMS (see Fig. 3.1). Although the structure of this material is simplified, it can be used to investigate the mechanical properties [38] and fracture properties [39] of cohesive granules and disordered solids. The elastic properties of the whole system can be finely controlled by changing the stiffness and shape of the PDMS bridges or the proportion of PDMS content in the system. Because of the wide range of tunable parameters, the system is suitable for investigating scaling laws in the mechanics of a wide range of cohesive materials and disordered structures in nature, such as avalanches in snow, earthquake occurrence, fracture of rocks and building materials [17, 29, 120–124].

In addition, my collaborators investigated the fracture properties of the system by performing uniaxial compression tests on the cohesive granular material. The results showed that the system

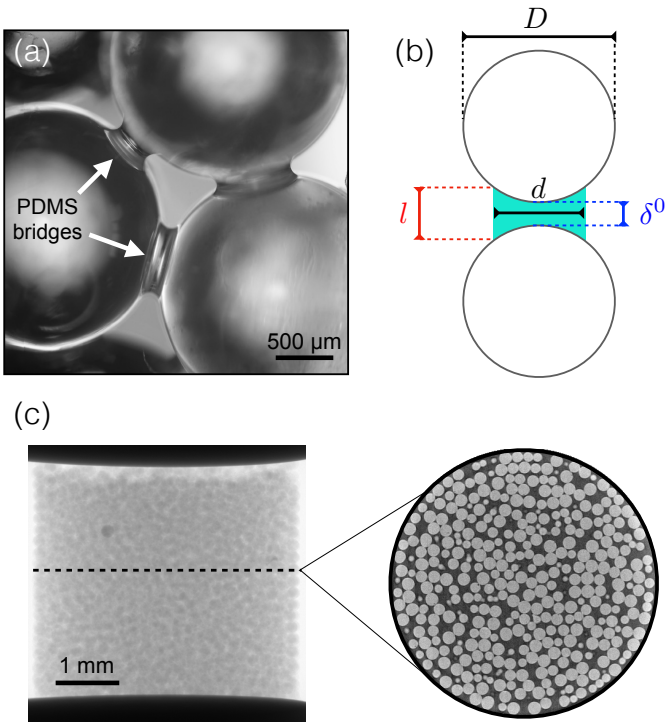


Figure 3.1: Structure of a cohesive granular material. **(a)** A micrograph of a cohesive granular sample shows the capillary bridges of solid PDMS formed between glass beads. **(b)** We model each pair of connected beads as spheres of diameter $D$ linked by a truncated cylinder of diameter $d$ and height $l$ and separated by a gap of size $\delta^0$. **(c)** X-ray tomogram of a sample compressed *in situ* between two pistons. The inset shows a cross-section of the 3D data. The sample is a cylinder of 4.25 mm diameter × 4.05 mm height, made of beads of diameter $D = 200.9$ $\mu$m. In my simulation models, I will match system geometries and particle coordinates to data from tomograms. This figure is reproduced from Ref. [107]

experienced brittle failure with a shear band, but the yielding strain to brittle failure was much higher than that in other systems such as rocks [38]. It has been suggested that these features result from an interaction between microscopic properties at the scale of individual beads and the large-scale (re-)organisation of the packing under mechanical loading. In order to understand in more detail the macroscopic failure process of the material, it is necessary to closely examine the properties of local contacts and properly upscale the microscopic laws for larger assemblies of beads.

### 3.1.1 Micromechanics of cohesive granulates

My collaborators characterised the microscopic mechanical response of a cohesive granular medium [107]. The target for these tests is composed of two glass beads attached together by a PDMS bond. The bond can experience four forces by the relative movement of the glass beads: normal displacement, tangential displacement, rolling, and twisting. [125]. These mechanisms can be modelled by elastic springs. However, we aimed to model this type of material with as few parameters as necessary and to reproduce the essential properties of the material. For this reason, they developed a protocol for measuring the normal and tangential spring constants of a single pair of beads, while they did not take into account contributions from bending and twisting. In this section, I will review my collaborators' experimental methods and results, and outline how these results were incorporated into my model.

#### Experimental methods

My collaborators conducted micromechanical testing on a cohesive granular material by using flexible glass micropipettes, as shown in Fig. 3.2. This type of measurement is often used to measure the forces which cells and other micro-organisms exert [126]. I will get spring constants and bridge heights from these experiments.

Samples of cohesive granular materials were prepared in the same way as in Ref. [38]. Samples are composed of glass beads and polymer bridges. The glass have averaged diameter 365 $\mu$m with a poly-dispersity 5%. The polymer bridges consist of polydimethylsiloxane (PDMS), which is a curable elastomer using a mass ratio of base to cross-linker of $40:1$. Liquid and uncured PDMS and glass beads are poured into a cylindrical mould with a PDMS volume fraction $W = 2.3\%$. Leaving it at 90°C overnight, the PDMS was solidified and forms into a network of pendular bridges between the glass beads. Through the uniaxial compression test of a solidified PDMS cylinder, its Young's modulus was measured as $E_p = 50 \pm 5$ kPa; the ratio of base to cross-linker determines the stiffness of PDMS [38]. PDMS is nearly incompressible, with a Poisson ratio $\nu \geq 0.49$ [127, 128].

To prepare a sample for micromechanical tests, two beads connected by a PDMS bridge were detached from a sample of cohesive granular material by scalpel. This was done under an inverted microscope, taking care not to disturb the bridge. Placing the beads on the glass slide, a droplet of epoxy was applied to half of one of the beads, and it was glued to the flat silicon wafer. After the epoxy had been solidified, the slide glass was removed and one of the beads was attached to the wafer. Then, the other bead was glued to a glass micropipette as shown in Fig. 3.2(a) and (b).

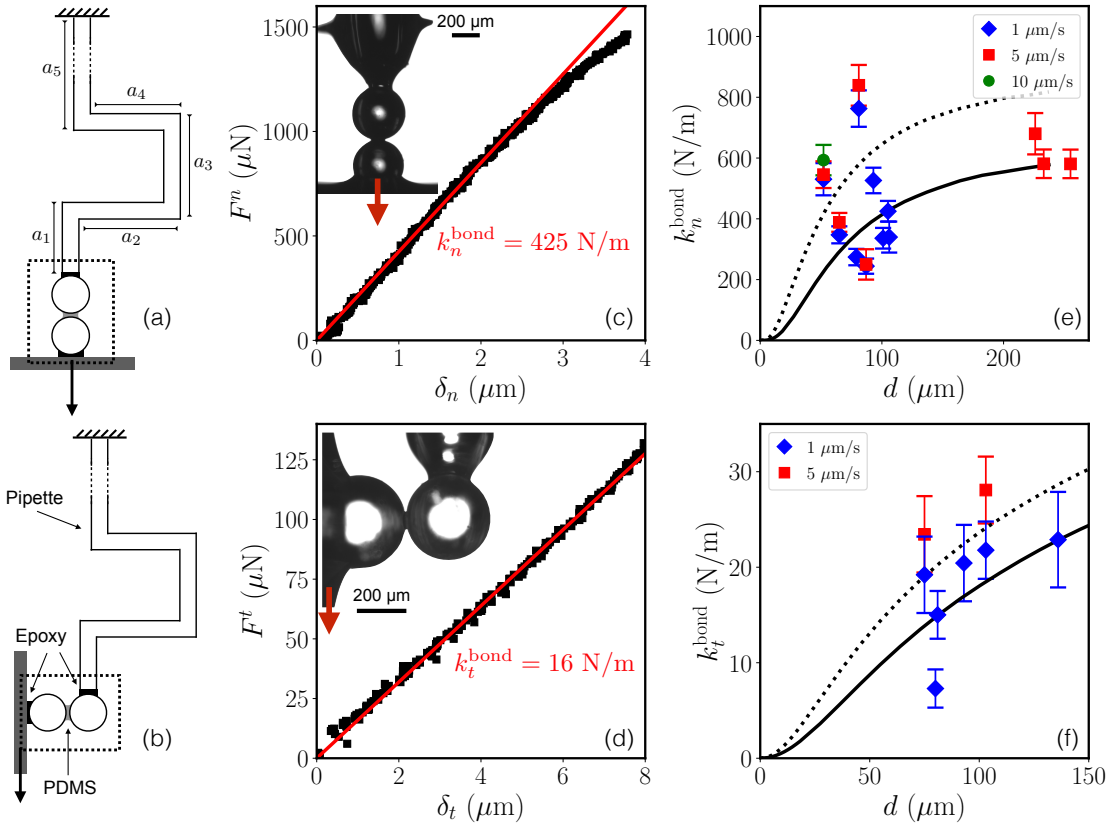


Figure 3.2: Schematics of the micromechanical tests in the normal **(a)** and tangential **(b)** configurations. The dotted frames correspond to the images shown as inserts in the example force-displacement measurements given in **(c)** and **(d)**. Linear fits (red lines) to the force-displacement data give the spring constants $k_n^{\text{bond}}$ or $k_t^{\text{bond}}$. Panels **(e,f)** summarise the spring constant measurements made of different bridge diameters $d$ and at various speeds. The lines are the results of simulations of bridges in similar conditions, assuming an initial bridge length, $\delta^0$, of either 1 $\mu$m (dotted line) or 2 $\mu$m (solid line). This figure is reproduced from [107].

The micropipettes are made of glass filaments bent into a U-shape geometry. For example, in Fig. 3.2(a), $a_1 = 2.5$ mm, $a_2 = 13$ mm, $a_3 = 3.5$ mm, $a_4 = 8.5$ mm, $a_5 = 117$ mm and the pipette has a diameter of 0.3 mm. The U-shape has two advantages. The micropipettes experience only elastic deformations while the bridge is extending, since the glass would break before any plastic deformation. In addition, as for the normal ($F^n$) and shear ($F^t$) forces applied to the micropipettes, they can be independently exerted on the bridge with minimizing any off-axis contributions. The pipettes' spring constant is determined by its geometry and it was measured as $40 \pm 2$ N/m with a pre-calibrated AFM cantilever [126]. To apply an elastic deformation into the bridge, the tip of the micropipette (top of $a_5$) was fixed and the wafer was mounted on and moved by a motorised translation stage.

Digital images in experiments were taken at 10 frames per second and resolution of 1.37 $\mu$m per pixel or 0.55 $\mu$m per pixel. Bead positions were identified using cross-correlation image analysis with a sub-pixel resolution [126]. The beads and micropipette were independently tracked by glass spikes made on the micropipette with the microforge. The force exerted on the micropipette was calculated from its deflection and spring constant [126]. The normal ($\delta^n$) or tangential displacement ($\delta^t$) of the bridge was deduced from the relative displacement of two glass beads. The diameter of the beads and the bridge were obtained by fitting from the microscopic images, to an accuracy of $\pm 2$ $\mu$m. At the beginning of the micromechanical test, the height of the bridge $\delta^0$ was less than 2 $\mu$m, but its exact value could not be measured.

**Results of micromechanical tests**

Micromechanical tests were performed for bridge diameters $d$ from 50 $\mu$m to 270 $\mu$m. Example force-displacement curves for normal displacement and tangential displacement are shown in Figs. 3.2(c) and (d), respectively. Within small displacements up to several microns, the curves seem to be linear and the bridge deforms elastically. By fitting them with linear fits, spring constants $k_n^{\rm bond}$ and $k_t^{\rm bond}$ were estimated. The effect of deformation speeds on the force-displacement curves was also checked. There were minimal differences in the spring constants when the speeds varied between 1 $\mu$m/s and 10 $\mu$m/s. The obtained spring constants for the normal displacements and tangential displacements are shown in Figs. 3.2(e) and (f). The normal spring constant $k_n^{\rm bond}$ has a wide variation between 200 N/m and 800 N/m, while the tangential one $k_t^{\rm bond}$ varies between 5 N/m and 30 N/m. The results suggest that the normal spring constant is much stiffer than the tangential one ($k_n^{\rm bond} \gg k_t^{\rm bond}$) and there are no systematic changes of spring constants to deformation speeds. These conclusions were incorporated into the numerical model, where spring constants were tuned to experimentally relevant values (see Sec. 2.2.3).

**Scaling spring constants: FEM simulations**

For the micromechanical experiments, the bead size $D$, polymer content $W$, and stiffness $E_p$ were fixed. To investigate how these variables affect the spring constant of a bridge, my collaborator also ran finite element simulations by using COMSOL Multiphysics. For this, the geometry of the bridge is sketched in Fig. 3.1(b), where two spherical caps of glass beads are truncated from the ends of the cylindrical bridge of diameter $d$, and the distance between the surfaces of the glass beads is described as $\delta^0$. Taking into account that the bridge is made of incompressible PDMS, Poisson ratio of $\nu = 0.49$ and Young's modulus $E_p$ were used in the calculations.

In the COMSOL simulations, no-slip boundary conditions were imposed on the sphere-bridge

interfaces at the cylindrical edges. One interface is fixed and a normal or tangential displacement is applied to the other interface. By measuring the total reaction force on the fixed interface as a function of the displacement, the spring constants $k_n^{\mathrm{bond}}$ and $k_t^{\mathrm{bond}}$ of the simulated bridge were calculated. The validity of the COMSOL simulations is checked in Figs. 3.2(e) and (f). Here, variable parameters $D$, $d$, and $E_p$ were chosen from the micromechanical test. $\delta^0$ was chosen as 2 $\mu$m since the parameter was at most 2 $\mu$m in the micromechanical test and was revealed to vary between 1 $\mu$m and 2 $\mu$m in macroscopic experiments. The results of COMSOL simulations are shown as the solid lines in Figs. 3.2(e, f) and they coincide with the micromechanical tests (dots), which have relatively weak dependence of $d$. The dotted lines in Figs. 3.2(e, f) correspond to results with $\delta^0 = 1$ $\mu$m. The fluctuations of the magnitude of spring constants in the experiments can be potentially explained from the variation of $\delta^0$ within this narrow range of $1 - 2$ $\mu$m. Furthermore, the dependence of spring constants on $\delta^0$ and $d$ are shown in Figs. 3.3(a, b). These results suggest that the spring constants of cohesive bridges strongly depend on the bridge geometry.

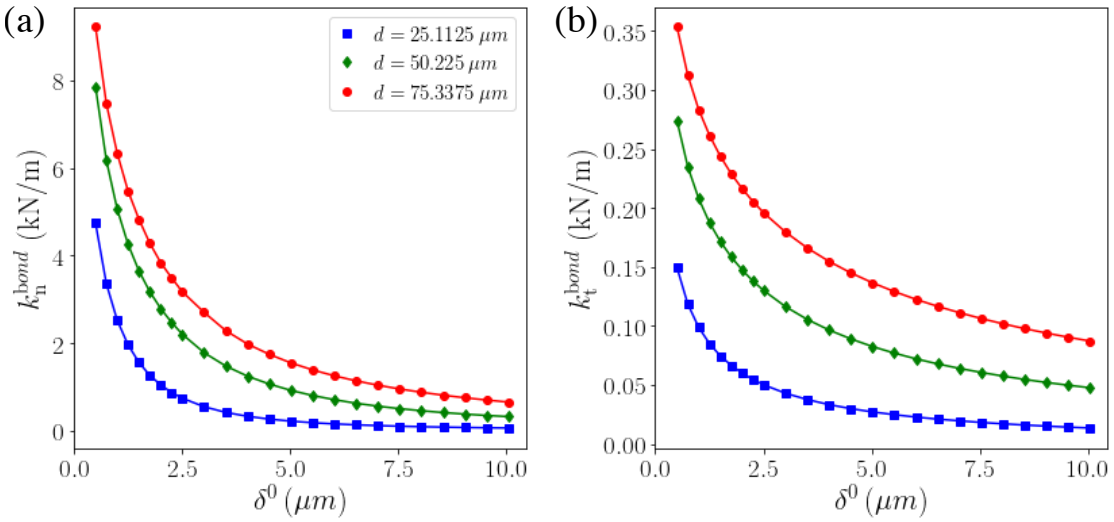


Figure 3.3: The spring constant measurements made of different initial bridge heights $\delta^0$ at various bridge diameters $d$. Panel (a) shows the normal spring constants $k_n^{\mathrm{bond}}$, and panel (b) shows the tangential spring constants $k_t^{\mathrm{bond}}$.

Since the bridge is a linear elastic body, there should also be a linear dependence on $E_p$ for the scaling of the spring constants. Here, I want to focus on reproducing the uniaxial compression test in the macroscopic experiment by using a DEM model of a collection of many beads. Thus, I adopt representative values of $k_n^{\mathrm{bond}}$ and $k_t^{\mathrm{bond}}$, calculated in COMSOL using a experimentally measured microscopic parameters. These values are incorporated into the DEM model to check the consistency of the macroscopic experimental and simulation results.

### 3.1.2 Upscaling micromechanical interactions

Cohesive granular materials can behave elastically to externally applied deformation, both microscopically and macroscopically [20, 37–39, 110, 113, 124, 129]. They can also have well-defined failure conditions at high strain. However, the macroscopic elastic response usually differs from the microscopic one, due to the importance of nonlinear effects such as force chains and strain localisation when approaching failure [108, 110, 129–133]. Thus, it is difficult to upscale the microscopic model to predict the macroscopic model. Likewise, it is also difficult to predict macroscopic failure from microscopic failure conditions. Therefore, the goal here is to use my simulations to upscale from microscopic properties to macroscopic properties of cohesive granular materials and to benchmark these simulations against experiments.

To enable this work, using X-ray microtomography, my collaborators have investigated the deformation process of the cohesive granular materials, both microscopically [107] and macroscopically [38]. The microscopic properties have been obtained through the microscopic experiments of two glass beads and the single bridge that combines them (Sec. 3.1.1). On the macroscopic scale, statistical information on the positions of the beads and the bridge networks that make up the cylindrical system has been obtained when the system is subjected to external deformation. Therefore, I was able to constrain all the parameters of the DEM simulations by their observations and incorporated the conditions for elastic deformation into my simulations. Note that this also includes a condition for fracture of the bridges obtained from microscopic bridge deformation experiments [108]. I then performed a series of DEM simulations of uniaxial compression tests on the modelled material. Here, I will compare the results obtained from the simulations with the macroscopic experimental results and show that this relatively simple model can successfully upscale microscopic details, to make predictions of material properties.

#### X-ray microtomography: Bead and bridge geometry

X-ray microtomography data on two samples has been obtained by my collaborators [38]. One case, called sample A, is shown in Fig. 3.1(c), whereas another case, sample B, was prepared with softer bonds. I will briefly explain the experimental setup. The samples were composed of monodisperse beads of diameter $D = 200.9 \pm 1.9$ $\mu$m, mixed with PDMS of Young's modulus $E_p = 1.5 \pm 0.15$ MPa (sample A) or $E_p = 0.64 \pm 0.05$ MPa (sample B). They have cylindrical geometry with 4.25 mm diameter $\times$ 4.05 mm height for sample A or 4.25 mm diameter $\times$ 4.82 mm height for sample B. Tomography scans were performed before compression, and consisted of sets of $2,000$ projections with a resolution of $1,132 \times 1,132$ pixels and a voxel size of 5 $\mu$m. A quasi-static uniaxial compression was then applied with a constant speed of 5 $\mu$m/s. I will compare

their stress-strain curves with simulations in Sec. 3.1.3.

My collaborators used Matlab to reconstruct the sample volume and identify the locations of beads by identifying the centroids of individual connected volumes after segmentation, to an accuracy of about one voxel size. The locations of bridges could not be identified explicitly, since the X-ray contrast between the bridges and beads was not sufficient to detect them automatically. Instead, bridges were counted manually. By doing this, the averaged coordination number $Z$ was found. For both samples, $Z \simeq 7.4 \pm 0.1$, which is also consistent with their previous study [39]. Furthermore, the bridge diameter averaged from 100 bridges in Sample A were also measured manually and was fit to a Gaussian distribution with a mean of 73.9 $\mu$m and a standard deviation of 12.7 $\mu$m.

These results give a list of the key properties (see Table 3.1) that I will use as input parameters into my simulation model, to check the macroscopic observations.

| Property | Symbol | Micromechanical tests | Sample A | Sample B |
|---|---|---|---|---|
| Bond Young's modulus | $E_p$ | 50 kPa | 1.5 MPa | 0.64 MPa |
| Bond diameter | $d$ | $50 - 270$ $\mu$m | 73.9 $\mu$m | 72.1 $\mu$m |
| Bead diameter | $D$ | 365 $\mu$m | 200.9 $\mu$m | 200.9 $\mu$m |
| Bond stiffness, normal | $k_n^{\text{bond}}$ | $200 - 800$ N/m | 5760 N/m | 2345 N/m |
| Bond stiffness, tangential | $k_t^{\text{bond}}$ | $5 - 30$ N/m | 325 N/m | 131 N/m |

Table 3.1: Key parameters used in the micromechanical modelling. Values are given for the materials used in the micromechanical tests (Sec. 3.1.1), as well as the two samples, A and B, for which the initial bead positions are known from X-ray microtomography (Sec. 3.1.2). In all cases $E_p$, $d$ and $D$ are measured experimentally. The bond stiffnesses are directly measured for the micromechanical test samples, and these results used to validate a FEM simulation of an elastic bridge, which is then used to predict $k_n^{\text{bond}}$ and $k_t^{\text{bond}}$ for the other samples.

**Numerical model of cohesive granulates**

I explain the DEM simulation method in this subsection. As the basic methodology of DEM simulations is summarised in Chapter 2, I focus on the main features of modelling and on the specific modifications made for this study.

In this study, I consider not only contact forces between glass beads but also interactions between glass beads through cohesive bonds (PDMS). These interactions are modelled as linear springs. Each bead is indexed such that bead $i$ has mass $m_i$, centre position $\boldsymbol{r}_i$, diameter $D_i$, angular velocity $\boldsymbol{\omega}_i$ and moment of inertia $I_i = m_i D_i^2/10$, and obeys the equations of motion

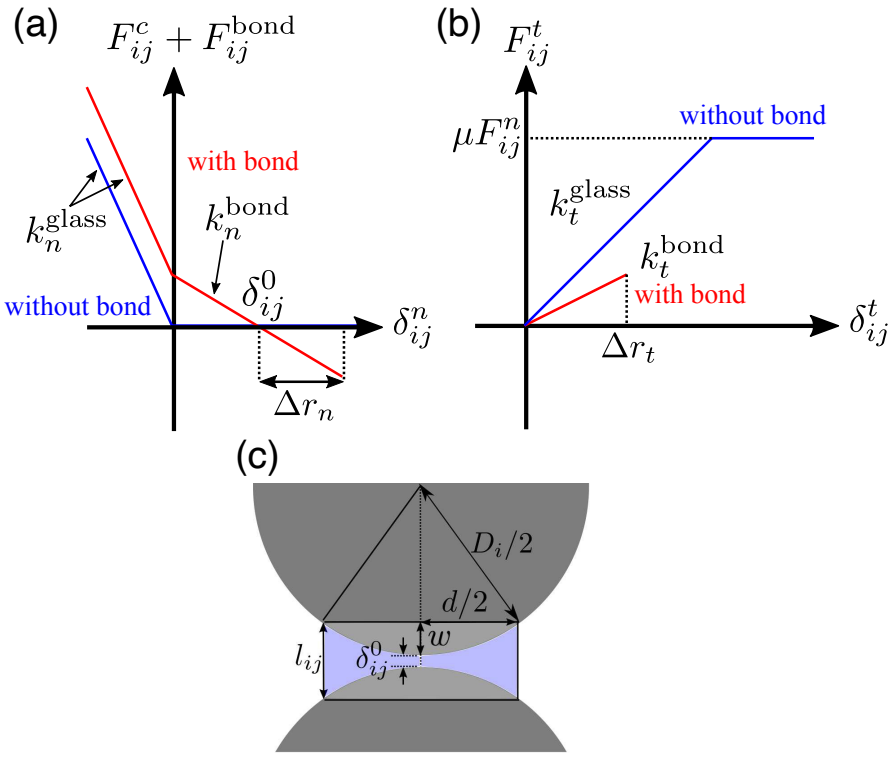


Figure 3.4: Modelling inter-particle interactions. (a) The normal forces between two interacting particles, $i$ and $j$, depends on their surface separation, $\delta_{ij}^n$, and whether or not they share an elastic bond. (b) Similarly, their shear force depends on the tangential displacement, $|\boldsymbol{\delta}_{ij}^t|$, of any contact or bond. In both panels the red curves show the situation of a shared cohesive bond, whereas the blue curves show the case of no cohesive interaction. Here, $\Delta r_n$ and $\Delta r_t$ are the normal and tangential displacements of the bond. (c) A sketch of the geometry of two glass beads held together by a cohesive bond. This figure is reproduced from Ref. [108].

Eq. (2.1) and Eq. (2.2), as described in sec. 2.2.2. The normal component of the interaction written in Eq. (2.3) should include an elastic force due to a bond $F_{ij}^{\mathrm{bond}}$, such that

$$F_{ij}^{n} = F_{ij}^{c} + F_{ij}^{\mathrm{bond}} + F_{ij}^{\mathrm{diss}}. \tag{3.1}$$

Thus, the conservative forces are given by

$$F_{ij}^{c} + F_{ij}^{\mathrm{bond}} = \begin{cases} -k_n^{\mathrm{glass}}\delta_{ij}^{n} + k_n^{\mathrm{bond}}\delta_{ij}^{0} & \delta_{ij}^{n} \leq 0, \\ -k_n^{\mathrm{bond}}\left(\delta_{ij}^{n} - \delta_{ij}^{0}\right) & \delta_{ij}^{n} > 0, \end{cases} \tag{3.2}$$

where $\delta_{ij}^{n} = |\boldsymbol{r}_i - \boldsymbol{r}_j| - (D_i + D_j)/2$ is the surface separation of the particles and $\delta_{ij}^{0}$ is the initial surface separation, which is the equilibrium length of the bridge. Here, I note that two different types of spring constants $k_n^{\mathrm{bond}}$ and $k_n^{\mathrm{glass}}$ are included in Eq. (3.2), which correspond to the spring constant of the cohesive bond and one of the glass bead. I set $k_n^{\mathrm{bond}} = 0.1k_n^{\mathrm{glass}}$ only when nearby particles share a bond, otherwise $k_n^{\mathrm{bond}} = 0$ as shown in Fig. 3.4(a). The ratio between spring constants ($R_{gp} \equiv k_n^{\mathrm{glass}}/k_n^{\mathrm{bond}}$) is low enough to avoid numerical instabilities and high enough to represent the difference between the spring constants. This was confirmed by performing several simulations by changing $R_{gp}$, ranging from 1 to 100, with the obtained stress-strain curves shown in Fig. 3.5. I did not observe any significant changes between $R_{gp} = 5$ and $R_{gp} = 100$. Only when $R_{gp} = 1$, which corresponds to $k_n^{\mathrm{glass}} = k_n^{\mathrm{bond}}$, was the Young's modulus of the system appreciably lower than the others. This could suggest that soft beads facilitate the deformation of the system, giving a larger yield strain and smaller Young's modulus. In any case, using $R_{gp} = 10$ is justified. The dissipation force in Eq. (3.1) is caused by an overlap between glass beads and chosen as Eq. (2.4).

The tangential forces can also act when two glass beads have overlap or they share a cohesive bond. The former case was explained in Sec. 2.2.5. When two glass beads have an overlap and a shear displacement, there exist elastic forces in a shear direction and Coulomb friction with $\mu = 0.5$ [134] expressed as,

$$\boldsymbol{F}_{ij}^{t} = -(k_t^{\mathrm{glass}}\boldsymbol{\delta}_{ij}^{t} + \zeta\boldsymbol{v}_{ij}^{t}). \tag{3.3}$$

However, for the latter case where particles are not overlapping, the spring constant of the bond should be softer than that of the beads, for the same reason as for the normal springs. As such, I also set $k_t^{\mathrm{bond}} = 0.1k_t^{\mathrm{glass}}$,

$$\boldsymbol{F}_{ij}^{t} = k_t^{\mathrm{bond}}\boldsymbol{\delta}_{ij}^{t} - \zeta\boldsymbol{v}_{ij}^{t}. \tag{3.4}$$

Here, there is no frictional sliding due to Coulomb friction when the cohesive bond experiences a large strain; alternatively, the cohesive bond will be broken, as shown in Fig. 3.4(b). I will explain the condition for a breakage of cohesive bond in the following.

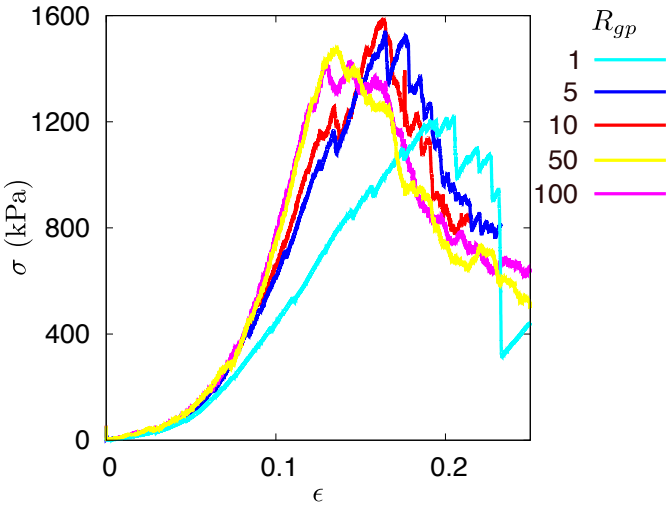


Figure 3.5: Benchmarking of the ratio between two normal spring constants ($R_{gp} \equiv k_n^{\text{glass}}/k_n^{\text{bond}}$). I note that these simulations were done under the condition of producing a cohesive bond when the initial surface separation between neighbouring particles satisfies $\delta_{ij}^n < 0.1D$; in other simulations, I added a cohesive bond $\delta_{ij}^n < 0.064D$, as explained later in this chapter. This difference increases the yield stress of the system but does not affect the qualitative behaviour of the stress-strain curve.

When a large strain is applied to a PDMS bond, the bond can undergo a breakage. To formulate some criterion for the bond breakage, previous studies have made failure conditions based on a von Mises criterion for yielding [41, 135] or the Tresca failure criterion for maximum shear stress [129]. Here, I constructed a failure condition based on energetic considerations. From my collaborators' experimental knowledge, the failure of PDMS bonds can happen by the peelings of bonds from glass beads rather than the internal breakages of the bonds [39]. This can be interpreted that the required energy for the peeling is much smaller than that for the internal breakage. Hence, I allow a bond breakage only when the internal elastic energy exceeds the peeling energy. The energy needed to peel a bond can be written by,

$$U_s = \frac{\pi d^2}{4} G, \tag{3.5}$$

where $\pi d^2/4$ is the surface area of the bond and $G$ is the surface energy of the bond. I used $G = 7$ J/m$^2$, which was measured as the detaching energy of PDMS from glass [102]. Next, I model the strain energy stored in a bond. Since a bond has two degrees of freedom in deformations, which are normal strain $\epsilon_n$ and tangential strain $\epsilon_t$, the strain energy can divided into the normal component $U^n$ and the tangential component $U^t$. Here, I regard the cohesive bond as a pillar of height $l_{ij} = 2w + \delta_{ij}^0$ (see Fig. 3.4(c)) and volume $V = \pi d^2 l_{ij}/4$. Then, the normal component

of strain energy can be modelled as

$$U^n = \frac{1}{2} V {\epsilon_n}^2 E_p = \frac{\pi d^2 l_{ij}}{8} \left( \frac{\Delta r_n}{l_{ij}} \right)^2 E_p, \tag{3.6}$$

where $\Delta r_n = \delta_{ij}^n - \delta_{ij}^0$ is the normal displacement of the bond. Likewise, the tangential component of strain energy can be given by

$$U^t = \frac{\pi d^2 l_{ij}}{8} \left( \frac{|\boldsymbol{\delta}_{ij}^t|}{2 l_{ij}} \right)^2 E_g, \tag{3.7}$$

where $E_g = E_p/(2(1+\nu))$ is the shear modulus of the PDMS bond for this calculation. I used a Poisson ratio $\nu = 1/2$, such that $E_g = E_p/3$. Therefore, by considering the energy balance between the surface energy (Eq. (3.5)) and the strain energy (sum of Eqs. (3.6) and (3.7)), I can gain the failure condition

$$\Delta r_n^2 + \frac{|\boldsymbol{\delta}_{ij}^t|^2}{12} \geq 2 \frac{G l_{ij}}{E_p}. \tag{3.8}$$

For example, when this inequality is satisfied, the cohesive bond will be considered broken and removed in my simulation. This procedure is not reversible and the broken geometry of bonds is not taken into further account, for simplicity.

For the initial condition, I prepared the particle configurations and particle coordinates from experimental setups, which are measured in the microtomograms of samples A and B. Since the radius of each particle could not be gained exactly in the microtomograms, I set up particle radii based on the experimental properties of the bead size distribution, which has a mean diameter of $D = 200.9$ $\mu$m with a standard deviation of 5%, as shown in Table 3.1. To reproduce this distribution, I used the Box-Muller method [136], while avoiding particle overlap at the initial packing. For each sample, I performed DEM simulations on at least 5 independent realisations of the initial conditions and took an ensemble average to get numerical results. The error bars are calculated as the standard deviations of the realisations.

As explained in the previous subsection, in the experiments the beads have approximately 7.4 bonds to neighbours on average. To duplicate this coordination number in simulations, I regarded that a particle shared a bond with any nearby particle if their initial surface separation was less than $0.064D$, as this condition leads to $Z = 7.4$ for the initial packing. To make the simulation model as simple as possible, with few parameters, I set the values of spring constants $k_n^{\mathrm{bond}}$ and $k_t^{\mathrm{bond}}$ as the same values for both samples although they depend on the initial geometries of the bridge. As described above, we estimated the values from $D$, $d$ and $\delta^0 = 2$ $\mu$m by using my collaborator's COMSOL simulations. The representative spring constants chosen in this study are given in Table 3.1.

After making the initial configurations (see Fig. 2.3(a)), uniaxial compression was applied to the system by moving two flat and rigid walls, which are configured at the top and the bottom of

the sample. To reproduce the experimental procedure, I fixed the top wall position and moved the bottom wall upwards at a constant speed of $10^{-4}$ in the non-dimensionalised units of the simulation, which corresponds to 46.4 mm/s. I used this constant velocity for all simulations since the velocity is a compromise between requiring the dynamics to be slow enough to reproduce the quasi-static experiments but still maintaining a realistic computation time. I confirmed that I could reproduce the results with a slower velocity of $10^{-5}$.

For boundary conditions, I used an open boundary at the side wall of the cylindrical sample. When a particle loses all bond connections with neighbours and moves away from the centre of the cylinder beyond a distance twice the radius of the cylinder, it is removed from the simulation, since it can no longer affect the bulk properties.

The normal stress of the system is calculated by

$$\sigma = \frac{F^{\text{wall}}}{\pi R^2}. \tag{3.9}$$

Here, $F^{\text{wall}}$ is the loading force calculated by summing the vertical components of all the forces applied on the top boundary particles from the bulk of the sample. $R$ is a radius of the cylindrical system.

### 3.1.3 Elasticity of cohesive granulates

In this subsection, I will explain results of the cohesive granular material that is modelled based on the measurements from the micromechanical experiments. To test the simulation results, I will compare them with corresponding experiments performed by my collaborators. For example, the stress-strain curves are compared to the elastic response of the cohesive granular materials under uniaxial compression, and comparisons between experiments and simulations are made in terms of the Young's modulus of the system. I then investigate how the Young's modulus is scaled by the stiffness and size of the PDMS bridges.

#### Stress-strain curves

First, to validate my simulation modelling, I compare the stress-strain curves between experiments and simulations of the uniaxial compression of samples with the same geometry. I show the results in Fig. 3.6 for samples A and B. Figs. 3.6(a, b) are the experimental results and Figs. 3.6(c, d) are the simulations' ones. For these, the normal stress $\sigma$ is depicted as the function of the compressive strain $\epsilon$. The material properties used in simulations are selected so that the values are consistent with micromechanical tests and are listed in Table 3.1. The corresponding movies of experiments and simulations are available in supplementary information in Ref. [107].

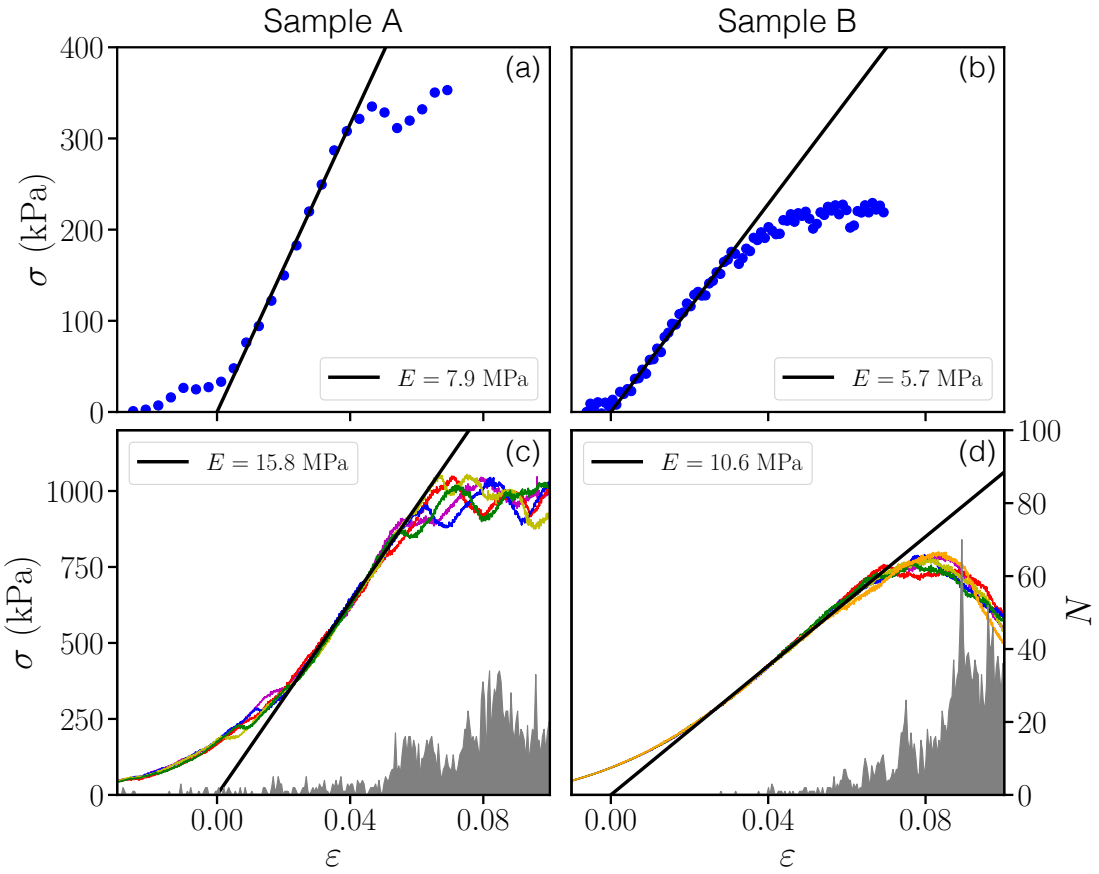


Figure 3.6: Comparison of experimental **(a,b)** and simulated **(c,d)** stress-strain curves. In each case the Young's modulus, $E$, is obtained by a least-squares fit to the linear region (black lines). Each simulated curve corresponds to a different initial realisation of the particle diameters, but using the same particle positions. Panels **(a,b)** share the same $y$-axis, as do **(c,d)**. The grey area in **(c)** and **(d)** gives the number of bonds that break, $N$, in each increment of strain. This figure is reproduced from Ref. [107].

For both samples A and B, results are qualitatively compatible between experiments and simulations; they have concave shapes at small strain, yielding behaviours at large strain, and elastic responses at intermediate strain. These three regimes were explained in my collaborators' experiments [38] and my simulations are consistent with these explanations. At small strain, the contacts between the compressing walls and constitutive glass beads in the sample are progressing. At intermediate strain, the stress is proportional to the compressive strain and the slope, which is measured as Young's modulus, is fitted by using a least-square method. I note that the zero-point of strain ($\epsilon = 0$) is set as an extrapolation of the slope in the linear regime. With progressing compression, the system experiences brittle failure with the yielding. These three regimes are also observed in my simulations. At the same time, simulations could reproduce the

distinct shapes of stress-strain curves due to samples, which come from the system geometry and the stiffness of cohesive bridges. These simulation results have been checked through 5 realisations by changing the initial glass beads' radii. However, simulations show higher stiffness than experiments in terms of Young's modulus. The modelled systems are approximately two times stiffer than the experimental ones for both samples.

I tracked the number of broken bonds $N$, which corresponds to the microcrack activity, as shown in Figs. 3.6(c, d). Detecting this quantity in experiments is not easy, but I can track it in each time step in simulations by monitoring whether each bond has met the failure condition. I counted the number within small strain windows $\Delta\epsilon = 4.2 \times 10^{-4}$. In Figs. 3.6(c, d), the microcrack activity is low throughout the elastic region. However, it bursts towards the yielding of the system and then increases rapidly. This confirms that the response up to the end of the linear region is essentially elastic and that deformation after the elastic regime is an irreversible process accompanied by plastic deformation. The detail of the failure process will be discussed in Sec. 3.2.

**Variation with polymer stiffness**

In my model, there are two types of stiffnesses: the stiffness of glass beads and the stiffness of cohesive bonds. It is widely observed that the cohesive component controls the system stiffness even if that component accounts for only small parts of the entire system [16,37,38,113]. In case the cohesive component is weaker than the majority component, such as the particles or grains, the effect of the cohesive component tends to be dominant. This is also true in our samples, and collaborators have reported that Young's modulus of the whole system $E$ is about one order stiffer than that of the cohesive bond made from PDMS [38,39].

To investigate the scaling of the Young's modulus of the system, $E$, with the Young's modulus of the polymer $E_p$, I ran simulations on the sample A by systematically varying $E_p$. In the simulations, I varied $E_p$, while the other parameters are fixed. I compared the results obtained from simulations with those of similar experiments, in which slightly larger beads with higher poly-dispersity were used: $D = 210\ \mu\text{m} \pm 5\%$. I show the results in Fig. 3.7 with a linear dependency $E = E_p$ (shown as the dashed line). Experiments show that the stiffness is much higher than the linear dependency and simulations also capture this trend. Here, I chose the spring constants of cohesive bonds from the results of COMSOL simulations assuming the initial height of bonds as $\delta^0 = 1\mu\text{m}$ and $\delta^0 = 2\mu\text{m}$. This range of spring constants is based on the observations by the micromechanical tests. I can conclude that the spring constants have a significant role on the system stiffness, $E$, here varying it by 60%. This variation is consistent with the increase in $k_{\text{n}}^{\text{bond}}$, and suggests the sensitivity of the mechanical properties of the cohesive

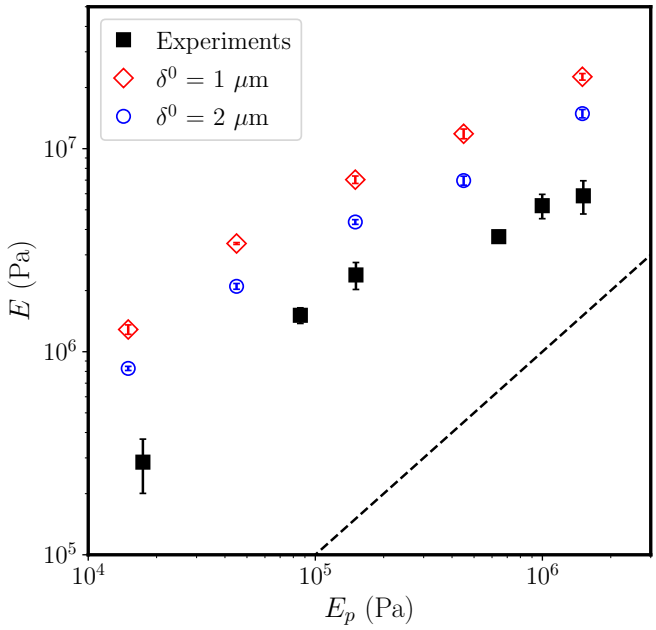


Figure 3.7: Comparison of how the Young's modulus of a cohesive granular sample, $E$, depends on the Young's modulus of the bridges composing it, $E_p$. The simulations (open symbols) reproduce the experimental relationship (closed squares) seen between $E$ and $E_p$, and show the importance of the microscopic bridge length $\delta^0$ in determining the macroscopic stiffness of the sample. The dashed line shows $E = E_p$, for comparison. This figure is reproduced from [107].

materials to the cohesive component.

### Variation with polymer content

Next, as another feature of the cohesive component, I focus on the system stiffness by varying the volume fraction of the cohesive component $W$ in the system. This dependency has been investigated in my collaborators' experiments (see Fig. 3.8). $E$ has approximately linear dependencies with two slopes. The slopes changes at the critical value of $W^* = 2.7\%$. After this point, the stiffness increases slowly with the cohesive content and the point coincides with the point where the pendular-funicular transition occurs [38]. In the pendular regime, the cohesive component or matrix materials span between pairs of neighbouring glass beads and strengthen the materials with increasing matrix content. On the other hand, in the funicular regime, the bridges that form the matrix material are so large that they merge together, filling in the pore space between e.g. clusters of three or more beads [10, 11]. This slower increase with the cohesive component above $W^*$ can relate to the filling in of the larger pore spaces rather than strengthening the bonds.

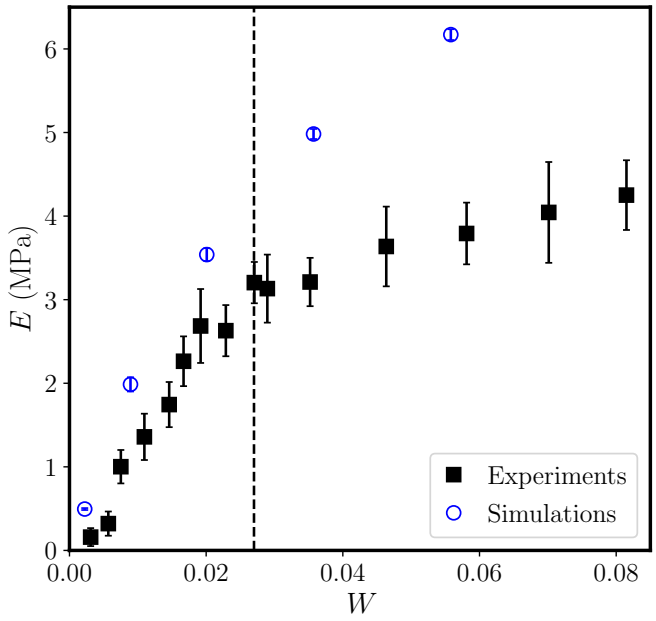


Figure 3.8: The Young's modulus of the material, $E$, increases with increasing content of PDMS, $W$, in a similar manner in both the experiments (closed squares) and the simulations (open circles), up to $W = 2.7\%$ (dashed line). Experimentally, this value corresponds to the appearance of trimer structures in the system, [38] while only pendular bridges are observed for lower $W$. Here, $E_p = 250$ kPa in both experiments and simulations. This figure is reproduced from [107].

Since I assumed the PDMS bridge spans between two glass beads, which corresponds to the pendular regime, I tried to reproduce the linear trend of the stiffness $E$ with $W$ below the $W^*$. To validate the dependency, I varied the bridge diameter $d$ in my simulations of sample A. This change in $d$ causes the changes in the spring constants $k_{\mathrm{n}}^{\mathrm{bond}}$ and $k_{\mathrm{t}}^{\mathrm{bond}}$ and the height of the cohesive bond $l_{ij}^0$ in Eq. (3.8). I estimated the volume fraction $W$ from $d$ based on the empirical relation $W \propto d^2$ [38].

The results are shown in Fig. 3.8 along with experimental results (using $D = 210$ $\mu$m). Although the stiffness from the simulations is again stiffer than the one from the experiments, the two sets of results have good similarities up to the critical point $W^*$. Above the critical point, they are deviating from each other since it is beyond the assumption of the pendular system. In such a regime (funicular regime), another type of modelling is required about the elasticity of the particle bonds.

### 3.1.4 Summary and discussion

In this study, I investigated the relationship between the nature of the microscopic cohesive bridge and the properties of the macroscopic cohesive granular media, which has glass beads connected by the microscopic bridges. To this end, I modelled the cohesive granular aggregates based on micromechanical tests on the cohesive bridge and performed DEM simulations. I restricted the parameters used in the model by the micromechanical tests done by my collaborators. The tests also gave me the insight to build a theory on the failure criteria of the cohesive bridges.

Regardless of the simplification of the modelling, I could capture the macroscopic nature of the system, such as the stiffness of the aggregates and the failure behaviours. I revealed that the geometry and the stiffness of the cohesive bridges play an essential role in the elastic and fracture properties of cohesive granular materials. For example, a slight difference in the bridge length or diameter can significantly affect the macroscopic response, although the cohesive matrix is a small part of the whole system.

In particular, I reproduced the two significant results that are consistent with similar experiments. One is the scaling of the system stiffness $E$ over a couple of orders of magnitudes of the polymer stiffness $E_p$. Within an accuracy of about a factor of two, I reproduced the scaling behaviour. The other is the scaling of $E$ with polymer content $W$ within the pendular regime. The results from simulations diverge from the experimental results at $W = W^*$, which corresponds to the transition point from the pendular regime to the funicular regime. This transition in stiffness is also observed in Ref. [113] using millimetric beads and a harder cement, suggesting the cross-over of stiffness with $W$ is a general result.

However, simulations consistently predict stiffer systems than observations from experiments. This is arguably caused by the single choice of the bridge height $\delta^0$. Although the observed heights in experiments are distributed widely [39], I used the representative value in simulations: $\delta^0 = 1$ $\mu$m or $\delta^0 = 2$ $\mu$m. Fig. 3.7 directly shows that the change in $\delta^0$ affects the system stiffness significantly. If I use the broader values on $\delta^0$, which would contribute to a lower stiffness of polymer bridges, the system would expect to have a weaker stiffness.

Regarding the system failure, the model also correctly predicted the strain where the sample experiences a non-elastic response to compression and starts to fail, as shown in Fig. 3.6. This fact suggests that my criteria for bond breakage (Eq. (3.8)) works correctly in my simulations. The failure criteria imply that the bridge breaking in tension is more likely than breakage with a shear displacement. The criteria also suggest the dependence of the bond breakage on the nature of the bond, for example, Young's modulus $E_p$, the height of a cylinder $l_{ij}$, and the interfacial energy.

Finally, I discuss the failure process of this kind of material. The model built in this study enable us to track the spatio-temporal dynamics of microscopic failures within the sample by detecting failure points of cohesive bonds. These quantities are difficult to measure with high resolution in experiments. However, I can address this efficiently in the numerical simulations. Measuring these quantities could allow me to predict the failure mode and the failure timing before the material experiences an in-elastic deformation. In the following section 3.2, I will address the failure mode of the cohesive granular aggregates by changing the system density. In Sec. 3.3, I will try to predict the failure timing by using machine learning.

## 3.2 Failure processes of cohesive granular materials

In Sec. 3.1, I modelled a cohesive granular system through DEM simulations based on micromechanical experiments. The model was simple but could capture the essential features of the experiments, such as stress-strain curves and how the elastic properties scale in response to changes of polymer stiffness and polymer content. However, beyond qualitatively confirming the shear band mechanism experimentally, I did not address the details of the failure process. Here, I will focus on the failure in detail. In particular, cohesive granular materials are known to show a brittle-ductile transition depending on the system's density, plasticity, and local strength of contacts [108,114–116]. Therefore, I will reproduce the transition from shear bands to plastic deformation and to compaction bands in the same simple model implemented by DEM simulations and show that my numerical model can apply to many materials.

### 3.2.1 Introduction to chapter 3.2

In this chapter, I have modelled materials that consist of individual grains held together by a matrix material. Natural examples are mortars, asphalts, volcanic ash, and snow [124], and artificial examples are cemented solids, sintered glass, and alumina beads [38,39,113]. Since this kind of material can be found in many fields, we can also see the failure of such materials in many contexts, such as geological situations or industrial materials [137].

For a fixed sample size, two essential competing components determine the fracture mode in cohesive granular materials [138]: stress localisation due to damage [22] and damage scattering due to disorder [23]. For example, the porosity of a system can determine how it fails. Rocks with lower porosity can experience brittle failure, whereas rocks with higher porosity can deform plastically, in the same manner as metal [24]. A further increase in porosity can lead to other local fracture modes, such as an anticrack. We can define an anticrack as a failure mode with the displacement field of a Mode-I crack, but with the reversed sign, i.e. compression or closure

rather than opening displacement [17, 25, 26].

Brittle materials, such as rocks, have been studied in a variety of stress conditions in laboratory experiments [120–122, 139–142]. For the uniaxial compression of a dense brittle material, one common response is failure by macroscopic shear-banding. We can also detect microscopic damage during deformation through acoustic signals [120–122, 139–142]. By tracking the spatial locations of the signals, we can observe that randomly distributed damage under a small deformation progressively localises to form system-spanning shear bands leading to catastrophic failure. Recently, the X-ray tomography method [143, 144] has also been used to measure the details of microscopic failure. Similarly, a conductivity-based method was applied to detect microcracks in sandstone under strong temperature variations [145]. The statistics of the microscopic failure for a range of porosities and materials have been studied experimentally [146, 147] and numerically with DEM simulations [41, 135].

As another type of failure, we commonly observe plastic deformation in metallic materials or rocks under particular conditions, such as high confining pressure [28, 148] or high temperature [149]. Relatively higher porosity with lower strain rate can cause the brittle-ductile transition at lower confining pressure [148, 150–152], and let high porous rocks, such as sandstone, deform plastically. The brittle-ductile transition due to strain-rate hardening has also been observed in micrometre scale metals [153, 154].

In a different context, purely compressible deformation bands, called compaction bands or anticracks, have been reported in geological field studies [155, 156]. These bands develop in a transverse direction to the confining axis. Some previous studies include field studies [157–159], theoretical modelling [160, 161], laboratory experiments [120, 121, 142, 160, 162, 163], and simulations [164, 165]. As a result, the compaction bands are known to develop only in particularly low-density systems, including foams [123] and snows [29, 166]. After their formation, such bands can work as a barrier to water flow and restrict the directivity of permeability in sandstone aquifers [163, 167]. The development of compaction bands are regarded as equivalent to anticrack formation and can be described in terms of the Eshelby inclusion model [26].

In Sec. 3.1, I designed the numerical model to capture the initial elastic and eventual yielding processes in cohesive granular media, as observed in similar experiments. In this section, I will now show that the model can systematically extend to cohesive materials with a range of packing fractions and can reproduce a wide range of the observed behaviours of natural materials, including sandstone [120, 121, 142], snow [29], and foam [123]. In the elastic regime, I will show power-law scalings of the Young's modulus and the yielding stress with the effective bond density. Beyond the yielding point, I observe three distinct failure modes for a range of packing fractions. For example, the model could capture a shear band formation at higher densities corresponding

to a brittle failure, uniform deformation without failure bands corresponding to a ductile failure, and a compaction failure at lower densities corresponding to a compaction band. It shows how these very distinct failure modes can occur in similar materials in response to changes in their densities. Furthermore, I will show that the model can also detect the statistical properties in distribution of microcracks. Therefore, the model has the potential to investigate quantitative predictions that are hard to probe otherwise.

### 3.2.2 The model

The internal dynamics and internal rules of the DEM simulations here are identical with those given in Sec. 3.1.2. In this study, I added a couple of modifications into the initial setup of the model, in order to observe the failure process of cohesive granular materials at several packing fractions. First, I used slightly different geometries to perform the DEM simulations. For example, using longer pillars (shown in Fig. 3.9) can reduce the effects of the boundary on internal failure. Secondly, I changed the model setup. Particularly, I introduced random dense packing to make initial configurations, allowing the numerical simulation to extend to cohesive materials with a range of packing fractions. I also modified the boundary conditions to clamped boundaries, as explained in Sec. 2.2.6.

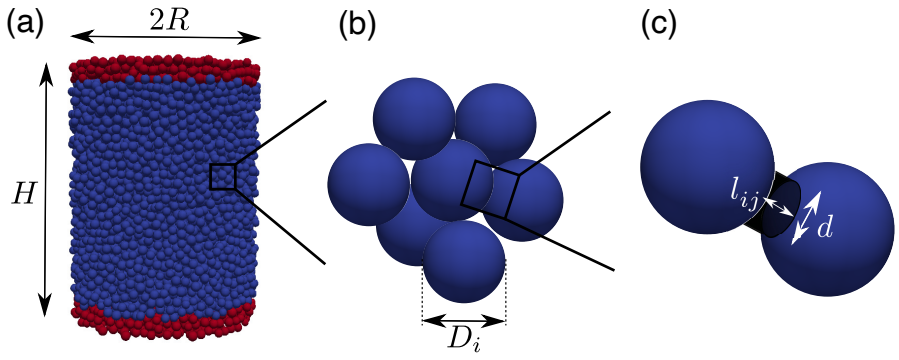


Figure 3.9: Modelling a cohesive granular medium involves considerations of different scales. (a) I simulate the compression of a cylinder with radius $R$ and height $H$. It is composed of spherical particles, grains or beads, held together by elastic bridges. Particles near the upper and lower boundaries (red) are clamped, so that they can only move vertically. (b) The magnified view shows randomly arranged and slightly poly-disperse particles, where particle $i$ has a diameter $D_i$. Each particle can interact with its neighbours by contact forces, and by any bridges or bonds. (c) Zooming in more, I model a bond between particles $i$ and $j$ as a truncated cylinder of height $l_{ij}$ and diameter $d$. This bond can stretch, both normally and tangentially, and will break if strained enough. This figure is reproduced from [108].

### Simulation parameters

Simulation parameters are constrained by a similar experiment (Sample A in Table 3.1). I list parameters used in this study and their non-dimensionalised forms in Table 3.2. I note that all the quantities are non-dimensionalised in terms of the average mass ($m$), the average particle diameter ($D$), and the spring constant for normal glass beads ($k_n^{\text{glass}}$).

### Model setup

Next, I describe how to make the initial configurations and boundary conditions. First, I prepared a cubic region with periodic boundaries in the horizontal directions and rigid walls at the top and bottom. To make a material with a particular packing fraction $\phi$, I tuned the number of particles with particle diameters of a Gaussian distribution with a standard deviation of 1%. I used the Box-Muller method [136] to reproduce the poly-dispersity. Once the number of particles was fixed, the pointlike particles were randomly distributed within the box and slowly increased their diameters. Particle positions are updated to avoid overlaps with nearby particles using the algorithm described in References [96, 97]. When particles' sizes are small, overlaps between particles can be easily eliminated by slight displacements. On the other hand, as the particle size

| Property | Symbol | Value | Scaled value | Ref. |
|---|---|---|---|---|
| Sample diameter | $2R$ | 4.22 mm | $2R/D$ | [38] |
| Sample height | $H$ | 5.91 mm | $H/D$ | – |
| Bond diameter | $d$ | 75.4 $\mu$m | $d/D$ | [39] |
| Bond stiffness, norm. | $k_n^{\mathrm{bond}}$ | 5.76 kN/m | $k_n^{\mathrm{bond}}/k_n^{\mathrm{glass}}$ | [39] |
| Bond stiffness, tang. | $k_t^{\mathrm{bond}}$ | 0.32 kN/m | $k_t^{\mathrm{bond}}/k_n^{\mathrm{glass}}$ | [39] |
| Friction coefficient | $\mu$ | 0.50 | 0.50 | [134] |
| Bead diameter | $D$ | 200.9 $\mu$m | 1 | [38] |
| Bead mass | $m$ | 10.8 $\mu$g | 1 | [38] |
| Bead stiffness, norm. | $k_n^{\mathrm{glass}}$ | 57.6 kN/m | 1 | [107] |
| Bead stiffness, tang. | $k_t^{\mathrm{glass}}$ | 3.25 kN/m | $k_t^{\mathrm{glass}}/k_n^{\mathrm{glass}}$ | [107] |
| Interfacial energy | $G$ | 7 J/m$^2$ | $G/k_n^{\mathrm{glass}}$ | [39, 102] |

Table 3.2: Model properties set to experimentally observed values, corresponding to glass beads held together by softer (PDMS) bridges. In particular, Refs. [38, 39, 107] correspond to observations made in identically prepared materials. The sample height $H$ is 1.5 times that studied in Ref. [38].

increases, especially in a system with a high packing fraction, achieving an entirely overlap-free particle configuration is not easy. I take the vector sum of overlaps with neighbouring particles and move the particles towards that direction. However, if the norm of the vector sum becomes larger after the movement than one before the movement, I do not move the particle. Under these rules, I moved particle positions iteratively. To accelerate this procedure and avoid particles getting stuck with a finite overlap, I added a tiny random displacement to each iteration.

After the system achieved a random dense packing, I shaped the cubic system into a cylinder of radius $R$ and height $H$ by removing all the outliers from this cylindrical region. Then, I added a cohesive bond between any neighbouring particles when $\delta_{ij}^n < 0.1D$. I list the number of particles in the cylindrical system for each packing fraction, along with their coordination numbers in Table 3.3.

For boundary conditions, I adopted clamped boundary conditions, as shown in Fig. 3.9(a). I fixed the relative positions of all particles within $2.5D$ of either top or bottom edges of the cylinder. The bottom particles are allowed only to move vertically, while the top particles were held rigidly fixed in place. By moving the bottom wall upwards at a constant velocity of $10^{-4}$, I compressed the system vertically. Then, I calculated $F^{\mathrm{wall}}$ and $\sigma$ in the same way as in Sec. 3.1.2.

| $\phi$ | $N$ | s.d.($N$) | $Z$ | s.d.($Z$) |
|---|---|---|---|---|
| 0.350 | 6,754 | 38 | 3.887 | 0.061 |
| 0.375 | 7,207 | 44 | 4.040 | 0.061 |
| 0.400 | 7,721 | 59 | 4.242 | 0.060 |
| 0.425 | 8,194 | 36 | 4.535 | 0.143 |
| 0.450 | 8,708 | 39 | 4.841 | 0.088 |
| 0.475 | 9,189 | 46 | 5.218 | 0.078 |
| 0.500 | 9,665 | 19 | 5.721 | 0.127 |
| 0.525 | 10,136 | 15 | 6.261 | 0.028 |
| 0.550 | 10,616 | 18 | 7.018 | 0.038 |
| 0.575 | 11,084 | 25 | 7.837 | 0.020 |
| 0.580 | 11,188 | 10 | 7.979 | 0.015 |

Table 3.3: In initial configurations the average number of particles, $N$, and their coordination number, $Z$, depend on the packing fraction, $\phi$. The tabulated values are averaged over five independent realisations with different initial configurations and standard deviations are indicated by s.d.($N$) or s.d.($Z$).

### 3.2.3 Results and Discussion

In this subsection, I will show results on the failure of the simulated cohesive granular material under compression at a wide range of packing fractions, between $\phi = 0.350$ and 0.580. At the lowest packing fraction of $\phi = 0.350$, simulations could not be continued since many particles floated across the open boundary conditions in a radical direction. I will begin with the elastic regime of the system at low strains and move to the statistical properties of microcrack activity before and after the failure points. Finally, I will explore the details of failure processes at several $\phi$.

I show the overview of this study in Fig. 3.10. At a high packing fraction of $\phi = 0.580$, I observed development of shear bands, as shown in Fig. 3.10(a). At an intermediate value of $\phi = 0.500$, as in Fig. 3.10(b), the sample deforms plastically without prominent failure bands. At a lower density of $\phi = 0.400$, as in Fig. 3.10(c), the system shows localised failure bands along a horizontal plane, resembling an anticrack [123] or compression failure [121, 122].

#### The elastic regime

I show the stress-strain relationships under uniaxial compression of samples at different initial packing fractions in Fig. 3.11. For small strains, the system deforms elastically and shows a

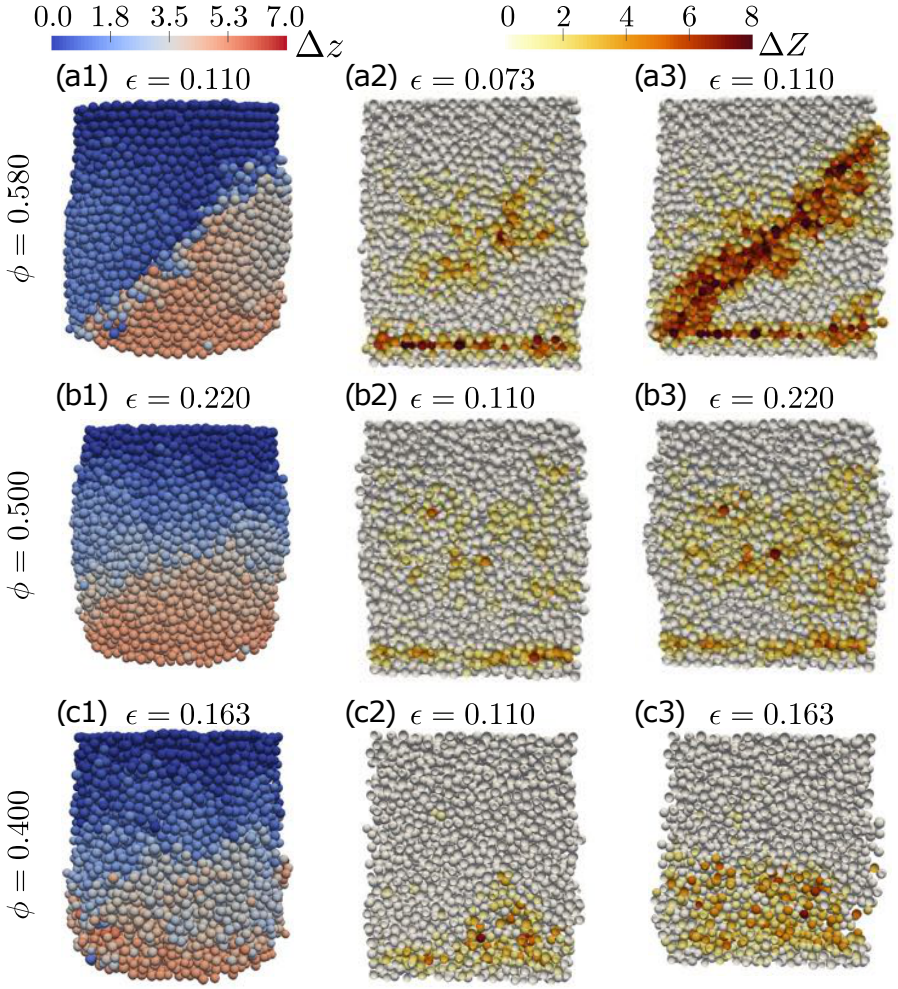


Figure 3.10: Deformation and failure modes of cohesive granular media at various packing fractions, $\phi$. Examples are shown, by row, for representative values of (a) a dense packing of $\phi = 0.580$, (b) an intermediate case of $\phi = 0.500$ and (c) a low value of $\phi = 0.400$. In column (1) the particles at the surface of the deformed samples are coloured to show their vertical displacements, $\Delta z$, compared to their initial positions. The sample in (a1) fails along a slip plane or shear band, whereas (b1) shows the yielding of the system by plastic deformation and uniform compaction is seen in (c1). Columns (2) and (3) show cross-sectional snapshots of these processes at various strains, which highlight the changes in coordination number, $\Delta Z$, as the deformation proceeds. These cross-sectional snapshots are depicted as perpendicular, vertical planes through the centre of the object. In all cases there is activity at the lower boundary, resulting from the clamped conditions. Additionally, (a) shows damage localising along an inclined shear band, whereas (c) highlights a horizontal failure plane. This figure is reproduced from [108].

linear stress-strain curves. I measured the Young's modulus $E$ of each sample by fitting the linear regimes of the curves, as in Fig. 3.6. For the highest packing fraction of $\phi = 0.580$, the shape of the

stress-strain curve has similarities with the one from the corresponding experiment [38], as shown in Fig. 3.11(b). The agreement between simulation and experiment comes from the fact that I used the same particle positions as the measured sample. The model estimated a consistently stiffer sample ($E = 13.7$ MPa) than the experiments ($E = 7.9$ MPa) for similar reasons to those discussed in Sec. 3.1.3. In particular, I simplified the model by making all cohesive bridges have the same spring constant. The clamped boundary conditions also contribute to the stiffer sample compared to the experiment since boundary particles are considered to be artificially stiff particles without any horizontal displacements.

The denser a system is, the higher the coordination number will be, and there will be more cohesive bonds shared with nearby particles (see Table 3.3), which makes the system stiffer than those with a lower $\phi$. I depicted this trend in Fig. 3.11(c), and Young's modulus $E$ increases smoothly with $Z\phi$, which corresponds to a contact density (*i.e.* the density of bonds or bridges within the material). I fitted the dependency by a power law, $E \sim (Z\phi)^{\xi}$, with exponent $\xi = 3.27 \pm 0.14$. As discussed below, this scaling is generally consistent with the behaviour expected in the aggregated system [110].

The stiffness of a granular material strongly depends on internal properties such as the packing fraction and particle structure [110,168–171]. Whereas the effective-medium theory of a frictional granular medium without cohesion would suggest a linear dependency of $E$ [172], Gaume *et al.* [110] has reported that sticky hard spheres have a data collapse for $E(Z\phi)$, with a power law with an exponent of $\xi = 4.9$. Similarly, the cohesive granular system in 2D has been reported to show a more rapid increase in $E$ with $Z\phi$ than the one predicted by effective-medium theory [130, 132]. This strong dependency of the bulk stiffness on contact density has been attributed to the presence of force chains or force networks with some correlation length, which can be decoupled from the particle geometry or system size [110, 130, 132].

From an alternative perspective, such scaling is often instead described only in terms of the volume fraction $\phi$, for example in dilute colloidal gels [170, 171] and more dense powder agglomerates [168, 169]. These cases also suggest power-law scalings of $E \sim \phi^{\gamma}$ with $3 < \gamma < 5$. The prevailing consensus is that these power-law scalings reflect the scaling of an effective backbone of stress-bearing elements [171].

**Onset of failure**

Beyond the elastic regime, the stress-strain curves in Fig. 3.11(a) show either a peak stress representing a compressive strength, or a plateau stress indicating a yield stress. A denser system with high $\phi$ tends to sustain higher stress; a sparse system with low $\phi$ yields without as well-defined a peak stress. This kind of dependency of the strength of a material with its

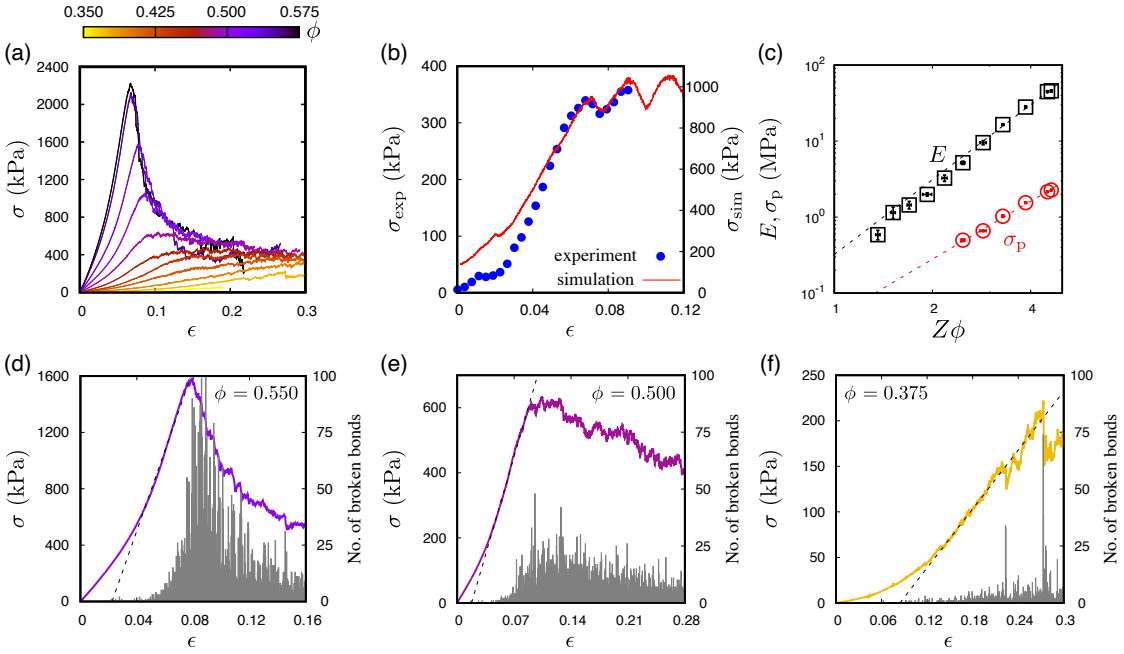


Figure 3.11: Elastic response of cohesive granular media. (a) The stress-strain curves depend on the initial packing fraction, $\phi$. As $\phi$ decreases the material becomes softer, and the peak stress drops. The post-peak behaviour also changes, from a more brittle to a plastic, yielding response. (b) A comparison can be made between an experimental stress-strain curve measured in our motivating material [38] and simulation results where the initial particle positions are taken directly from that experiment. (c) The Young's modulus (black squares) depends on the initial density of contacts or cohesive bonds, *i.e.* with $Z\phi$, in a manner consistent with a power law of exponent $\xi = 3.27 \pm 0.14$. This broadly agrees with the scaling reported for other cases of adhesive (sticky) granular media or aggregates [110, 168–171]. Simultaneously, the peak stress, $\sigma_p$ (red circles), depends on $Z\phi$, consistent with a power-law fit of exponent $\alpha = 2.53 \pm 0.12$. The global microcrack activity (here, bonds broken in each $3 \times 10^{-4}$ strain step) also varies with $\phi$. Representative plots show (d) brittle failure at $\phi = 0.550$, with an accompanying burst of activity and a large post-peak stress drop; (e) ductile failures at $\phi = 0.500$, with a broader and less-defined peak of activity; and (f) the formation of an anti-crack at $\phi = 0.375$, with intermittent stress drops and associated spikes of microcrack activity. The dashed lines in (d)-(f) show fits to the elastic regime, used for estimating $E$. This figure is reproduced from [108].

density has been widely observed in the uniaxial compression experiments of cohesive granular materials, for example, porous alumina [146], sandstones [131], and their corresponding DEM simulations [133,173]. In these cases, porosity controls the strength of cohesive granular materials for the following reasons. At first, since stresses tend to localise at contact points in porous

materials, those contact points act as defects where stresses concentrate beyond the limiting fracture toughness [174]. Additionally, recent work on the transmission of force chains through cemented granular media suggests that more porous samples bear a higher stress localisation, which significantly reduces their ultimate load carrying capacity [133].

In this study, I observed a well-defined peak stress in the stress-strain curves for samples above $\phi = 0.525$, corresponding to their brittle failure mode (see Fig. 3.11(d)). On the other hand, for intermediate packing fractions, the stress did not show a definite peak stress and instead achieved a roughly plateau level for intermediate packing fractions, consistent with a continuous yielding process or plastic/ductile failure (see Fig. 3.11(e)). With a further decrease in packing fraction, the stress-strain curves showed intermittent and irregular drops in stress (see Fig. 3.11(f)). When I could define the peak stress reasonably (specifically, for $\phi \geq 0.475$), I investigated the dependency of the peak values, $\sigma_{\rm p}$, on the contact density. I show these data in Fig. 3.11(c) with a fitting curve of a power law of exponent $\alpha = 2.53 \pm 0.12$. This dependency has a good agreement with the power-law scaling of exponent 3.04 reported by Gaume *et al.* [110] for the ultimate compressive strength of cohesive granulates made of sticky hard spheres.

In the following, I will characterise the three types of failure modes observed in the simulations, as depicted in Fig. 3.11(d-f), and the transitions between these failure modes. At first, to evaluate internal fracture quantitatively, I detected the microcrack activity in terms of the broken cohesive bonds in each strain step, of size $3 \times 10^{-4}$. In experiments, this quantity can be identified by monitoring acoustic emissions as a material sample deforms (*e.g.* [121, 122, 139, 140, 142, 160, 175]). I show the number of the microcracks, or broken bonds, in each strain window in Fig. 3.11(d-f), simultaneously with the stress-strain curves. Figure 3.11(d) shows that intense activity coincides with the peak stress for $\phi = 0.550$. This trend of acoustic activity is consistent with observations from rock experiments by using Clashach sandstone [175]. In Fig. 3.11(e), for $\phi = 0.500$, I detected fewer microcracks without a clear peak which I characterise as the ductile failure mode. At the lowest packing fraction of $\phi = 0.375$, in Fig. 3.11(f), abrupt spikes or bursts of activity accompany the intermittent stress drops, for example, near $\epsilon \simeq 0.22$ and 0.28. Such intermittency of microcrack activity is consistent with the observations of acoustic emissions accompanying compaction band formation in porous sandstones [121]. In all cases, the statistical properties of microcrack activity change near failure. Thus, I will focus on the spatial distribution of this quantity in the next subsection.

#### Entropy of microcrack activity near failure

The simulated cohesive granular system shows three distinct failure modes depending on the initial packing fraction: brittle failure, ductile failure, and anticrack or compaction band formation.

These reflect differences in the internal contacts and damage distribution in the samples during deformation. To measure the quantitative properties of the spatial distribution of microcracks, I calculated the normalised configuration entropy of the microcrack locations as compression proceeds. I could detect the concentration or localisation of damage through a decrease in this entropy [176]. This kind of metric, also known as the information or Shannon entropy, has been applied to experiments to predict the failure point of brittle and inhomogeneous materials, for example, in experiments involving plaster, wood and fibreglass [176, 177]. As an example of field observations, Ref. [178] has reported that a decrease in this entropy accompanied catastrophic failure in a galena mine [178]. Similarly, many other applications have reported entropy measurements, such as the analysis of generic random-fuse models [179] or earthquake time series [180–184]. In all these cases, the entropy reduces towards the failure point, as damage localises throughout a sample.

Next, I will explain the definition and the measurement method of the configuration entropy. I calculated the metric based on Refs. [176, 177]. At first, I divided the cylindrical system into $10 \times 10 \times 15$ cells, of size $2.2d \times 2.2d \times 2d$ (*i.e.* slightly shorter than cubic cells). I measured the fraction of microcracks, $q_i$, occurring in each cell $i$ in any given strain window. For these windows I divided the strain into 20 equal bins, with each having a width of approximately 0.01 in strain. The normalised entropy is then calculated as

$$S = -\frac{1}{S_0} \sum_i q_i \ln q_i. \tag{3.10}$$

Here, $S$ is normalised by the equipartition entropy, $S_0$, which is the entropy sum calculated by assuming that all the microcracks occurring in that strain window were completely randomly distributed in space. Note that empty cells outside the cylinder are excluded from this summation. This normalisation allows me to compare the entropy for different packing fractions even if the total number of microcracks differ in each sample. Under this definition, a random distribution of microcracks in space gives the maximum of $S = 1$. As the opposite limit, I would measure perfectly localised damage as $S = 0$. However, while I can detect any localisation trend through a decrease in entropy, the absolute value of $S$ can depend on the chosen cell sizes [177], which should be enough larger than the particle size but be enough smaller than other system scales. The magnitude of $S$ can also depend on the system size, as the relative widths of shear bands in cohesive granulates are known to depend on the sample size [135], but I did not explore this point in this study.

I show the strain evolution of the normalised entropy $S$ in Fig. 3.12 for various packing fractions. Simultaneously, I visualise the global microcrack activity (calculated as in Fig. 3.11). With an increase in strain, the microcrack activity localises in space and the rate of bond breakages

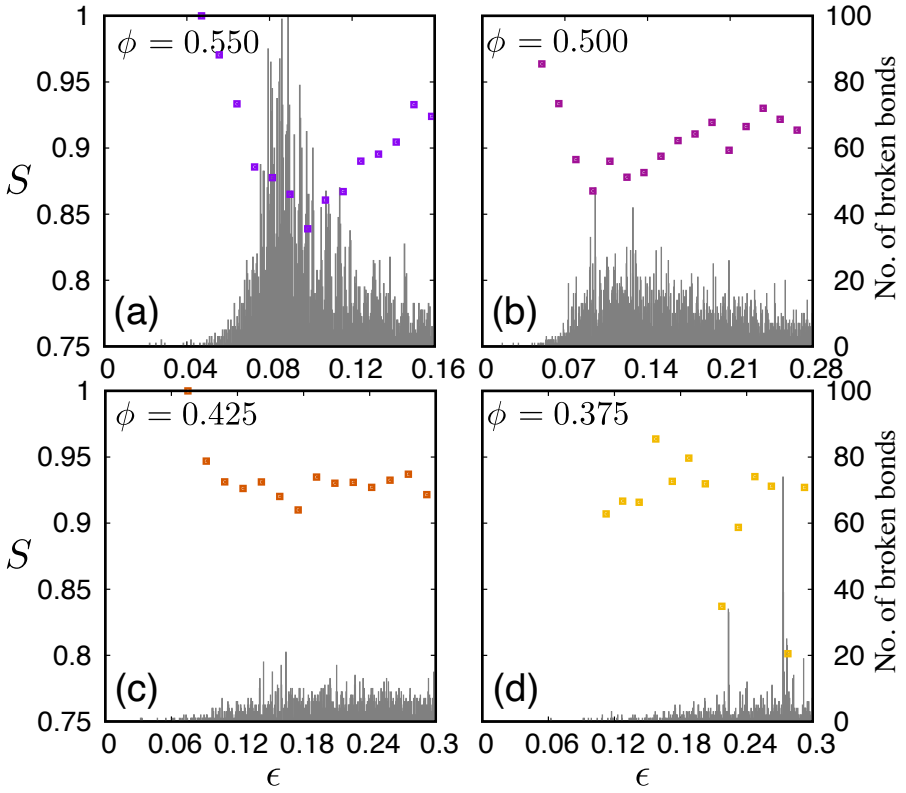


Figure 3.12: The normalised configuration entropy, $S$, characterises the localisation of damage during failure. Shown here is the strain-dependence of $S$ and its associated microcrack activity for model realisations with initial volume fractions, $\phi$, of (a) 0.550, (b) 0.500, (c) 0.425 and (d) 0.375. Values of $S$ were calculated using Eq. 3.10, by binning bond failure events over regular strain intervals. At high $\phi$ the drop in $S$ is simultaneous with the increase in activity as a shear-band forms, and shows precursor activity before the stress peak (compare with Fig. 3.11(d)). At intermediate $\phi$ the entropy drops to a lesser degree, and maintains a constant value as yielding proceeds. At the lowest $\phi$ the intermittent spikes of activity, coinciding with stress drops, show low $S$ and hence highly localised damage. This figure is reproduced from [108].

increases. The localisation of microcracks causes a reduction of entropy.

At a high packing fraction of $\phi = 0.550$, the entropy begins to drop before peak stress or peak microcrack activity is reached, as damage starts to form the localised plane of failure, as shown in Fig. 3.12(a). This precursor signal to shear-band formation is commonly observed in fracture experiments on heterogeneous brittle materials [176, 177]. Additionally, $S$ recovers to higher values after peak stress. This is because damage spreads through the entire system after a catastrophic failure. In some simulations, conjugate shear bands also occur as deformation proceeds. Both mechanisms will cause an increase in $S$. While the reduction in entropy is significant at high packing fractions (see Figs. 3.12(a, b)), the drop in entropy becomes less

pronounced as the packing fraction decreases. At $\phi = 0.425$, as shown in Fig. 3.12(c), the entropy keeps an almost constant value throughout the ductile deformation. In these cases, I can attribute a small drop in entropy to damage accumulation near the lower boundary (see Figs. 3.10(b2, b3)) due to the clamped boundary conditions.

At the lowest packing fraction of $\phi = 0.375$, I observed intermittent fluctuations in $S$ that accompany spikes in microcrack activity and the formation of anticracks. For example, this can be seen in Fig. 3.12(d), near $\epsilon = 0.22$ and 0.28, and this is a typical case of the lowest-$\phi$ samples. I have not made any further quantitative comparison of $S$ with any observations on anticracks. However, the intermittent fluctuation in the entropy of microcrack activity may be a general feature of compaction band or anticrack formation, as observed in compaction bands of sandstones [120, 121], snow [29], and foam [123].

**Transitions between failure processes**

In this subsection, I will try to identify three distinct failure modes by the following quantities: the evolution of their local packing fractions, the spatial profiles of their beads' coordination numbers and displacements, and variations in the spatial and angular correlations of microcracks.

To see changes in the internal structure before and after deformation, I examined the distribution of local packing fractions. The local packing fraction of particle $i$ is defined by $\phi_l = V_i/\tilde{V}_i$, where $V_i = (\pi/6)D_i^3$ and $\tilde{V}_i$ is the volume of its Voronoi cell (*e.g.* as in Refs. [185, 186]). I calculated the quantities by using the VORO++ code library [187]. The histograms are shown in Figs. 3.13(c, d) along with the result from a similar experiment, in which $\phi_l$ can be calculated from X-ray tomograms, and which shows a reversible Reynolds dilatancy [38, 107]. Fig. 3.13(b) on the experimental histogram compares the distributions at point 1 and 4 in Fig. 3.13(a). Intuitively, a compaction of the sample reduces the volume of the Voronoi cell, which may cause an increase in the local packing fractions. In contrast, I observed a shift of histogram, particularly toward a decrease in the local packing fractions. This reduction of local packing fractions may imply that particles align perpendicularly to a shear plane due to Reynold's dilatancy. Likewise, in simulations, I could observe a decrease in the local packing fractions through deformation only at higher initial packing fraction, for example, at $\phi = 0.580$ in Fig. 3.13(d). This effect could not be seen at lower packing fractions of $\phi = 0.375$ in Fig. 3.13(c). Thus, I presumed there is a cross-over between an increase and a decrease in the distribution of the local packing fractions.

To further examine the cross-over, I made the cumulative distribution functions for the corresponding histograms at $\phi = 0.580, 0.525$, and 0.375, as shown in Fig. 3.14. The cumulative distribution functions were calculated by $F(\phi_l) = 1 - \int_0^{\phi_l} P(\phi)d\phi$, for the probability distribution function $P(\phi)$. In Fig. 3.14(a), $F(\phi_l)$ shifts to lower volume fractions as compression proceeds

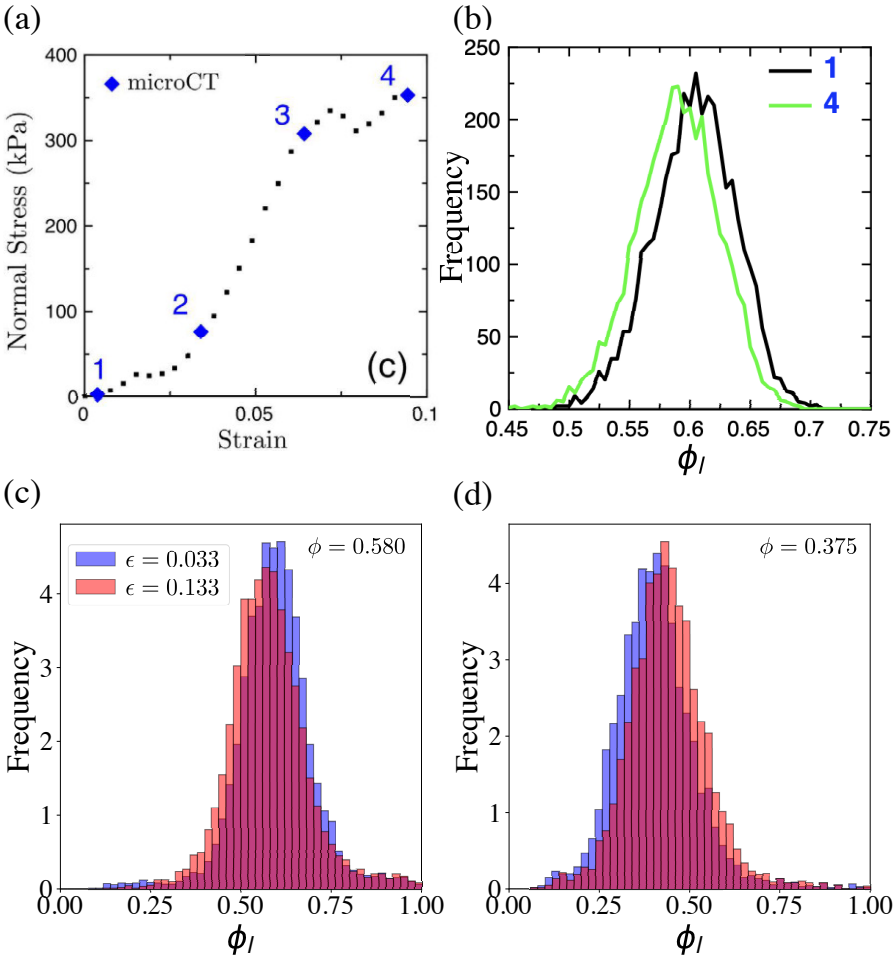


Figure 3.13: (a) Stress-strain curve measured in similar experiments [38] and (b) frequency of the local packing fraction in the experiments. Frequency of local packing fractions are shown at (c) $\phi = 0.580$ and (d) $\phi = 0.375$ in simulations.

for $\phi = 0.580$. With reducing the packing fraction, the tendency is reversed and $F(\phi_l)$ shifts to higher volume fractions at $\phi = 0.375$ (Fig. 3.14(c)). An intermediate point between dilation and compaction seems at $\phi = 0.525$ in Fig. 3.14(b), and the two curves collapse.

To identify the cross-over point closely, I also checked the strain dependency of the median of the local packing fractions $\langle\phi_l\rangle$ at $F = 0.5$. I plotted $\langle\phi_l(\epsilon)\rangle - \langle\phi_l(0)\rangle$ for different initial packing fractions, as shown in Fig. 3.14(d). For this results, the negative sign corresponds to a dilatant response and the positive one corresponds to a compressive response. The cross-over happens between between $\phi = 0.500$ and 0.525. It is worthy of special mention that this cross-over point coincides with the transition point from the brittle failure, *via* shear band formation to a plastic failure. This transition can also be described by the sign of the dilatancy factor $\beta$, which derives from the ratio of the plastic volumetric to axial strains under deformation in

geomechanics [188, 189]. With the criteria, clear shear bands appear for $\beta > 0$, and compaction bands or homogeneous cataclastic flows are seen for $\beta < 0$ [162, 189].

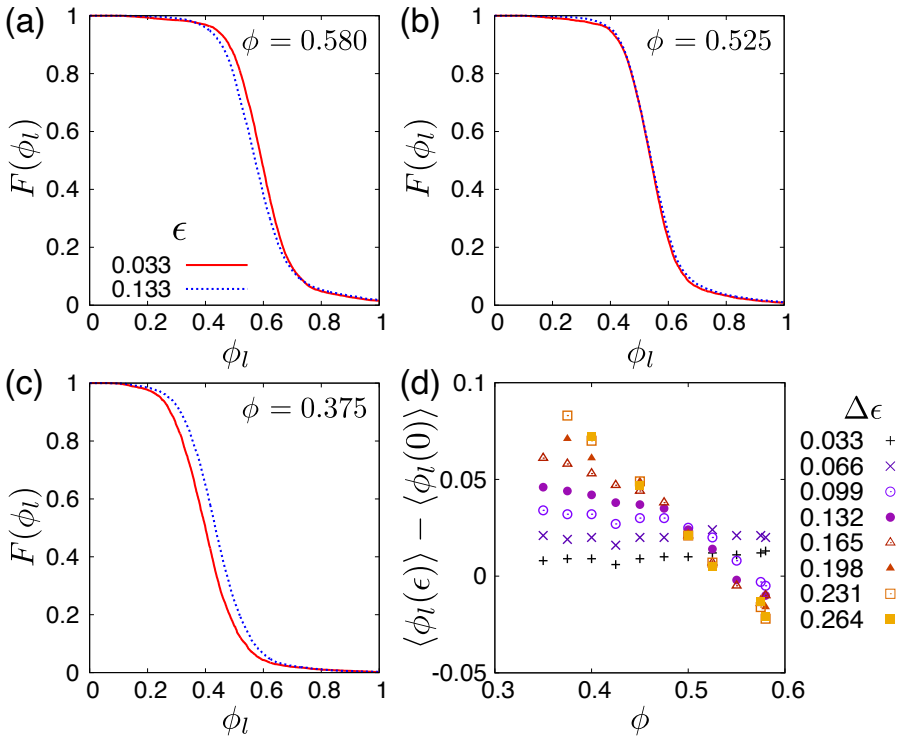


Figure 3.14: Simulations demonstrate dilatancy at large enough $\phi$, but not for more porous materials. I show here the complementary cumulative distribution function of the *local* packing fraction for (a) $\phi = 0.580$, (b) 0.525 and (c) 0.375 and strains of $\epsilon = 0.033$ (red solid lines) and 0.133 (blue dotted lines). The shift of the distribution from left to right with an increase of strain implies the compaction of a system. The shift for the opposite direction implies dilation. (d) At various strains I can identify the median $\phi_l$ as the the half-way point of such curves, *i.e.* where $F = 0.5$. Plotting how this median, $\langle\phi_l(\epsilon)\rangle$, changes from its initial value, $\langle\phi_l(0)\rangle$, highlights the dilatancy. Here, a positive dilatancy factor is implied for $\phi = 0.525$ and above, which is also where shear bands are seen. This figure is reproduced from [108].

Next, I quantitatively analysed the anticrack formation observed at lower packing fractions. As described in Sec. 3.2.1, the definition of anticracks is a failure mode with the displacement profile of a mode-I crack, but with the reversed sign [17, 25, 26]. They can be detected through localised reductions in porosity [26], microcrack activity [122], damage accumulation [162], strains and displacements [123]. At first, I characterise the damage localisation by plotting the coordination number profile of the representative simulation of $\phi = 0.400$. I depicted a snapshot of the sample in Fig. 3.10(c), where an anticrack develops from right side to left side between strains of 0.11 and 0.16. As shown in Fig. 3.15(a), the anticrack formation reduces the average number

of contacts between $z/H = -0.6$ and $-0.9$. At the same position of the same simulation, I plotted the vertical-displacement profile in Fig. 3.15(b). I could observe the discontinuity of the vertical displacement at the position of the anticrack, which is consistent with its definition. In both cases, I plotted the positions in an undeformed coordinate system, or Lagrangian reference frame, normalised by the original sample height $H$ [123].

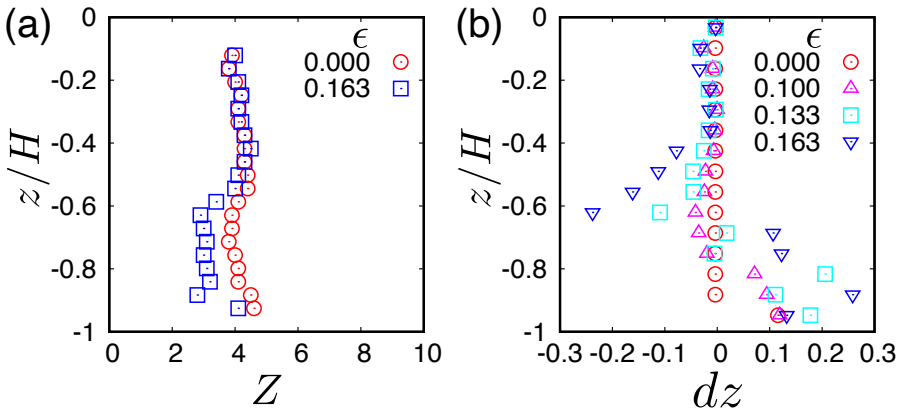


Figure 3.15: Detection of an anti-crack at $\phi = 0.400$. I show here how the horizontally-averaged (a) coordination number $Z$ and (b) vertical displacement $dz$ of particles in a sample changes under compression. In both panels the positional information is plotted using a Lagrangian or undeformed reference frame (as in *e.g.* [123] for anti-cracks in foam), to allow features to be more easily compared. At a depth of between 0.6 and 0.7 times the sample height an anti-crack forms. This can be seen by a local reduction of the coordination number and by the opposite signs of the $z$-displacement profile above and below the anti-crack. This figure is reproduced from [108].

Finally, I showed the correlation analysis for the spatial distribution of microcrack activities in the various failure modes. I calculated the correlation function in the following steps. At first, I calculated the displacement vectors between all possible pairs of broken bonds. Next, to capture the difference between shear and compaction bands, I made a density map between the length $\delta_{ij}$ and polar angle $\theta_{ij}$ (*i.e.* angle measured from the axis of compression) of these pair-wise displacement vectors. I plotted the density map in Fig. 3.16(a),(c), and (e) at each initial density. However, the colour bar in these figures suggested that the number of broken bonds completely differed depending on the initial packing fraction. Then, I randomly generated the same number of broken bonds at each density within the cylindrical sample. I normalised the density map by a correlation function calculated similarly but for these random positions. The normalised density maps are shown in Figs. 3.16(b),(d), and (f). Figs. 3.16(a,b) show the case of a shear band at $\phi = 0.580$. Here, the strong correlations at $\theta_{ij} = \pi/4$ and $3\pi/4$ imply the formation of shear bands along diagonal planes at 45° to the direction of compression. Figs. 3.16(c,d) show

the case of diffuse plastic damage at $\phi = 0.500$, showing weaker correlations in any orientations. The last case is given in Figs. 3.16(e,f) at $\phi = 0.400$. The correlation at $\theta_{ij} = \pi/2$ develops, showing that the broken bonds localised in the horizontal direction.

### 3.2.4 Summary and discussion

In this study, by using the model constructed in Sec. 3.1, I explored the detail of the failure process of a cohesive granular system. By varying the initial density of the system, which changes the distribution of the granular particles and the cohesive bonds connecting each other, I showed that the model could reproduce the variety of failure modes: shear banding, plastic creep and anti-cracks or compaction bands. These three types of failure are observed in snow [17, 29, 166], foam [123], colloidal gels [132, 170, 171], powder aggregates [130, 146, 168, 169], sandstone [121, 122, 142, 157–159, 163, 189] and so on.

To characterise these failure modes, I demonstrated the shift in the sign of the dilatancy factor from brittle (positive) to plastic failure (negative). This result is consistent with compressional tests on sandstone [189]. I also showed that anti-crack formation is associated with intermittent stress drops, strain and damage localisation. The damage localisation coincided with the temporal reductions in the positional entropy of microcrack activity. Furthermore, I described the particularly strong power-law scaling of the elastic modulus and compressive strength of cohesive granular materials with the density of bonds (as with [110]), effectively described by $Z\phi$. The results lend support to the developing idea of how force chains control the failure processes in cohesive granular systems [130–133], by controlling the distribution and density of stress concentrations.

There remains wide scope for further application of this model. Its parameters can be changed to reflect different materials, from snow (low $\phi$, weak bonds) to sandstone (high $\phi$, stiff bonds with strength depending on cement or matrix content) and artificial composites like the materials that directly inspired it.

As a future perspective of this work, one could explore system size effects, as was done for shear band width in Ref. [135]. A similar effort could explore the effects of varying the volume fraction of the bond material, to allow for a broader characterisation of rocks, such as in [37, 113].

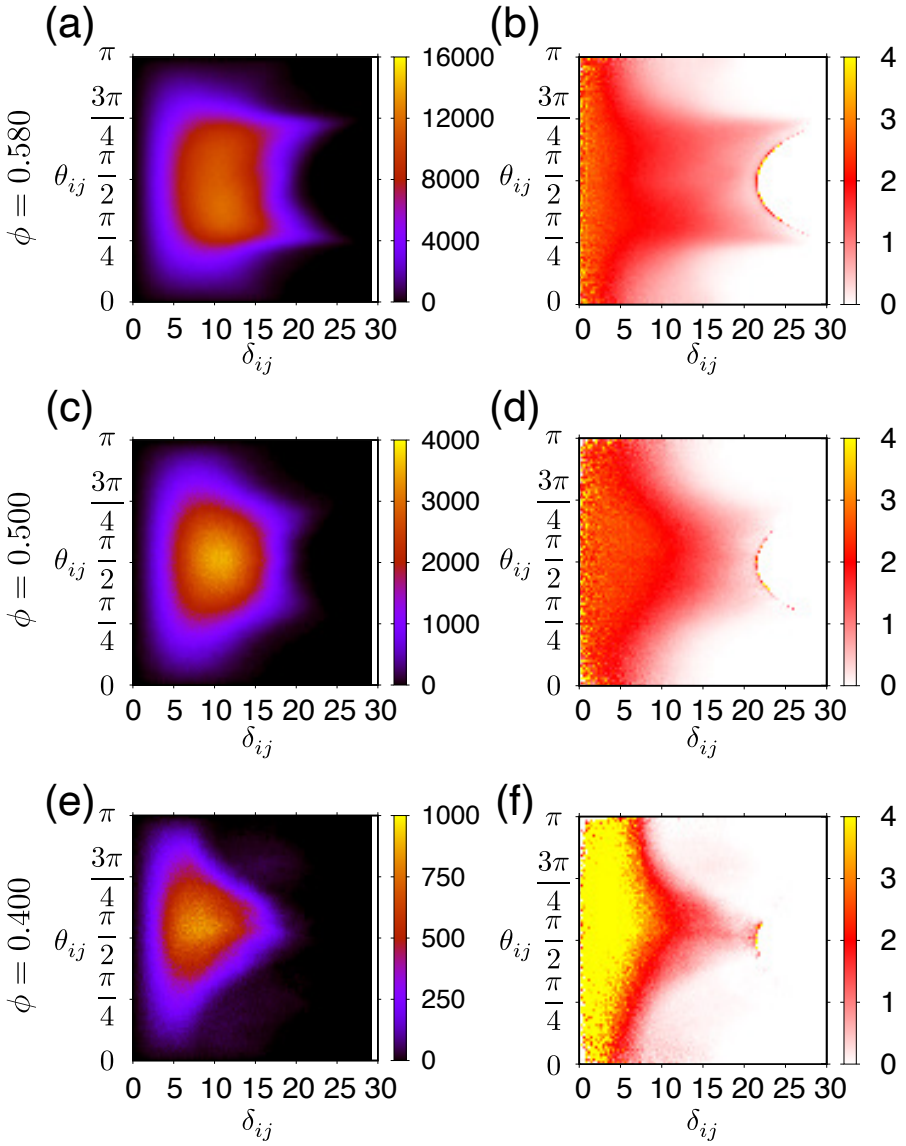


Figure 3.16: Correlation analysis of damage in various modes of failure. Shown on the left are density maps giving the relative likelihood of finding pairs of bond breakages at distances $\delta_{ij}$ and angles $\theta_{ij}$ from each other. Panels on the right show the same information, normalised by a similar map generated from pairs of points randomly distributed within the volume of the sample. In this representation, bond breakages happening entirely at random would give a correlation value of 1. Note that the cylindrical shape of the samples constrains the choices of allowed pairs of bonds and particles, and is responsible for the curve of noise around $\delta_{ij} = 20$. Here, panels (a) and (b) show the brittle failure at $\phi = 0.580$, (c) and (d) are at $\phi = 0.500$ and highlight ductile deformation, while (e) and (f) present data from an anti-crack at $\phi = 0.400$. This figure is reproduced from [108].

## 3.3 Prediction of failure timing of cohesive granular materials

In this section, I will describe how I applied the random forest method to attempt to predict the failure timing of quasi-statically deforming materials. The random forest method is a kind of ensemble learning method, which uses an ensemble of individual decision trees [190]. I prepared sample data from numerical simulations simulating cohesive granular material (as in the previous Sec. 3.2). As a result, I succeeded in predicting the failure timing accurately under the condition that the variation among samples is small, specifically for initially dense samples. The model could not predict the failure timing for lower density samples, which may be due to fewer training sets. However, this study suggested that not only the yielding stress but also the cumulative number of acoustic signals, i.e., the amount of damage accumulation in the system, were critical features in predicting the failure timing.

### 3.3.1 Introduction to random forest method

As described in Sec. 3.2.1, the failure of cohesive granular materials can be observed in many contexts, such as geological situations or industrial materials [137]. Therefore, predicting or controlling the failure timing of such materials is desirable [191, 192].

Recently, machine learning methods have been getting much attention [193]. One of its methods, the random forest method [190] is an ensemble algorithm that makes an average prediction from a set of decision trees. In short, the training data are split at each node of a given tree, which compares the data to a threshold with a threshold for a particular attribute. At the next node, each of these groups is further split using a threshold on a different attribute and so on, until in each leaf (end of the decision tree) the value of the target variable (time to failure) is the same, or when further splitting does not improve predictions (fixed by variance reduction or maximum depth of trees). Now, the training data for each tree is selected from the full training set using bootstrapping. Bootstrapping acts as a mitigation strategy against outliers in the training set, as some rows are bound to be repeated. In this way, each tree sees a different randomly selected part of the full training set, giving the ensemble of such trees.

The random forest method has been used to predict the timing of stick-slip from the results of sand experiments [58]. The study accurately predicted the timing of a simple cyclic motion of a rigid bar, which repeats sticks and slides against the sand, in the experiment of pulling a rigid bar compressed in the sand. As another example, the technique has been applied to predict the onset of failure in the fibre bundle model [194]. In this case, it was best predictable for the

quasi-brittle failure mode. However, these examples are simplified cases of fracture. A numerical model constructed in this chapter (Secs. 3.1 and 3.2) can be compared directly with corresponding experiments [38] and is more realistic in terms of using parameter values from the experiments. In this study, I will report the preliminary results of predicting failure by applying the random forest method to results from my numerical simulations of cohesive granular materials [108]. In addition, I will explore the initial packing fraction dependence of prediction and extract feature importance in predicting failure timing.

### 3.3.2 The model

#### Preparation for samples

In this study, I prepared datasets in the same way as Sec. 3.2.1. Here, I review the essential features of the results. I consider a cohesive granular system with a cylindrical shape formed by glass beads attached together by polymer bonds. The elastic response of this material under uniaxial compression has been investigated experimentally [38], and I have reproduced the deformation process of this material by using DEM simulations [108]. I show a schematic diagram of this system in Fig. 3.17(a). The particles coloured in blue correspond to the bulk particles, and the red particles correspond to the upper and lower walls. The particles of the upper wall are fixed in position, and the particles of the lower wall are moved upwards to apply uniaxial compression to the system.

I show the stress-strain curves under uniaxial compression at different initial densities $\phi$ of the system in Fig. 3.17(b). When a small amount of strain is applied, the stress follows a linear response against strain, and the system behaves elastically. When the strain is further increased, the system yields as the stress reaches its maximum value, leading to failure. When the initial density is large, the system fails with a large stress drop, while the stress drop becomes smaller as the initial density decreases. The difference in the stress-strain curves at several $\phi$ reflects the distinct failure processes, which are shown in Figs. 3.17(c-e). At the higher initial density of $\phi = 0.580$ in Fig. 3.17(c), a shear band develops across the entire system, and the system deforms in a brittle manner. The whole system deforms uniformly at the middle density of $\phi = 0.500$ in Fig. 3.17(d). These results are consistent with the laboratory experiments for rocks of different densities [188]. Further decrease in the initial packing fraction causes another failure mode of compaction band, as shown in Fig. 3.17(e).

In general, many small cracks are generated during the failure processes of brittle rocks. In laboratory experiments, these microcracks are detected as acoustic emissions (AEs), and their spatial development has been investigated [22, 120, 121, 140, 141, 175]. Initially, microcracks are

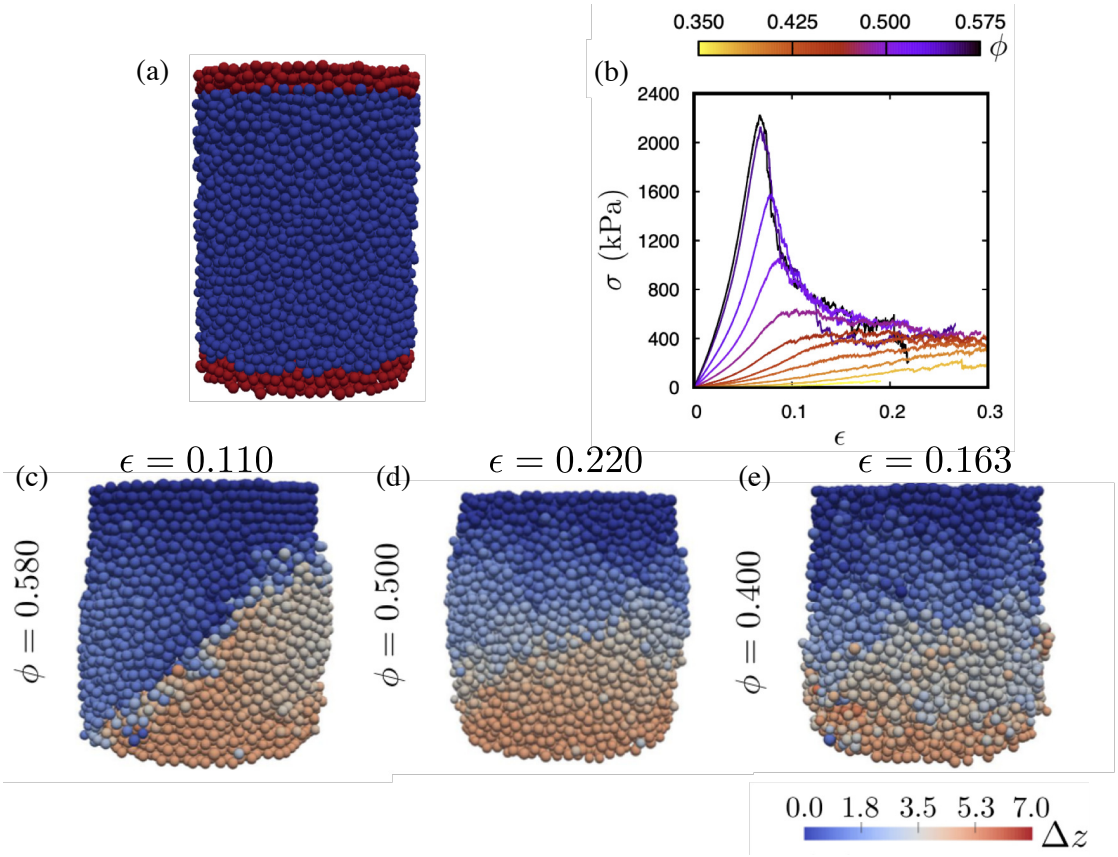


Figure 3.17: (a) Schematic picture of simulation setup (reproduced from Fig. 3.9(a)). (b)The stress-strain curves depend on the initial packing fraction, $\phi$ (reproduced from Fig. 3.11(a)). (c-e) Deformation and failure modes of cohesive granular media also depend on $\phi$ (reproduced from Fig. 3.10).

randomly distributed in space. As strain accumulates, they gradually concentrate on a plane and eventually lead up to shear deformation on that plane. Therefore, detecting the spatial evolution of microcracks can plausibly enable us to predict the onset of failure timing. In my system, a fracture of the cohesive bond connecting the glass beads corresponds to a microcrack in rock experiments. As a statistical property, I tracked the time evolution of the cumulative number of cohesive bond fractures, representing the amount of damage accumulation in the system.

### Random forest method

The random forest method was implemented by the Scikit-learn library [195] in Python 3.6. The following parameters are used in setting up the random forest method: the maximum depth of each decision tree (the depth of the conditional branching) and the number of decision trees. In this study, I used a depth of 10 and the number of decision trees of 100. I checked that small

variations around the chosen parameter values do not improve predictions.

Following the procedure described in Sec. 3.2, I prepared five datasets at each initial density of samples, $\phi$. I used four of them for training the model, i.e. as training data, and one for evaluating the performance of the random forest method, test data. Thus, training data is independent of test data. Each dataset includes a time series of six features as descriptors:

- $\sigma$: Stress within the small strain windows $\Delta\epsilon(= 4.2 \times 10^{-4})$
- $\dfrac{d\sigma}{dt}$: Time derivative of stress in each time window
- $\dfrac{d^2\sigma}{dt^2}$: Second derivative of stress in each time window
- $\bar{\sigma}$: Mean value of stress within $100\Delta\epsilon$
- var($\sigma$): Variance of stress within $100\Delta\epsilon$
- AE: Cumulative number of broken cohesive bonds at each time step (accumulation of damage in the system)

Furthermore, I extracted feature importance for the prediction using the python function. The feature importance values are defined by the mean and standard deviation of accumulation of the impurity decrease due to a particular feature within each tree. The impurity (Gini impurity) is an indicator that measures how much of the target is not classified for each node, and is calculated by subtracting the sum of the squared probabilities of each target from one [196, 197].

In this study, I predicted the onset of failure timing with the random forest method in the following way. First, I defined failure timing as the value of strain that gives the maximum stress in the stress-strain curve. I built five datasets under the same conditions but with different initial configurations of granular particles. Then, I split them into four for training data and one for test data. I used the training data to train the random forest method with all six time series (given in the itemised list above) as features, along with another measure of the time to failure as the goal to be predicted. On the other hand, for test data, I excluded only the strain to failure, which is the objective variable, and fed the other features into the trained model. Finally, the random forest method was used to predict the remaining strain before the onset of failure. I also investigated the dependence of predictions on the initial packing fraction $\phi_i$ ranging from 0.450 to 0.580.

### 3.3.3 Prediction results

#### Stress-strain curves

I show the results of the prediction by the random forest method in Fig. 3.18. Here, I plotted the stress as an example amongst the several features used to visualise the predicted strain to failure. At the higher initial density of $\phi = 0.575$, the test data (coloured in blue) agree with the prediction (coloured in green). On the other hand, the fluctuation of the prediction increases as the initial density decreases. This significant fluctuation in the predictions at lower density is caused by the low reproducibility of stress-strain curves, depending on the initial configurations, which is confirmed by a large deviation between the test data and the mean value of the training data (coloured in red). Thus, the prediction accuracy decreases as the initial packing density decreases. To improve the prediction accuracy, I would need to build a large number of datasets to reduce the deviation related to the initial configuration.

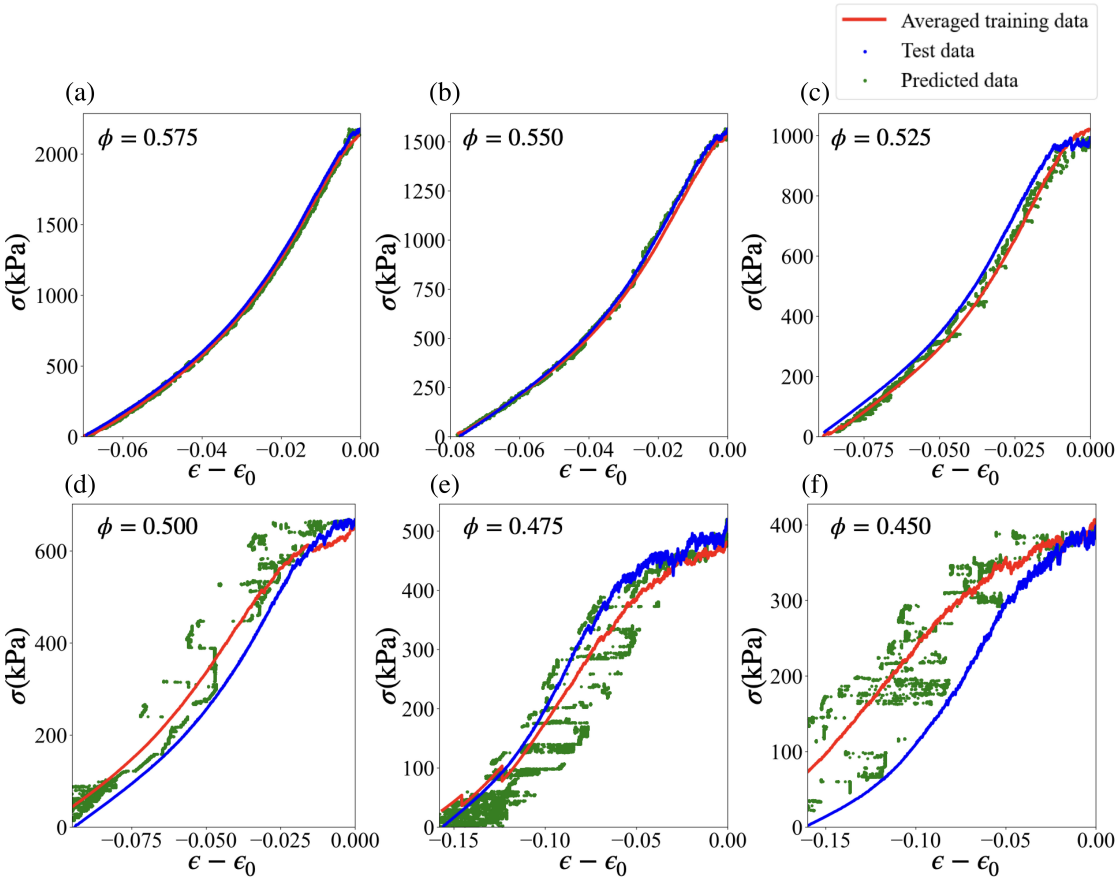


Figure 3.18: Stress-strain curves for the averaged training data (red), test data (blue), and predicted time to failure (green) at different initial packing fractions, $\phi$. Stress is plotted against strain to failure $\epsilon - \epsilon_0$, with failure strain $\epsilon_0$.

**Feature importance of predicting failure**

Next, I show the feature importance for predicting the strain to failure in Fig. 3.19. At higher initial densities (Figs. 3.19(a-b)), the stress is estimated to be an essential feature, which means that the system fails when a well-defined yield stress is reached. On the other hand, at lower initial densities (Figs. 3.19(c-f)), the important feature is shifted to other features, such as the mean value of stress, the variance of stress, and the accumulated damage or acoustic emissions. This transition suggests that statistical properties of stress and the damage accumulation inside the system are more important features for predicting failure, rather than the yield stress, at a lower density system, while a brittle system with higher density fails at constant yielding stress. However, the results obtained are not detailed enough to make a strong claim to this end, since the number of training datasets is limited.

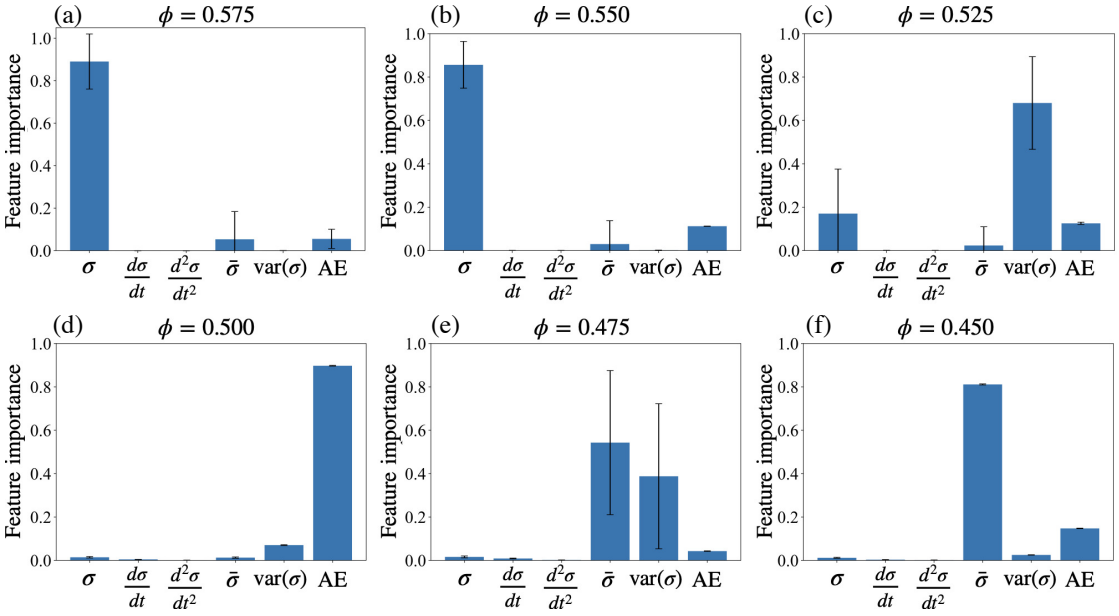


Figure 3.19: Feature importance for prediction at different initial packing fractions.

### 3.3.4 Summary and discussion

The quasi-static deformation process of a cohesive granular system was simulated numerically at several initial densities. I applied the random forest method to predict the failure timing of the system. The prediction accuracy of failure timing changed with the initial density of the system.

In the parameter range where the initial density is high and the system breaks in a brittle manner, the algorithm accurately predicts the strain to failure based on a well-defined yield stress. On the other hand, the algorithm cannot as accurately predict the strain to failure at the lower initial density system, where the system deforms plastically due to a significant fluctuation

in the datasets depending on the initial particle configuration. It should be noted that this trend goes against what is reported for predictability of disordered solids [198]. In the literature, the predictability of failure tends to be reduced at higher density, since the amount of precursory signal (acoustic emissions) are reduced. However, in this study, I could detect acoustic signals at high resolution even at higher density. Furthermore, the higher the density, the less freedom there is in the initial particle configuration, and the changes in realisations become more limited. Thus, the sample always breaks in the same manner, causing a high predictability.

I also extracted the feature importance for predictions. The essential features shifted from stress to mean stress, variance and accumulation of damage in the system as the initial density of the system decreased.

# Chapter 4

# Shear simulations of cohesive granular particles under a constant pressure

I have discussed the mechanical properties of cohesive granular materials in Chapter 3. This chapter will now address the rheology, or the shear flow, of granular particles through molecular dynamics simulations (hereinafter referred to as MD simulations) as another problem of granular materials. Revealing the rheological behaviour of granular particles is essential not only in physics but also in the earth sciences [1–3]. In particular, density is a critical factor in determining rheological behaviour [199, 200]. In Sec. 4.1, I will investigate the effect of density and inter-particle contact on the rheology of a granular system under constant pressure, where the system's density can change over time. In contrast to the previous chapter, I will adopt a harmonic potential for the inter-particle potential and implement and perform MD simulations in a 2D system. The results described in Sec. 4.1 form the basis of reference [111]. In Sec. 4.2, I will extend the model to include a more realistic interaction potential and perform 3D simulations using an inter-particle potential based on DMT contact theory. There, I will present some preliminary results, including the spatio-temporal evolution of voids.

## 4.1 Rheology of cohesive granular particles under constant pressure in 2D

### 4.1.1 Introduction

Understanding the rheological behaviour of granular materials is important for applications in industry and other fields [1–3]. A system density exerts a strong control over the rheological behaviour of granular particles. Thus, the system with a constant density, i.e. where the volume and the number of granular particles are kept constant, has been intensively studied, and a critical

density, known as the jamming density, has been reported to drastically change the rheology [199, 200]. Below the jamming density, the viscosity is proportional to the shear-rate [201], and kinetic theory is a powerful tool for understanding the rheology of dilute and moderately dense cases [202–210]. Above the jamming density, the particle contacts become dominant, and the shear stress has a finite yield stress, even for a low shear-rate limit. At the vicinity of the jamming density, critical scaling has been reported [199, 200]. Another important setup for investigating the rheology is the system under constant loading. This case can be observed in natural situations, such as earthquake faults. Under this condition, the friction coefficient is a monotonically increasing function of the inertial number, which is the dimensionless shear-rate defined by the ratio of the shear stress to the normal stress [42–44, 211–213]. Furthermore, a frictional force between granular particles changes this dependency [43]. The rheology for frictional grains obey $(\mu - \mu_c) \propto I^{1/2}$, while one for frictionless grains shows a linear response. Here, $\mu$ is the frictional coefficient, $\mu_c$ is the friction coefficient in the zero shear-rate limit, $I$ is the inertial number.

As I introduced cohesive interactions in Sec. 1.1, they can be observed in certain situations, such as the van der Waals force for fine powders [6, 8], the capillary force for moderately humid particles [9–14], and the electromagnetic force for magnetic beads [15]. The existence of cohesive interactions can trigger nucleation or cluster formation of particles [214–216] and then alter the rheology of granular flows. Several patterns can appear depending on the shear-rate and the system density [53, 217]. The dissipation between collisions increases when the granular temperature is comparable to the magnitude of the attractive forces [218–220]. Recently, studies on the rheology of cohesive granular particles under a constant volume condition have also been reported [45, 46, 48, 50, 217]. These show that there exists a well-defined yielding stress, even below the jamming density [30, 45, 46, 49], that does not appear for noncohesive systems. Irani et al. [45, 46] observed a minimum stress below the jamming density under constant volume conditions (see Fig. 4.1). This result differs from that of noncohesive cases. On the other hand, I have mentioned that the rheology under constant loading is different from that under constant density. However, there remains a lack of understanding of the rheology of granular materials under constant loading, in particular, of those with cohesive interactions. In this study, I will focus on the rheology of cohesive granular particles under a constant loading environment.

### 4.1.2 The model

I will consider a 2D system and prepare 2,000 bidisperse frictionless disks in a 50:50 ratio with diameters $d_1(\equiv d)$, $d_2 = 1.4d$ and masses $m_1(\equiv m)$, $m_2 = 1.4^2 m$. I fix the dispersity as 1.4 to

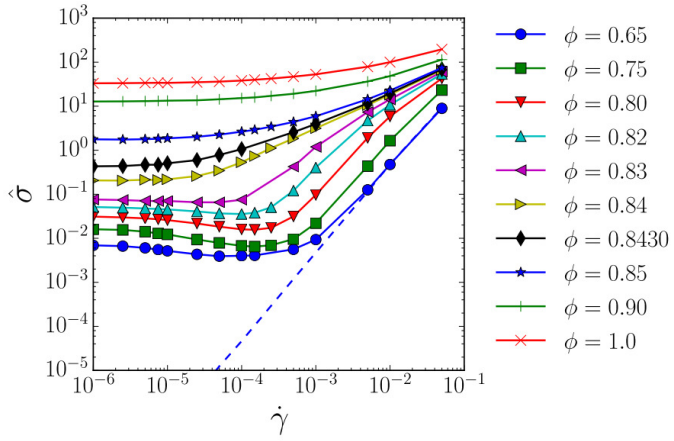


Figure 4.1: Flow curves for cohesive grains under constant volume conditions showing how the stress $\hat{\sigma}$ depends on strain rate $\hat{\gamma}$. Below the jamming density, flow curves show minimum values, which have not been observed under constant loading conditions. This figure is reproduced from Ref. [46].

avoid crystallisation (see Sec. 2.1). I construct boundary walls with length $L_x = 42d$, building the wall up using the smaller particles aligned in the $x$-direction with interval $d$. To efficiently apply shear without inducing slip along the wall, I also align the particles to form triangles with sides $6d$, as shown in Fig. 4.2. I compress the boundary walls with the magnitude of force $PL_x$ in $y$ where $P$ is the confining pressure on the system. In addition, I move walls along the $x$-direction with velocity $V$ for the top one and $-V$ for the bottom one, with imposing a periodic boundary condition in the $x$-direction. I define the system height $L_y$ by averaging the height over time since the system size in the $y$-direction fluctuates under the constant pressure condition.

The interaction between particles is described by the sum of the elastic force from their inter-particle potential and dissipative forces as described in Sec. 2.2.2. In this study, I select the inter-particle potential as

$$U(r_{ij}) = \begin{cases} \epsilon\left[\left(1-\frac{r_{ij}}{d_{ij}}\right)^2 - 2u^2\right] & \frac{r_{ij}}{d_{ij}} \leq 1+u, \\ -\epsilon\left(1+2u-\frac{r_{ij}}{d_{ij}}\right)^2 & 1+u < \frac{r_{ij}}{d_{ij}} \leq 1+2u, \\ 0 & \frac{r_{ij}}{d_{ij}} > 1+2u, \end{cases} \tag{4.1}$$

so that I can introduce a weak cohesive interaction that acts only in a short range, as shown in Fig. 4.3. Here, $d_{ij} \equiv (d_i + d_j)/2$, $r_{ij}$ is the distance between the $i$th and $j$th particles, $\epsilon$ relates to the stiffness of the particles, and $u$ characterises the depth and width of the potential well. This potential is used not only for cohesive grains but also for attractive emulsions [45, 47, 48]. Note that in contrast to the bonds considered in Chapter 3, this cohesive interaction forms bonds that

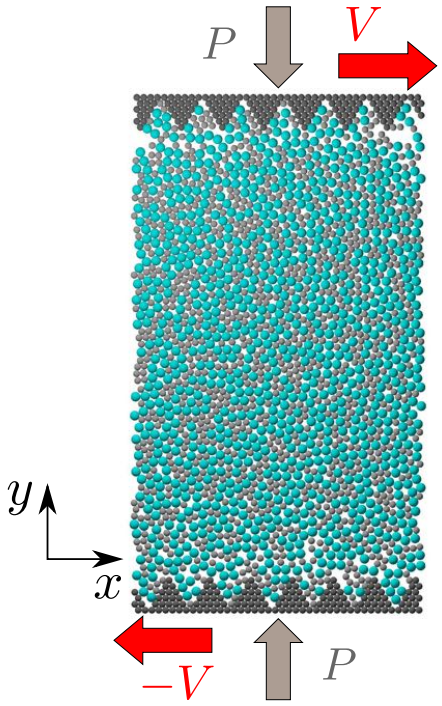


Figure 4.2: Simulation model for the shear simulation in 2D. I confine bidisperse particles between the top and bottom boundary walls by applying a normal pressure in the $y$-direction. A shear deformation is applied to the system by moving the walls in the $x$-direction. This figure is reproduced from Ref. [111].

can break and reform as frequently as necessary. In addition, I consider the dissipative force written in Eq. (2.4), which acts when two particles overlap each other. The magnitude of the dissipative force depends on the relative velocity of the two particles. The force acting on the $i$th particle is expressed as

$$\boldsymbol{F}_i = \sum_{j \neq i} \left[ -\boldsymbol{\nabla}_i U(r_{ij}) + \boldsymbol{F}^{\mathrm{diss}}(\boldsymbol{r}_{ij}, \boldsymbol{v}_{ij}) \right]. \tag{4.2}$$

In addition, I used overdamped boundary walls, with dissipation rate $\zeta^{\mathrm{wall}} = 10\sqrt{m\epsilon}/d$, to accelerate the simulations. The time evolution of the walls is described by

$$F^{\mathrm{wall}}_{\mathrm{top}} - PL_x - \zeta^{\mathrm{wall}} \dot{y}_{\mathrm{top}} = 0, \tag{4.3}$$

$$F^{\mathrm{wall}}_{\mathrm{bottom}} + PL_x - \zeta^{\mathrm{wall}} \dot{y}_{\mathrm{bottom}} = 0. \tag{4.4}$$

Here, $F^{\mathrm{wall}}_{\mathrm{top}}$ and $F^{\mathrm{wall}}_{\mathrm{bottom}}$ are calculated by summing the vertical components of all the forces applied on the top and bottom walls, and $y_{\mathrm{top}}$ and $y_{\mathrm{bottom}}$ describe the positions of the top and bottom walls in the $y$-direction.

All the quantities are non-dimensionalised in terms of $m$, $d$, and $\epsilon$. In the following, asterisks represent dimensionless variables or parameters constructed by these units. For example, the

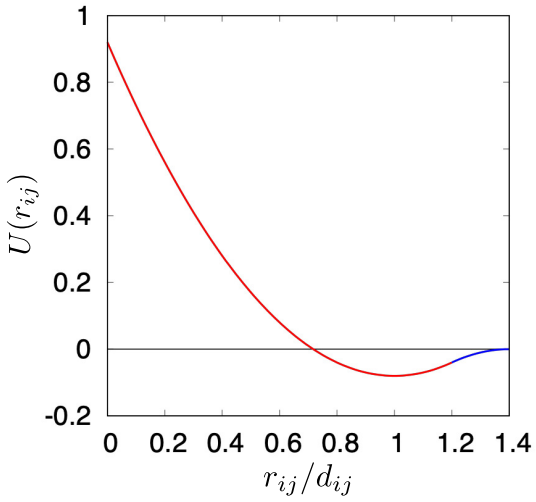


Figure 4.3: The inter-particle potential expressed in Eq. (4.1). Here, I choose $\epsilon = 1.0$, $d_{ij} = 1.0$, and $u = 0.2$. The red curve is a downward convex parabola, as described by the first case in Eq. (4.1), and the blue curve is one with a convex upward as written in the second case.

wall velocity $V$ is described as $V = V^*\sqrt{\epsilon/m}$ with the dimensionless velocity $V^*$. I select the dimensionless dissipation rate as $\zeta^* \equiv \zeta d/\sqrt{m\epsilon} = 2$ as in previous studies [45,46]. This dissipation rate approximately corresponds to a restitution coefficient of 0.135, representing certain materials such as copper and aluminium. It should be noted that the choice of the restitution coefficient does not markedly affect the rheology [42].

In this study, I make the initial condition in the following way. At first, I compress the bulk system without applying a shear ($V^* = 0$). During this process, I introduce a weak cohesive interaction, $u = 2 \times 10^{-4}$. I run this simulation until the system reaches a steady state and select the resulting particle configuration for the initial condition.

### 4.1.3 Phase diagram

In a steady state, a set of control parameters specifies the system's behaviour. By varying confining pressure $P$, cohesive force $u$, and shear velocity $V^*$, I determined four steady states: (i) uniform shear phase, (ii) oscillation phase, (iii) clustering phase, and (iv) shear-banding phase, as described below.

The long-time averaged velocity profiles in the $y$-direction are linear in phases (i) and (ii). In phase (i), all the particles flow following the linear velocity profile, on average, and uniform shear is found throughout the domain, without significant departures or fluctuations. While the long-time averaged behaviour of phase (ii) is similar to that of phase (i), I detect a difference in the high-frequency behaviour. In particular, phase (ii) has large velocity fluctuations in the bulk

and shows intermittent backward movements.

To characterise phase (ii), I focus on the region near $y = L_y/4$, which is half-way between the centre of the system and the top wall, with width $L_y/31$ and calculate the average velocity $\bar{v}_x^*$ in this region. I select the region since its long-time averaged velocity is not zero and yet the effect of the walls is relatively small in this regime. I define the integrated mean displacement $\Delta(t)$ in the region as

$$\Delta(t) \equiv \int_0^t dt' \bar{v}_x(t'). \tag{4.5}$$

I show the time evolution of $\Delta(t)$ in phases (i) and (ii) in Fig. 4.4. The oscillation phase (ii) has large fluctuations, and the behaviour differs from the one in phase (i). The intermittent decrease in $\Delta(t)$ indicates backward motion, reducing the deformation energy of the shear.

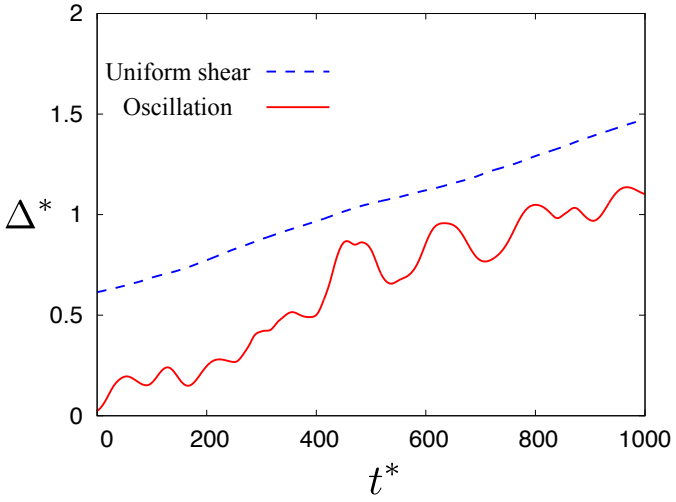


Figure 4.4: Time evolution of the integrated mean displacement $\Delta$ (Eq. (4.5)) in the region near $y = L_y/4$ for phase (i) (uniform shear, coloured in blue) with $u = 2 \times 10^{-4}$, $P^* = 10^{-3}$, and $V^* = 10^{-3}$, and phase (ii) (oscillation, coloured in red) with $u = 2 \times 10^{-1}$, $P^* = 10^{-3}$, and $V^* = 10^{-3}$, where $t^* \equiv t\sqrt{\epsilon/md^2}$ and $\Delta^* \equiv \Delta/d$. This figure is reproduced from Ref. [111].

To further quantitatively analyse the difference between phase (i) and phase (ii), I also investigate the distribution functions of the velocity fluctuation of the particles. Here, I define the velocity fluctuation of particle $i$ as the deviation from the local average flow velocity $\bar{v}_x(y_i)$, where $y_i$ is the $y$-coordinate of particle $i$. For this, I only consider the region of $-L_y/4 < y < L_y/4$, to reduce the boundary effect. Fig. 4.5 exhibits the probability distribution of the velocity fluctuation at several values of the wall velocity $V^*$. The velocity fluctuation increases with the decrease in wall velocity. Negative fluctuation with $\delta v_x^*/V^* < -1$ implies that a fluctuation is larger than the average flow velocity and that the averaged partricle motion has the backwards movement. As $V^*$ decreases, the probability distribution for velocity fluctuation develops a long tail over

the negative domain. Therefore, the probability of backward motion is more significant. I judge that a state is in the oscillation phase (phase (ii)) if the probability of $|\delta v^*/V^*| > 1$ is larger than 0.018. The value is chosen so that the fluctuation is three times larger than the standard deviation when the probability distribution function is exponential.

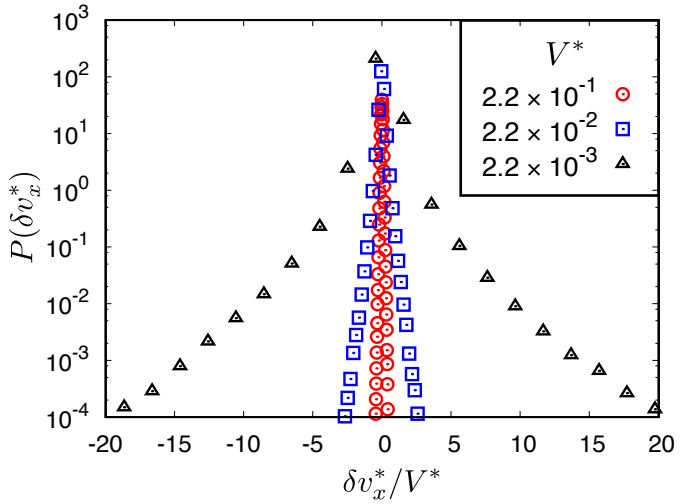


Figure 4.5: Distribution function of the velocity fluctuation $\delta v_x \equiv v_x - \bar{v}_x$ for various velocities of the moving walls $V^*$ with $V^* \equiv V\sqrt{m/\epsilon}$. Here, the average flow $\bar{v}_x$ is subtracted from the particle velocity $v_x$. The horizontal axis thus shows the normalised ratio of the particle velocity to the velocity of the moving walls. I use the following parameters: $u = 2 \times 10^{-2}$, $P^* = 10^{-2}$, and $V^* = 2.2 \times 10^{-1}$ (circles), $2.2 \times 10^{-2}$ (squares), $2.2 \times 10^{-3}$ (triangles). I classify $V^* = 2.2 \times 10^{-1}$ and $2.2 \times 10^{-2}$ as a uniform phase (i) and $2.2 \times 10^{-3}$ as an oscillation phase (ii). This figure is reproduced from Ref. [111].

Next, I will describe the other phases. I could not apply a uniform shear deformation across the whole system with low normal stress and high cohesive force, even in the long-time average as instabilities in the shear field developed. In this case, I observe two characteristic phases: (iii) clustering and (iv) shear-banding. I show the density and velocity profiles of these phases with typical snapshots in Fig. 4.6. In phase (iii), certain clusters form in the bulk region, and they roll with time (see Fig. 4.6(a)). Uniform shear cannot be achieved when these clusters form, as shown in Fig. 4.6(b). In this region, I also observe a reduction in the packing fraction because voids remain near the clusters. In phase (iv), in contrast, the packing fraction profile indicates nearly uniform distribution, while the shear is localised in a certain region, as shown in Fig. 4.6(d). This localisation occurs not only in the bulk region but also in the region near the walls, depending on the parameters and random fluctuations in the initial conditions.

Based on the above discussion, I present phase diagrams of the observed long-time phases

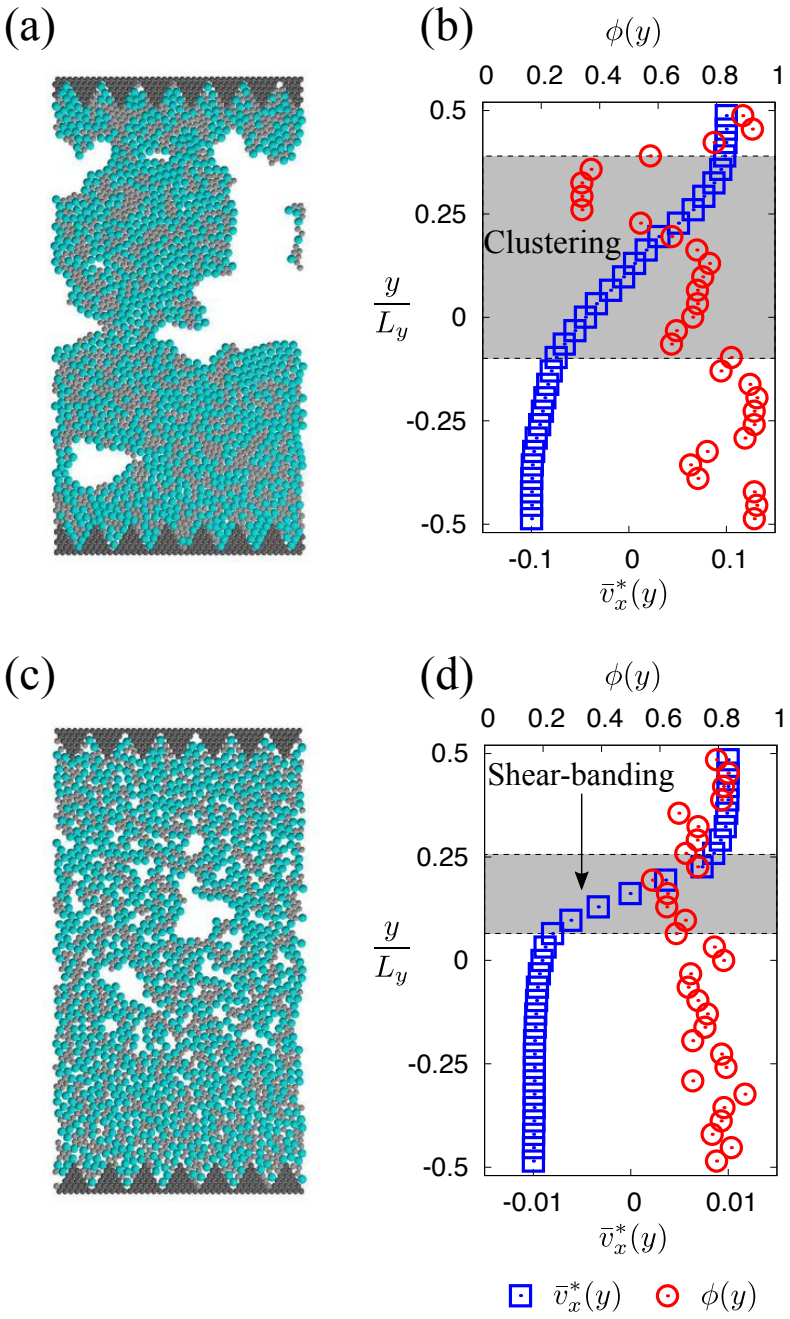


Figure 4.6: (a) Snapshot and (b) density (red circles with upper axis) and velocity (blue squares with lower axis) profiles of the clustering phase ($u = 2 \times 10^{-1}, P^* = 10^{-3}$, and $V^* = 10^{-1}$). Similar plots are shown in (c) and (d) for the shear-banding phase, where I use the parameters $u = 2 \times 10^{-2}, P^* = 10^{-3}$, and $V^* = 10^{-2}$. The shaded regions in (b) and (d) exhibit clustering and shear-banding, respectively. This figure is reproduced from Ref. [111].

in Fig. 4.7 by changing the confining pressure $P$, cohesive force $u$, and shear velocity $V^*$. The uniform shear phase becomes dominant with increasing the shear velocity. On the other hand, the

oscillation phase appears when the shear velocity gets slower. The oscillation phase appears with a strong cohesive force, even in the higher velocity regime, indicating that the attractive force controls and stabilises the oscillation phase. The clustering and shear-banding phases emerge only in the region where the inter-particle attraction is dominant compared with the repulsion.

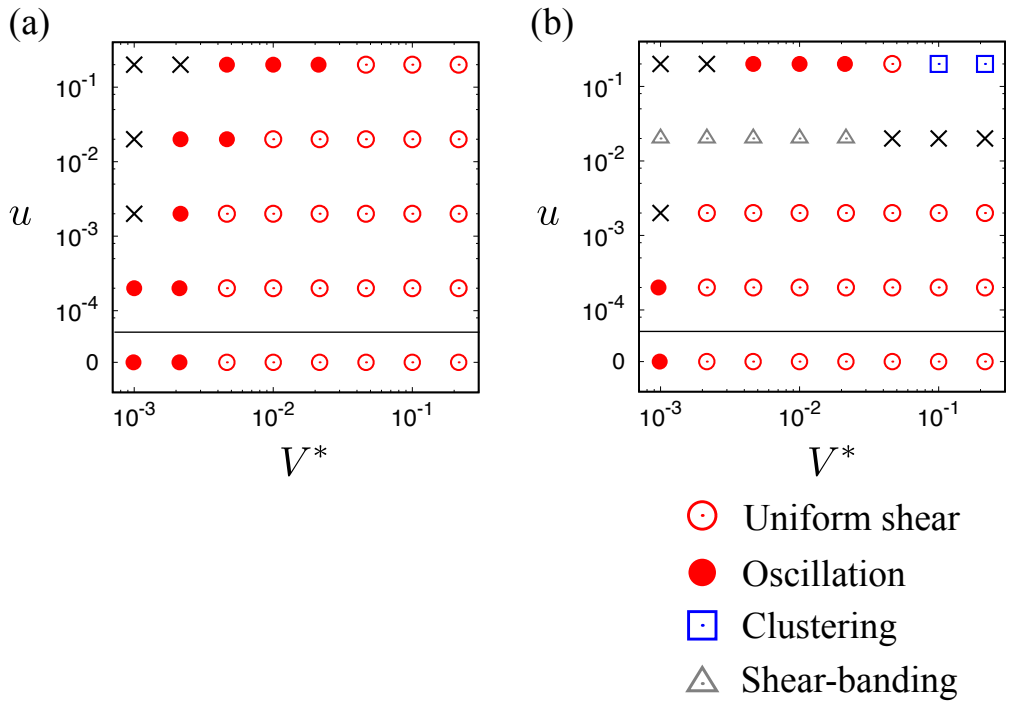


Figure 4.7: Phase diagrams for (a) $P^* = 10^{-2}$ and (b) $10^{-3}$. I distinguish four phases: (i) uniform shear (open circles), (ii) oscillation (filled circles), (iii) clustering (open squares), and (iv) shear-banding (open triangles), where the dimensionless normal stress is $P^* \equiv Pd^2/\epsilon$ and the dimensionless velocity of the moving walls is $V^* \equiv V\sqrt{m/\epsilon}$. The cross marks correspond to the other phases where simulations were unstable, for example where walls are slipping. This figure is reproduced from Ref. [111].

### 4.1.4 Flow curve

Next, I present the $\mu - I$ rheology to describe a granular flow. Here, $\mu(\equiv -\sigma_{xy}/P)$ is the friction coefficient and $I$ is the inertial number defined by $I \equiv \dot{\gamma}\sqrt{m/(Pd)}$. Since both $\mu$ and $I$ are dimensionless parameters, $\mu - I$ rheology is widely used, and it makes a comparison of simulation results with experiments easy [42]. Ideally, the shear-rate should be $\dot{\sigma} = V/L_x$, since I perform shear simulations at constant shear-rates. However, in practice, $\dot{\sigma} < V/L_x$ has sometimes been observed in my simulations due to small slip delays at walls. Thus, I determine the shear-rate $\dot{\gamma}$ as the slope of the velocity profile in the region where the velocity profile is linear

in the long-time average. Hence, I focus only on (i) uniform shear and (ii) oscillation phases. The shear stress $\sigma_{xy}$ is the $xy$ component of the microscopic pressure tensor averaged over the entire system and defined by

$$\sigma_{\alpha\beta} = \frac{1}{L_x L_y} \sum_{i=1}^{N} \left( m_i V_{i,\alpha} V_{i,\beta} + \frac{1}{2} \sum_{j \neq i} r_{ij,\alpha} F_{ij,\beta} \right), \tag{4.6}$$

where $\boldsymbol{V}_i \equiv \boldsymbol{v}_i - \boldsymbol{U}(y)$ is the deviation from the macroscopic velocity field $\boldsymbol{U}(y)$ at each moment in time.

Fig. 4.8 shows the $\mu - I$ rheology for cases with (a) higher normal stress ($P^* = 10^{-2}$) and (b) lower normal stress ($P^* = 10^{-3}$) by varying the strength of the cohesive force $u$. There exist yield stresses in the low shear-rate limit corresponding to the finite values of $\mu$ seen at very slow shear-rates, i.e. low values of $I$. The curves collapse in the high shear-rate regime, which is independent of the attractive potential $u$, except for the most cohesive samples with $u = 2 \times 10^{-1}$. This collapse indicates that attraction may be negligible in the high shear-rate regime, as is expected. On the other hand, in the low shear-rate regime, the effect of attraction is considerable, i.e., the friction coefficient increases as the attraction becomes strong.

In contrast, the flow curve for the strongest attractive potential studied ($u = 2 \times 10^{-1}$) is completely different from those for the weaker attractions. The friction coefficient is abnormally large, as shown in Figs.4.8(a, b), and this trend is particularly notable for the low normal stress cases, where the attraction is dominant. The high friction arises because an attractive force supports the system even without any compressive force applied across the walls of the system. The lower normal stress further increases the friction coefficient. I will discuss this large friction coefficient from different points of view in Sec. 4.1.6.

To investigate the effect of cohesive interaction on the flow curve, I first decompose the friction coefficient into the static part $\mu_c$, defined by the zero $I$ limit friction in Fig. 4.8, and the dynamic part. Then, I fit the flow curves using

$$\mu = \mu_c + a\sqrt{I}, \tag{4.7}$$

with the fitting parameters $a$ and $\mu_c$. I plot $\mu - \mu_c$ against the inertial number $I$ for various $P$ and $u$ in Fig. 4.9. The result coincides with earlier studies [42–44, 211–213], which reported this relationship using frictionless particles without cohesive interactions under a constant pressure condition. This implies that the cohesiveness does not affect the exponent of $I$ in Eq. (4.7) and only affects the static friction $\mu_c$ and the coefficient $a$.

Furthermore, I show the static part of the friction coefficient, $\mu_c$, for various $P^*$ and $u$ in Fig. 4.10. The figure demonstrates that $\mu_c$ is a decreasing function of the normal stress. In addition, $\mu_c$ tends to be independent of the pressure when the cohesion becomes weak. Then,

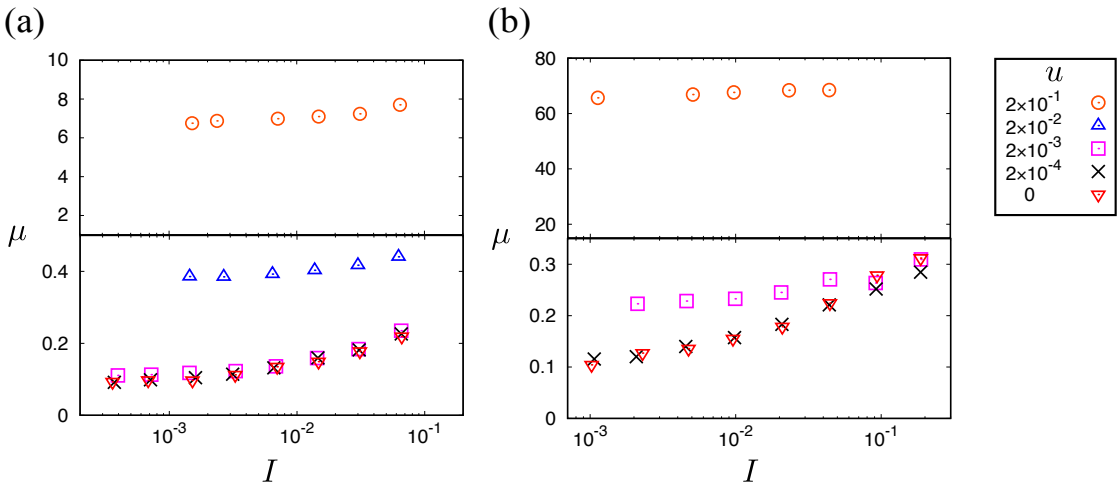


Figure 4.8: Plot of the $\mu - I$ rheology for $u = 2 \times 10^{-1}$ (circles), $2 \times 10^{-2}$ (triangles), $2 \times 10^{-3}$ (squares), $2 \times 10^{-4}$ (cross marks), and 0 (reverse triangles) when the normal stress is (a) higher ($P^* = 10^{-2}$) and (b) lower ($P^* = 10^{-3}$). This figure is reproduced from Ref. [111].

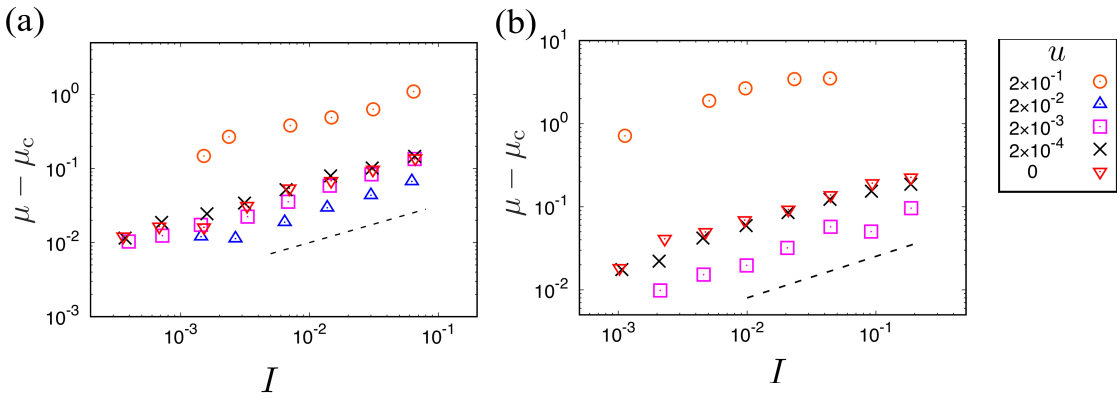


Figure 4.9: Plot of the $\mu - \mu_c$ data for various $u$ when the normal stress is (a) higher ($P^* = 10^{-2}$) and (b) lower ($P^* = 10^{-3}$). $\mu_c$ is the plateau value in the low shear-rate limit in Fig. 4.8. The dashed lines represent Eq. (4.7), i.e. a power law relationship with exponent 1/2. This figure is reproduced from Ref. [111].

I can conclude that the cohesive force influences the relationship between the static friction coefficient and the normal pressure.

I also plot the system-averaged normal stress $\sigma_{xx}$ in the $x$-direction as a function of the inertial number $I$ in Fig. 4.11. At a weak cohesion, the normal stress in the $x$-direction is equivalent to the normal stress, $P^* = 10^{-2}$. In contrast, it becomes lower than the normal stress and tends to be negative for the cohesion-dominant case, $u = 2 \times 10^{-1}$. In this regime, it should be noted that $\sigma_{yy}$ has large fluctuations around the average values of $P^*$, but $\sigma_{yy}$ does not take a negative value. This negative stress in $\sigma_{xx}$ suggests the existence of anisotropy when the attraction is

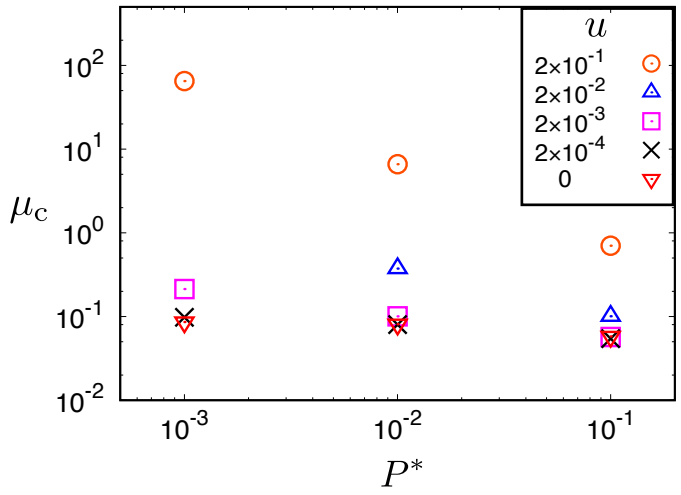


Figure 4.10: Plateau value $\mu_c$ in the flow curve (Fig. 4.8) as a function of the normal pressure $P^*$ for various $u$. This figure is reproduced from Ref. [111].

dominant, which is consistent with the appearance of inhomogeneous phases at high cohesiveness. I will discuss anisotropy further in Sec. 4.1.6.

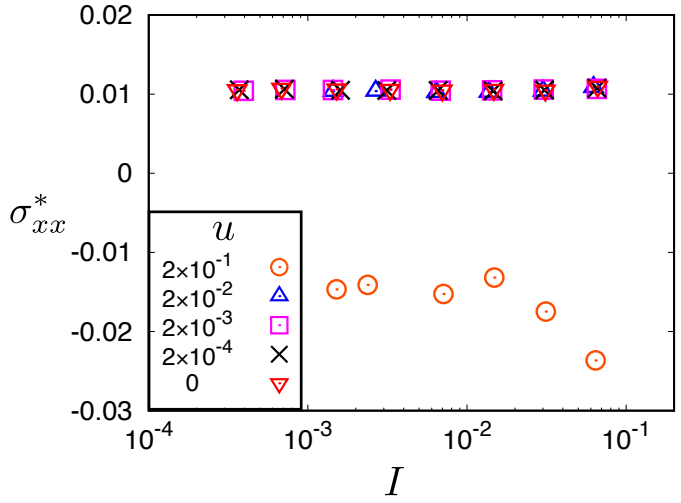


Figure 4.11: Normal stress $\sigma^*_{xx}(\equiv \sigma_{xx}d^2/\epsilon)$ in the $x$-direction versus the inertial number $I$ for various $u$ when $P^* = 10^{-2}$. This figure is reproduced from Ref. [111].

### 4.1.5 Packing fraction

Under a constant pressure condition, the packing fraction is not controlled and is determined by the set of control parameters. I plot the inertial number dependence of the packing fraction in Fig. 4.12. The packing fraction is nearly independent of the inertial number but depends on the cohesiveness and the pressure. When the cohesion is weak, the packing fraction is nearly equal to

the jamming density, as shown with the dashed line in Fig. 4.12. At high $I$, curves deviate from the jamming density because particle collision becomes dominant at this regime [42]. On the other hand, an artificially high packing fraction of $\phi > 0.90$ is realised for $u = 2 \times 10^{-1}$. At such a high cohesion, particles can deform significantly and can be packed above the jamming density. It should be noted that high pressure also has a contribution to making the system denser. The parameters for this high packing fraction are the same as those for the abnormally large friction coefficient discussed in Sec. 4.1.4. In particular, a large friction coefficient is achieved in the case of low pressure and strong attraction.

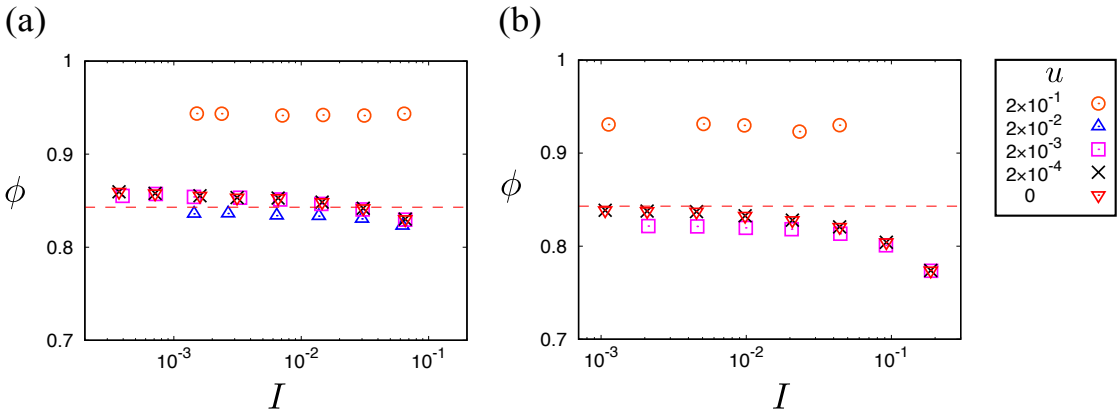


Figure 4.12: Packing fraction for various $u$ when the normal stress is (a) higher ($P^* = 10^{-2}$) and (b) lower ($P^* = 10^{-3}$). The dashed lines indicate the jamming density ($\phi_J = 0.843$) for a hard sphere system in 2D [221]. This figure is reproduced from Ref. [111].

### 4.1.6 Anisotropy

Next, I measure the anisotropies of the coordination number and the inter-particle force. Since I apply both uniaxial compression and shear deformation into the system, particles have directionality in repulsive and attractive forces [213]. When I consider the four quadrants around a certain particle, repulsive forces develop in the second and fourth quadrants (as shown by blue regions in Fig. 4.13(a)), and attractive forces in the first and third quadrants (as shown by red regions in Fig. 4.13(a)) under the current external forces. Thus, I define the anisotropic coordination number $Z_{\max}$ by the coordination number in the second and fourth quadrants and $Z_{\min}$ by one in the other quadrants. I also decompose the component of the anisotorpic coordination number by the inter-particle distances, for example, $Z^{\rm rep}$ in the repulsive force range or $Z^{\rm att}$ in the attractive force range, based on Eq. (4.1). I present the anisotropic coordination number in Fig. 4.13(b, c). Fig. 4.13(b) describes the case where cohesive force is weak with $u = 2 \times 10^{-4}, P^* = 10^{-3}$. There is no significant change between $Z^{\rm rep}_{\max}$ and $Z^{\rm rep}_{\min}$, and the coordination number in the at-

traction range is negligible. Thus, I cannot observe the anisotropic effects. On the other hand, in the cohesion-dominant case of Fig. 4.13(c), $Z^{\rm rep}_{\rm max} > Z^{\rm rep}_{\rm min}$ and $Z^{\rm att}_{\rm min} > Z^{\rm att}_{\rm max}$ clearly imply the anisotropic properties. These results are intuitive because a high $Z^{\rm rep}_{\rm max}$ represents repulsion dominance along the maximum compressional axis ($Z_{\rm max}$) and a high value of $Z^{\rm att}_{\rm min}$ represents attraction dominance along the minimum compressional axis ($Z_{\rm min}$).

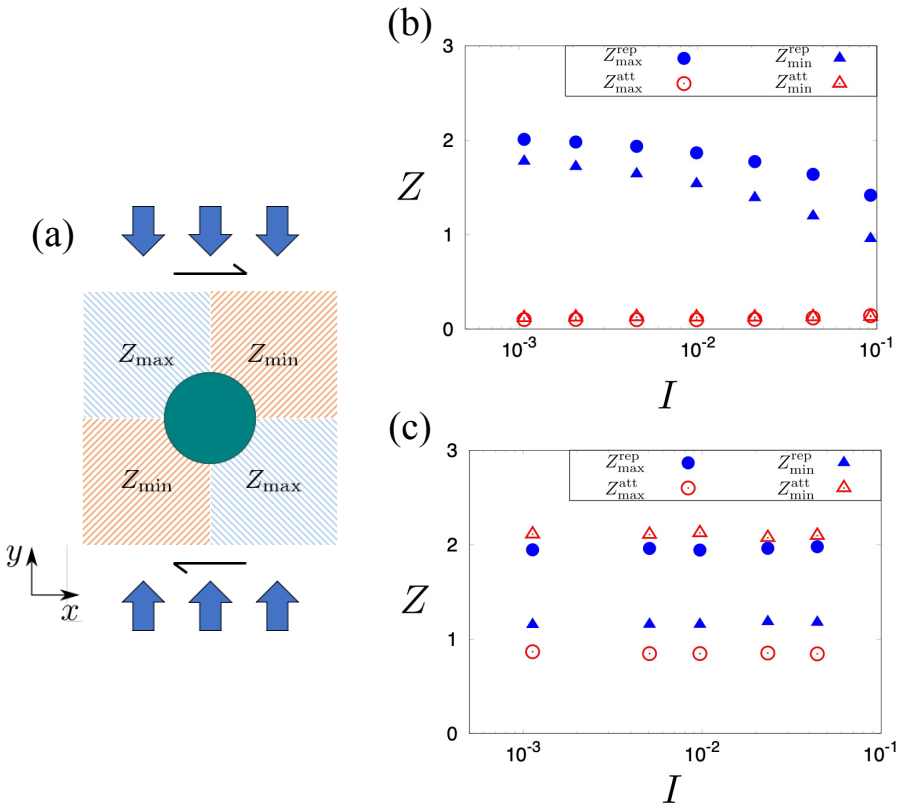


Figure 4.13: (a) Schematic diagram of the decomposition of the coordination number by principal axes: $Z_{\rm max}$ and $Z_{\rm min}$. They are further decomposed into two sub-elements depending on inter-particle distances: attractive (superscript of "att") and repulsive ranges (superscript of "rep"). I plotted the anisotropic coordination number by changing the inertial number for the (b) repulsion dominant case ($u = 2 \times 10^{-4}$ and $P^* = 10^{-3}$) and (c) attraction dominant case ($u = 2 \times 10^{-1}$ and $P^* = 10^{-3}$). The filled and the open circles (or triangles) represent the two elements of $Z_{\rm max}$ (or $Z_{\rm min}$), respectively. This figure is adapted from Ref. [111].

In addition, I plot the angular distribution of the contact forces in Fig. 4.14. Here, I take a time average over $10,000t^*$ and a configurational average over all particles except for boundary particles. For visibility, I plot the magnitudes of attractive and repulsive forces. In Fig. 4.14(a) of the weak cohesion case, the maximum compressional axis ($\sigma_1$) corresponds to the repulsion-dominant region. On the other hand, for the cohesion-dominant case in Fig. 4.14(b), the at-

tractive force becomes maximum along the minimum compressional axis ($\sigma_2$). These results are consistent with the anisotropic coordination number shown in Fig. 4.13.

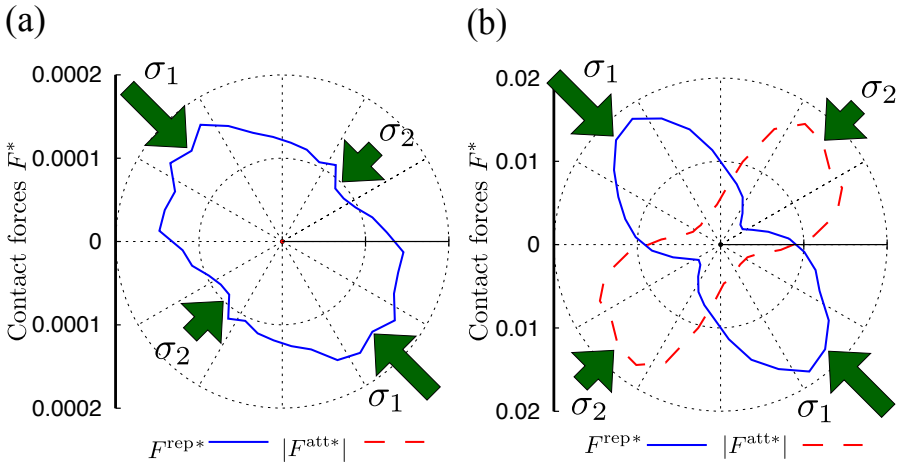


Figure 4.14: Angular distribution of the contact forces for the (a) weak cohesion case with $u = 2 \times 10^{-4}, P^* = 10^{-3}, V^* = 2.2 \times 10^{-3}$ and (b) strong cohesion case with $u = 2 \times 10^{-1}, P^* = 10^{-3}, V^* = 2.2 \times 10^{-2}$. I plot the magnitude of the attractive (dashed line) and repulsive (solid line) forces. The arrows indicate the maximum and minimum compression axes ($\sigma_1$ and $\sigma_2$), respectively. For case (a), the attractive force is vanishingly small because its contribution is considerably weaker than the repulsive force. This figure is reproduced from Ref. [111].

Furthermore, I discuss the abnormally high friction coefficient when the attractive potential is strong and the normal stress is low as shown in Fig. 4.8(b), in terms of anisotropy of the inter-particle force. Note that the normal stress in the $x$-direction $\sigma_{xx}$ takes negative values in this regime (see Fig. 4.11). As discussed above, repulsive forces tend to develop in the second and fourth quadrants, and attractive forces in the first and third quadrants. Thus, I depicted the schematic picture of the forces acting on a fixed particle in Fig. 4.15. The nearby particle in the first quadrant is in the attractive range, and one in the fourth quadrant has a repulsive interaction with the fixed particle. I decompose the repulsive force ($\boldsymbol{F}^{\mathrm{rep}}$) and attractive force ($\boldsymbol{F}^{\mathrm{att}}$) into $x$ and $y$ components, respectively. Here, $\boldsymbol{F}_x^{\mathrm{rep}}$ and $\boldsymbol{F}_x^{\mathrm{att}}$ have opposite signs, causing a decrease in $\sigma_{xx}$ compared with the purely repulsive system, as shown in Fig. 4.11. On the other hand, $\boldsymbol{F}_y^{\mathrm{rep}}$ and $\boldsymbol{F}_y^{\mathrm{att}}$ have the same sign and contribute to increase $\sigma_{xy}$, as per the second term in Eq. (4.6). This can be the origin of the abnormally large friction coefficient.

### 4.1.7 Summary

I performed MD simulations of cohesive granular particles under a constant pressure condition and sheared the system by moving the boundary walls. I considered the effect of cohesion on

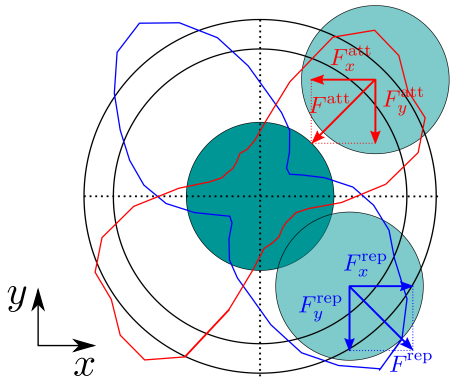


Figure 4.15: Schematic of the decomposition of the repulsive and attractive forces in Fig. 4.14(b). This figure is reproduced from Ref. [111].

rheology by adopting an attractive potential.

First, I established four distinct phases depending on the constant wall pressure, the shear velocity of the moving walls, and the attractive potential between particles. In the region where uniform shear was seen in the long-time average, I classified the uniform shear phase and the oscillation phase by investigating the distribution function quantitatively. In addition, when the cohesive force was strong, it was difficult to obtain uniform shear in the bulk, even after I took a long-time average. In such cases, I observed the clustering and shear-banding phases with localised shear deformations in certain regions. In the clustering phase, a strong cohesion causes a cluster formation. In the shear-banding phase, shear is localised within a narrow region. These phases may be determined to minimise the energy of the system, which I will discuss in Sec. 4.2. By performing parameter studies, I generated the phase diagram.

Based on this phase diagram, I plotted the flow curve ($\mu - I$ rheology) in the region where uniform shear was applied in the long-time average. The flow curves are a monotonically increasing function of the inertial number. By subtracting the plateau value $\mu_{\mathrm{c}}$ from the $\mu - I$ rheology, I analysed the exponent of $\mu - \mu_{\mathrm{c}}$ as a function of $I$. This exponent, which is $1/2$ when the curve is properly fit, is known in noncohesive systems [43]. Thus, I conclude that the effect of cohesion can be represented by $\mu_{\mathrm{c}}$.

In the flow curves, strong cohesion yields a large friction coefficient. In this region, anisotropies of the coordination number and angular distribution of the inter-particle forces appear. These demonstrate that the repulsive forces are maximum along the maximum compressional axis, whereas the attractive forces are maximum along the minimum compressional axis, which can be the origin of the large friction coefficient.

Finally, I compare these results with previous works [45,46]. I prepared finite walls and moved these walls to apply a shear to the system under a constant pressure condition. However, previous

studies involved a constant volume condition with the Lees–Edwards boundary condition [91]. They demonstrated that the flow curve was non-monotonic below the jamming density, whereas it monotonically increased with the shear-rate above the jamming density. Under a constant pressure condition, I obtained a monotonically increasing flow curve irrespective of the density. This difference may be due to the stability of the voids. In previous studies [45, 46], these voids may survive under a certain condition below the jamming density, which was also reported in Ref. [53]. In contrast, voids tend to vanish in our system because the normal stress in the $y$-direction may generally inhibit the spatial heterogeneity of the density. Although I report the rhology curves only where uniform shear is applied in long-time average, I speculate that the non-monotonic rheology observed in the previous studies relate to the clustering and shear-banding phases. In the next section, I will explore the stability of the voids with an enhanced model in 3D.

## 4.2 Rheology of cohesive granular particles under constant pressure in 3D

### 4.2.1 Introduction

In Sec. 4.1, I performed shear simulations of cohesive granular particles under constant loading conditions. The effect of cohesive force on the rheology is small under a weak cohesion, or the condition of relatively strong cohesion but also strong loading. The rheology curve can be well approximated by $\mu = \mu_c + a\sqrt{I}$, which agrees with the rheology of sheared granulates under the constant pressure condition but without cohesive interactions [43]. Furthermore, simulation results suggested that the cohesion effect can be integrated into the static friction $\mu_c$, defined as the friction coefficient at the zero shear-rate limit, as shown in Fig. 4.9. On the other hand, in the region where the effect of cohesive force becomes dominant, I observed a cluster formation and a shear-banding due to strong cohesion, causing localised shear deformations.

However, there is room for improvement in the simulation model described in Sec. 4.1 and published in Ref. [111]. For example, I implemented the simulation in a 2D system, using a simplified linear spring for the particle interactions. In this section, I will refine the simulation model. I will implement shear simulations under a constant loading in 3D, using the Hertzian contact theory with weak cohesion, to describe the inter-particle interaction in this model. I will check if the non-uniform rheology (clustering or shear-banding) due to the cohesion observed in the 2D system is retained in the more sophisticated simulation setup. In order to reveal the formation process of clustering, I will also investigate the effect of a stepwise change in shear-rate

near the clustering phase transition. Finally, I will report the preliminary results of examining the critical nuclei size for cluster formation.

### 4.2.2 The model

As in Sec. 4.1, but now using 3D spheres as particles, I prepare corrugated walls consisting of particles at the top and bottom of the system and apply a shear deformation across the system by moving the walls with a velocity of $V$ while pushing them with a confining pressure of $P$. For the boundary condition, I impose periodic boundary conditions in the $x$ and $y$ directions. I set the system size as $L_x = 42d$, and consider the three cases where $L_y = 2d, 4d$, and $6d$. It should be noted that the system thickness is quite thin, but I can sufficiently take into account 3-dimensionality to see differences between 2D and 3D. As an example, I show a snapshot of the 3D system in Fig. 4.16. The height $L_z$ was freely determined by the number of particles and internal variables, such as the strength of cohesion $u$, confining pressure $P$, and shear velocity $V$. I adjust the number of particles so that the aspect ratio of the system with $L_y = 2d$ is roughly the same as in the 2D system simulations of Sec. 4.1 ($L_x : L_z \simeq 1 : 2$), and so I typically use $15,000$ particles. However, when studying the hysteresis effect, which requires a long-time simulation, I use $6,000$ particles to reduce the computation time.

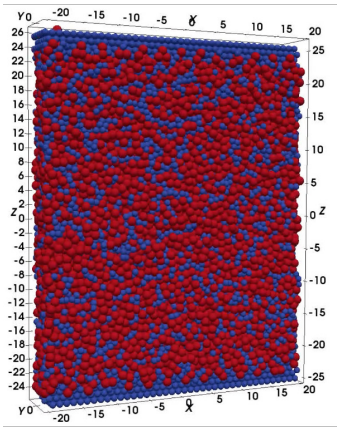

Figure 4.16: Simulation model for the shear simulation in 3D. I confine bidisperse spheres in a $50:50$ ratio with diameters $d$ and $1.4d$ between the top and bottom boundary walls by applying a confining pressure. In this plot, I set the system size as the system width $L_x = 42d$ and the system thickness $L_y = 6d$ with the number of particles $15,000$.

I implemented the inter-particle interaction by the following equation:

$$F^h(r_{ij}) = \begin{cases} \frac{2\epsilon}{d_{ij}} \left\{ (1 - \frac{r_{ij}}{d_{ij}})^{3/2} - u \right\} & (\frac{r_{ij}}{d_{ij}} \leq 1), \\ \frac{2\epsilon}{d_{ij}} \left\{ \frac{r_{ij}}{d_{ij}} - (1+u) \right\} & (1 < \frac{r_{ij}}{d_{ij}} \leq 1+u), \\ 0 & (\frac{r_{ij}}{d_{ij}} > 1+u). \end{cases} \tag{4.8}$$

This interaction is based on the elastic force of the Hertz contact when the neighbouring particles have an overlap, and also takes into account the cohesive force acting at a short distance $u$. This inter-particle interaction is analogous to the DMT theory used for micron-sized particles [81, 82]. In Fig. 4.17, I show a comparison of the interaction in Eq. (4.8) with the model of a linear spring and weak cohesive interaction introduced in Sec. 4.1. Although the depth of the attraction is the same in both models, there are slight differences in the attraction range and the elastic force when the particles are in contact.

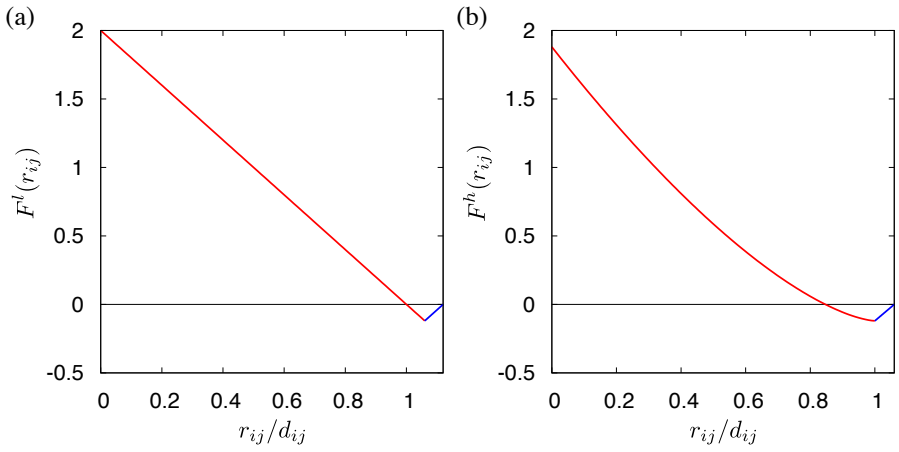


Figure 4.17: (a) Inter-particle interaction used in Sec. 4.1, assuming a linear spring with a weak attractive force acting over short distances [45, 46]. (b) Particle interaction used here, assuming a Hertzian contact with a weak attractive force acting over a short distance, defined by Eq. (4.8). I use the following parameters: $\epsilon = 1.0$, $d_{ij} = 1.0$, and $u = 0.06$. This parameter set is typical for the 3D shear simulations in this study.

In this study, I use the following physical parameters. I take the interaction strength $\epsilon$ in Eq. (4.8), the smaller particle diameter $d$, and the particle mass $m$ to have unit values, and all physical quantities were made dimensionless using these quantities. As in Sec. 4.1, I denote the non-dimensionalised physical quantities with an asterisk. In order to reproduce the cluster and shear-banding phases observed in the simulations of the 2D system, where uniform shear could not be applied at the steady states, I use the normal stress, $P^* = 10^{-3}$, and varied the strength of cohesion from $u = 2 \times 10^{-2}$ to $8 \times 10^{-2}$. I also varied the non-dimensionalised shear-rate from $V^* = 10^{-3}$ to $10^{-4/3}$.

For making the initial conditions, I introduce a weak cohesive force of $u = 2 \times 10^{-2}$ to prepare a system configuration with sufficiently stable energy. Without applying a shear deformation ($V^* = 0$), I then compress the system by the non-dimensionalised confining stress, $P^* = 10^{-3}$. I run this simulation for a long time ($t^* = 50,000$), and after confirming that the system energy is sufficiently stable, I select the resulting particle configuration as the initial setup.

### 4.2.3 Phase diagram

By changing the strength of cohesion $u$, the non-dimensionalised shear-rate $V^*$, and the system thickness $L_y$, I classify the phases at the steady-state, as shown in Fig. 4.18. Before evaluating their phases, I run these simulations for time intervals of at least $100,000$ and check that the system's energy reaches a steady-state. Three different realisations with randomised initial conditions were studied for each parameter set. I make a phase diagram in Fig. 4.18 for one representative realisation, and the other two realisations show similar trends except for minor differences in the boundaries between different phases. Slippage near the boundary walls is often observed at a higher shear-rate and weaker cohesion (shaded in blue in the figure). At lower shear-rate and stronger cohesion (shaded in grey in the figure), uniform shear tends to be applied across the whole system. Between these regions, I observed cluster formation. However, parameter sets with which clustering can be observed are limited compared to the 2D system. The clustering parameter range becomes narrower by increasing the system thickness $L_y$, which strengthens the three-dimensionality. Furthermore, I do not observe shear-banding occurring inside the bulk system, rather it tends to develop only near the boundaries. I show typical snapshots of the different phases in Fig. 4.19. Both Fig. 4.19(a,b) show configurations that correspond to the clustering phase. Depending the position of clusters, either inside the bulk (Fig. 4.19(a)) or near the boundary wall (Fig. 4.19(b)), I further classify the clustering phases. In the phase of slipping near the boundary (Fig. 4.19(c)), I observe that either the upper or lower wall slips, and bulk particles are slipping with sticking together with another wall. I prepare the initial configuration carefully to avoid such a slippage near boundary walls, but nevertheless, slippage is observed even in the slow shear regime as the system thickness increases. In Fig. 4.19(a,b,c), voids stably exist near clusters or the boundary wall, which make these phases differ from the uniform shear phase.

### 4.2.4 Hysteresis

I have investigated the simulation results at steady states in Sec. 4.2.3. Next, I will address the hysteresis effect when I vary the shear-rate, stepwise. Throughout this numerical experiment, I

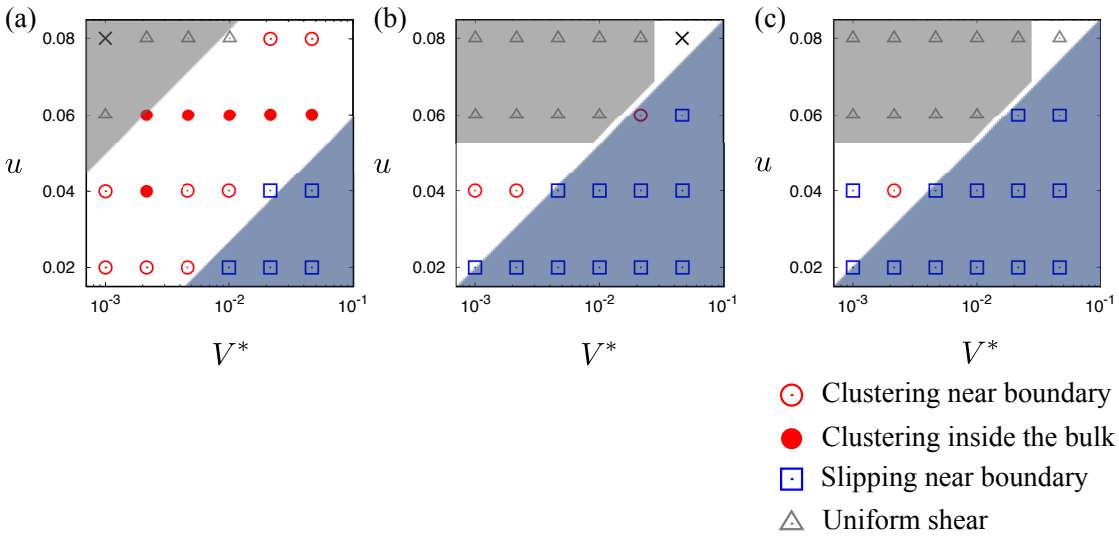


Figure 4.18: Phase diagrams obtained at steady states during long-time shearing simulations in 3D. I perform simulations with system thicknesses of (a) $L_y = 2d$, (b) $L_y = 4d$, and $L_y = 6d$. In the region where $u$ is large and $V^*$ is small (shaded in grey), uniform shear is observed across the whole system. In contrast, in the region where $u$ is small and $V^*$ is large (shaded in blue), the system slips near the boundary wall in the steady-state, regardless of the preparation of the initial conditions. Cluster formation can occur between these two limits. Since I fix the number of particles as $15,000$ in these simulations, the system height, $L_z$, changes depending on the other parameters.

aim to answer three questions. Firstly, after cluster formation, can the cluster, or voids as co-products, survive as stable features? Secondly, what physical parameter changes can be observed before and after cluster formation? Thirdly, how does the cluster form and how is this related to void generation?

For this test, I vary shear-rates stepwise while fixing all other parameters. Initially, I increase the shear-rate step by step (process (i) in Fig. 4.20(a)). After the shear-rate attains its maximum value of $V^* = 10^{-4/3}$, I decrease the shear-rate step by step (process (ii) in Fig. 4.20(a)). At each shear-rate, I run simulations for a time interval of $20,000$ dimensionless units. The time evolution of a typical system with the height, $L_z/d$, and shear velocity, $V^*$, is depicted in Fig. 4.20(b). The system height fluctuates after $t^* = 60,000$, corresponding to clustering formation. After a cluster is generated, even when I reduce the shear velocity, the cluster can survive, as indicated by the ongoing fluctuation of the system height after this time. Therefore, it was confirmed that once clusters are created, they can exist stably even in regions where no clusters are observed at a steady state and that there is a hysteresis effect. This answers the first question raised in the beginning of this section. It should be noted that, in the phase diagram at steady-states

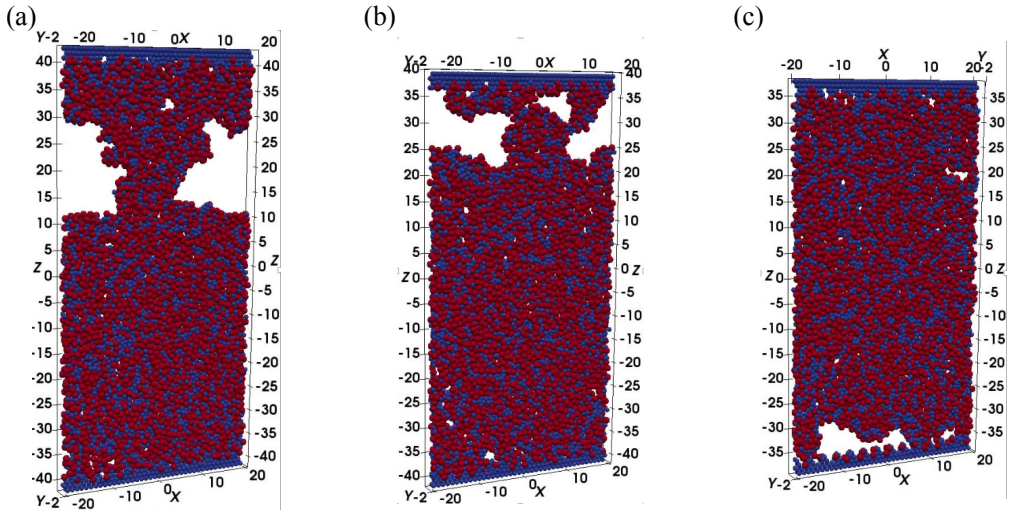


Figure 4.19: Typical snapshots of identified phases in the phase diagram: (a) Clustering inside the bulk, (b) clustering near the boundary, and (c) slipping near the boundary. I use the following parameter sets: $L_y = 2d$, $u = 0.04$, along with (a) $V^* = 10^{-8/3}$, (b) $V^* = 10^{-7/3}$, and (c) $V^* = 10^{-5/3}$, respectively.

in Fig. 4.20(a), the shear-rates $V^* = 10^{-8/3}$ and $V^* = 10^{-7/3}$ are classified as the clustering phases inside the bulk, but I could not observe the system fluctuation until $t^* = 60,000$. This can be because the simulation for hysteresis has the time interval of $20,000$ at each shear rate, which is shorter than the time duration required to achieve a steady-state, so the system may be undergoing a stochastic transition between the uniform shear phase and the clustering phase.

Cluster formation can also be detected through the time evolution of the non-dimensionalised shear stress, $\sigma^*_{xz}$, measured in the whole system, as shown in Fig. 4.20(c). A shear stress reduction is accompanied by a cluster formation around $t^* = 60,000$. I speculate that this is because a rotation of the formed cluster acts as a lubricant for the shear deformation. However, the details are not clear and further analysis and discussion are required. Time series of other quantities related to the system energy are shown in Fig. 4.21. It is noted that these quantities are normalised by the number of particles $(6,000)$ to show the energy per particle. Fig. 4.21(a) shows that the potential energy of bulk particles continuously decreases until a cluster formation. After the cluster formed, any further change in potential energy is slight, apart from the continuous fluctuations around an average value. This suggests that cluster formation is energetically advantageous in terms of potential energy. In Fig. 4.21(b), the kinetic energy per particle is approximated by the square of shear-rates ($V^{*2}$, see Fig. 4.20(b)), and any change in the absolute value of the kinetic energy is tiny, even when a cluster is formed around $t^* = 60,000$. There is also no clear hysteresis in the kinetic term. In contrast, the potential energy of the walls in

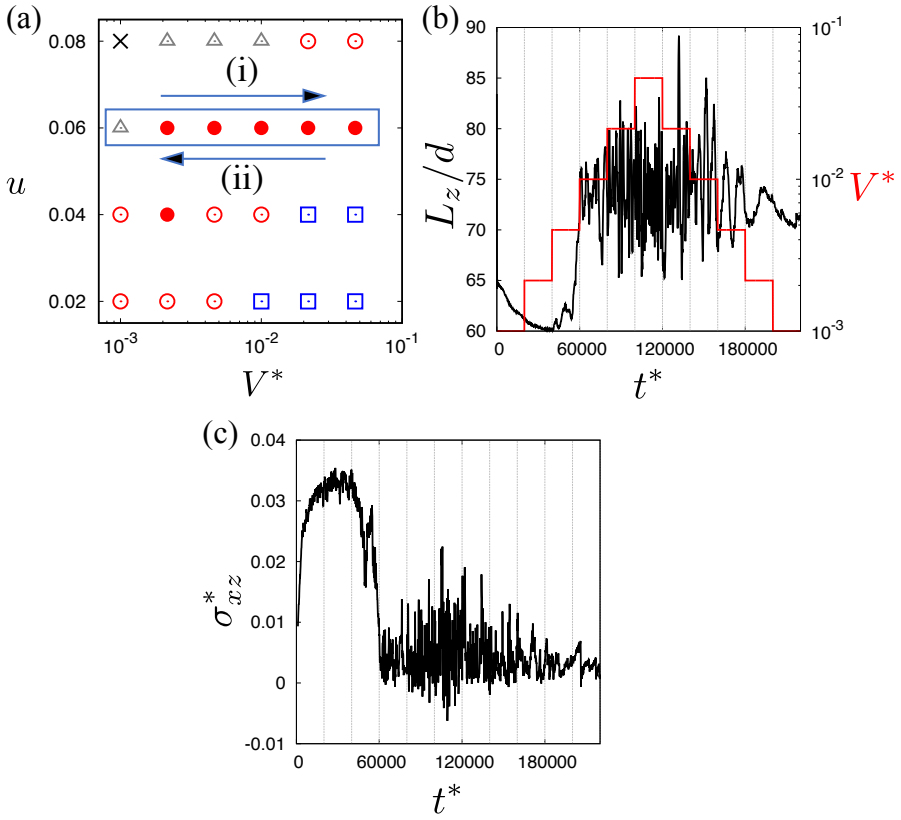


Figure 4.20: Investigation of the hysteresis effect when the shear-rate is varied stepwise. (a) Example of variation of shear-rates while fixing the cohesion strength at $u = 0.06$. I evolve the system for $20,000$ time units at each shear-rate while (i) I increase the shear-rate stepwise. Then, after reaching $V^* = 10^{-4/3}$, (ii) I decrease the shear-rate step by step in a similar way. The phase diagram shown here corresponds to $L_y = 2d$, as in Fig. 4.19(a). (b) Time series of the system height, $L_z/d$, coloured in black (left axis) and the stepwise change in shear-rate, $V^*$, visualised in red (right axis). (c) Time series of the non-dimensionalised shear-rate, $\sigma^*_{xz} (= \sigma_{xz} d^3/\epsilon)$. I use the following parameter set: $u = 0.06$, $L_y = 2d$.

Fig. 4.21(c), defined by $P \times$ (distance of moved walls), shows a similar trend to the one in system height (see Fig. 4.20(b)) to which it is clearly related. I also show a time evolution of the total energy calculated by a summation of the potential energy, kinetic energy, and the energy to move the walls, in Fig. 4.21(d). Summarising the above and answering the second question, a cluster formation can be detected by observing the time evolution of the following physical quantities: system height, shear stress, potential energy of the bulk particles, and potential energy of the boundary walls. It should be noted, however, that the detection of a cluster formation is possible only after the cluster formed and a process of the cluster forming, relating to the third question, is unclear. Therefore, further observation would be needed to capture the precursor signs of

cluster formation.

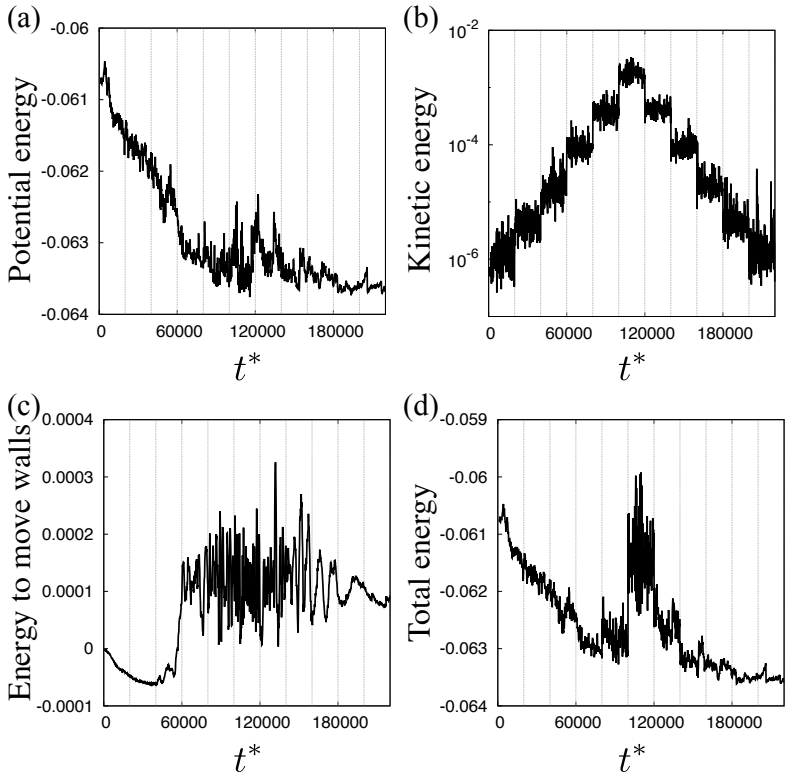


Figure 4.21: Time series of (a) potential energy, (b) kinetic energy, (c) potential energy of walls, and (d) total energy of the system when investigating the hysteresis effect. I use the following parameter set: $u = 0.06$, $L_y = 2d$.

### 4.2.5 Critical nuclei size

To further investigate the process of cluster formation, I will focus now on void growth accompanied by clustering. Since voids must stably exist surrounding a cluster when a cluster forms, the condition is required where voids can nucleate and then grow, in association with a cluster. Such a nucleation process has similarities to the nucleation of crystals [222] and crack nucleation in solids [223]. Then, there should be a critical nuclei size for a clustering formation, and I will address how to identify this critical size. By utilising the parameter set where uniform shear is observed ($u = 0.06$, $V^* = -7/3$, and $L_y = 6d$), I intentionally generated a cylindrical void with a radius $R_c$ at the centre of the system (see Fig. 4.22(a)) after uniform shear has been applied for some time ($t^* = 10,000$). By following the time evolution of the void, I check whether the void, or defect, can nucleate a stable cluster formation or not.

In Fig. 4.22(b, c, d), I show the time evolution of the non-dimensionalised normal stress, $\sigma^*_{zz}$, shear stress $\sigma^*_{xz}$, and total energy while varying the radius of the void from $R_c/d = 0$ to 6.

The solid lines describe the averaged value in 3 realisations and shaded regions correspond to the standard deviation of each parameter. Although the normal stress was expected to fluctuate after a cluster formation, it is hard to distinguish this clearly as an indicator of a cluster formation, as shown in Fig. 4.22(b). On the other hand, in Fig. 4.22(c), reductions in the shear stress clearly highlight the cluster formation, for example, when $R_c/d = 4, 5$, or 6. The huge fluctuation at $R_c/d = 4$ means that $R_c/d = 4$ is about the critical size for cluster formation, as out of three realisations, clusters are formed two times, and no clusters were formed in the other time. These clustering formations can also be detected by the time evolution of the total energy, as depicted in Fig. 4.22(d). In the parameter sets where a cluster forms, I can observe the significant reduction in the total energy after cluster formation with a void radius above $R_c/d = 4$. These indicators are consistent with what I have seen in Sec. 4.2.4.

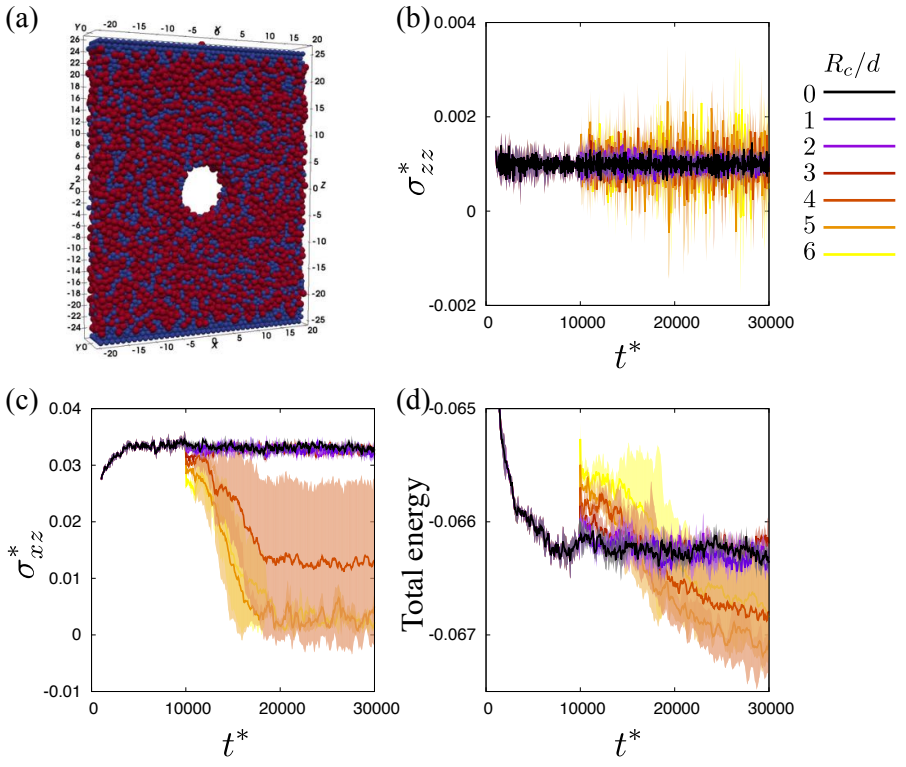


Figure 4.22: Investigation of the nucleation size creating a clustering. I make a void intentionally at the centre of the system to trigger cluster formation. (a) Snapshot of void creation ($t^* = 10,000$ and $R_c/d = 5$). (b) Time evolution of the normal stress, $\sigma_{zz}$, for void sizes, $R_c/d$, in the range of 0 to 6. (c) Time evolution of the shear stress, $\sigma_{xz}$. (d) Time evolution of the total energy inside the system. I use the following parameters set: $u = 0.06$, $V^* = 10^{-2}$ and $L_y = 6d$. I perform three realisations for each parameter, and I show the average value by solid lines and the standard deviation by shaded regions.

Through the above observations, I identify the critical nuclei size as $R_c/d = 4$ for the particular parameter set: $u = 0.06$, $V^* = -7/3$, and $L_y = 6d$. However, the critical nuclei size should strongly depend on the choice of parameters, and further investigation on parameter study would be needed to strengthen these conclusions. Furthermore, to clarify the process of cluster formations, it is required to understand a growing process of the void nucleation developing into clusters. This could be addressed in the future.

### 4.2.6 Summary and discussion

In this study, I could observe the non-uniform shear deformation, which is clustering, even in the 3D system as well as in the 2D system. I have made three notable observations. First, once a cluster forms, the cluster can exist stably even in parameter regimes where I observed that uniform shear could be applied into the system in steady state: this shows a hysteresis effect. Second, before and after the formation of such clusters, I observed significant changes in the time evolution of several physical quantities, for example, the fluctuation in a system height, the shear stress in a whole system, the potential energy of bulk system, and potential energy of boundary walls. Finally, in a particular parameter region, I also identified the existence of a critical nuclei size of a void for cluster formations. However, further study would be needed for revealing a parameter dependence of the critical nuclei size and for understanding the growth process of a void and its associated cluster.

# Chapter 5

# Summary and discussion

This thesis focused on the emergent phenomena of cohesive granular materials, which appear when the system deforms by application of an external force. Here, I addressed two types of deformation processes using discrete element method (DEM) and molecular dynamics (MD) simulations: the uniaxial compression experiments of a cemented granular system were simulated in Chapter 3, while shear deformation of a cohesive granular particle system was considered in Chapter 4. The first system shows the appearance of brittle failure with shear-banding, ductile failure, and compacting failure at increasing particle densities. For the second system, I identified non-uniform rheology, such as shear localisation and clustering with dilatancy, for conditions where the cohesive interaction is dominant. Furthermore, I succeeded in identifying key physical quantities, which changed before and after the emergence of these emergent phenomena.

In Sec. 3.1, as an example of cohesive granular materials, I dealt with an artificial cemented granular system, which was experimentally developed by my collaborators [38, 39]. The system consists of glass beads attached by polymer bridges and shows a wide range of elasticity by tuning the bridge stiffness. The system breaks in a brittle manner under uniaxial compression. To address the microscopic mechanics that cannot be addressed by experiments, I modelled the system by DEM simulations. For the simulations, all the parameters are constrained by the mechanical properties of a bridge between two glass beads, and the simulated geometry is designed to reproduce the experimental geometry as exactly as possible. I also developed criteria for bridge breakage based on the microscopic observations [39]. As a result, I could reproduce the experimental results semi-quantitatively for two different parameter sets by simulations (see Fig. 3.6). I could also reproduce how the system fails in a brittle manner via shear deformation, when the system exceeds the limit of elastic deformation. The model further showed how the elasticity of the sample varied as the bridge stiffness changed, as shown in Fig. 3.7, which is consistent with the experimental results [38]. In addition to simulating the changes in polymer content, I performed further simulations where I changed the bridge geometry, including the bridge diameter, and performed simulations. I obtained a proportional relationship between elasticity and polymer content in the pendular regime (see Fig. 3.8) as observed in the related experiments [38]. These results show that a simple minimal model is capable of accurately

predicting the large-scale mechanics of cohesive granular materials, from an understanding of its microscopic properties.

The constructed model is highly constrained by similar experiments. Although the target of this model is limited to the cohesive granular system, model parameters can be changed easily and the model is highly versatile.

In Sec. 3.2, I explored the failure process of the cemented grain system developed in Sec. 3.1. In particular, I investigated the applicability of the modelled system to different materials by changing the density of the hard particles that constitute the backbone of the model material. The extended system shows three types of failure modes: shear banding, plastic creep and anti-cracks or compaction bands, as depicted in Fig. 3.10. These failure modes can be seen in nature, for example in snow [17, 29, 166], foam [123], colloidal gels [132, 170, 171], powder aggregates [130,146,168,169], sandstone [121,122,142,157–159,163,189] and so on. The characters of these failure modes were explained in terms of the stress-strain relationship and spatial distribution of bridge breakages. For example, I showed the stress-strain curves and the activity of bond breakages in Fig. 3.11. A dense system breaks in a brittle manner with a peak stress, and the system with a medium-density deforms plastically. Further reduction in density induces the compacting failure (creating compaction bands or anti-cracks) accompanied by an intermittent stress drop and bursts of damage activity. These differences between failure modes can also be captured by the statistical properties of the spatial distribution of bridge breakages, which is summarised by the normalised configuration entropy (see Fig. 3.12) and by the shift in the sign of the dilatancy factor (see Fig. 3.14). Furthermore, the failure by compaction was characterised by the detection of local changes in the coordination number and displacements in $z$-direction with increasing strain, as shown in Fig. 3.15. Thus, I conclude that the particle and bond density, along with the spatial distribution of bridge breakages, are the essential parameters to determining the failure modes.

This study is completely new in showing three distinct types of failure modes from a simplified single DEM model. As a future perspective, changing elastic properties such as the ratio between glass beads and polymer bonds would be a possible direction of interest, and it could alter the transition point of failure modes.

In Sec. 3.3, I then applied a machine learning methods, the random forest algorithm, to predict the failure timing of cohesive granular materials, for the various failure modes that I had previously identified. In Sec. 3.2, I had obtained time series of the dynamics of compression up to failure for five distinct realisations of each simulated particle density, with different initial configurations. I fed these data into the machine learning algorithm using four realisations as training data and one as test data and tried to predict a failure strain corresponding to the

maximum or peak value of stress. At higher densities, the actual time to failure and the predicted time to failure were in good agreement, but the prediction accuracy decreased as the density decreased (see Fig. 3.18). The results suggest a one-to-one correspondence between the stress value and time to failure for brittle failure at high densities, irrespective of the initial particle configurations–which is consistent with the well-defined critical strain of these systems [38]. On the other hand, in ductile and compacting failures, there are variations in the stress-strain curves depending on the initial configurations, so machine learning predictions with more realisations are needed to accurately predict the time to failure. In the process of these predictions, I extracted the feature importance for predictions. The essential features shifted from the absolute value of the stress to more subtle features like the stress variance and accumulated damage in the system, as the initial density of the system decreased (see Fig. 3.19).

Another new aspect of this work is the prediction of a failure timing of a cohesive granular system. Although these are preliminary results, efforts to improve predicting accuracy are anticipated as future directions. The process of this study is also important in the field of industry. For example, there are many cases where sufficient time series data cannot be obtained due to missing data. Even under such circumstances, the process of generating time-series data by numerical simulation with appropriate modelling is effective. Furthermore, if the important features for the prediction can be extracted appropriately, it is possible to identify the data that actually needs to be observed [197].

In Sec. 4.1, I turned to focus on the rheology of cohesive granular particles, and began simulating the granular flow of fine powders. In this chapter, the materials under study were connected by bonds that could break and reform easily, like van der Waals bonds or capillary bridges. Here, I performed MD simulations in 2D to investigate the effect of cohesion on rheology under constant pressure conditions. Depending on the confining pressure, the strength of the cohesive interactions between particles, and the shear velocity, I classified the large-scale phases of motion seen at steady states of shear deformation (see Fig. 4.7). At phases where uniform shear was stable for long simulations, the effect of cohesion could be integrated into the static friction coefficient, $\mu_c$, as shown in Fig. 4.9. I showed an anisotropy in the coordination number (Fig. 4.13) and inter-particle forces (Fig. 4.14) at higher cohesion. However, uniform shear could not be applied stably, at the system developed clustering phases (containing large 'rolling' clumps of particles that lubricated the system) and shear banding phases that appeared to be stable for very long simulation times (see Fig. 4.6). These inhomogeneous phases appeared only in the parameter regions where the cohesion was particularly strong.

Finally, in Sec. 4.2, I observed how the non-uniform shear deformation identified by 2D simulations could be extended into 3D simulations (see Fig. 4.19), and explored the effects of

dimensionality on the stability of shear flows in cohesive granular materials. In particular, I measured changes in physical quantities before and after the emergence of the clustering phase and detected dilatancy and significant changes in the shear stress and potential energy of the system that accompanied the onset of cluster formation, as shown in Fig. 4.21. Furthermore, I confirmed that the cluster formation process is history-dependent (Fig. 4.20) and that there is a critical nucleus size for the appearance of a void to act as the nucleation of a cluster formation (Fig. 4.22). In conclusion, in both 2D and 3D simulations, I could observe the non-uniform flow, which is intrinsic to cohesive system, under a shear deformation and constant confining pressure. I detected changes in the shear stress and potential energy of the system, accompanied by the emergence of the inhomogeneous phases.

This study is new in observing clustering and shear-banding induced by cohesion in both 2D and 3D by comprehensive parameter studies. Addressing a critical nuclei size in cohesive granular materials is also a novel approach. However, in this study, I could not reveal the physical background of how the voids can grow up into clustering, which would need further development to perfect. The essential difference between the formation of clustering and shear-banding is also a new research question.

In conclusion, in this thesis I have shown how it is possible to reproduce the emergent phenomena such as a shear-banding, a compaction banding, and a cluster formation in a minimal model of DEM and MD simulations by carefully introducing cohesive forces between particles, in ways that are quantitatively consistent with the expected or measured microscopic interactions between particles. Through these simulations, I could detect the key physical quantities that change dramatically before and after the emergent phenomena, which can be used as indicators of failure, or transitions between shear states. Furthermore, I showed the applicability of the model to a variety of physically different materials, such as brittle, ductile, low-density materials. I also showed that the model is valid to explore the critical parameters for the emergence of different phases, or failure modes.

# References


[1] Leonardo E Silbert, Deniz Ertaş, Gary S Grest, Thomas C Halsey, Dov Levine, and Steven J Plimpton. Granular flow down an inclined plane: Bagnold scaling and rheology. *Physical Review E*, 64(5):051302, 2001.

[2] GDR MiDi. On dense granular flows. *The European Physical Journal E*, 14(4):341–365, 2004.

[3] Pierre Jop, Yoël Forterre, and Olivier Pouliquen. A constitutive law for dense granular flows. *Nature*, 441(7094):727–730, 2006.

[4] Osborne Reynolds. LVII. On the dilatancy of media composed of rigid particles in contact. With experimental illustrations. *The London, Edinburgh, and Dublin Philosophical Magazine and Journal of Science*, 20(127):469–481, 1885.

[5] Robert P Behringer and Bulbul Chakraborty. The physics of jamming for granular materials: a review. *Reports on Progress in Physics*, 82(1):012601, 2018.

[6] Antonio Castellanos. The relationship between attractive interparticle forces and bulk behaviour in dry and uncharged fine powders. *Advances in Physics*, 54(4):263–376, 2005.

[7] Stefan Luding. Cohesive, frictional powders: contact models for tension. *Granular Matter*, 10(4):235, 2008.

[8] Jacob N Israelachvili. *Intermolecular and surface forces*. Academic press, 2015.

[9] JS Rowlinson and B Widom. *Molecular Theory of Capillarity*. Clarendon Press, Oxford University, 1982.

[10] Stephan Herminghaus. Dynamics of wet granular matter. *Advances in Physics*, 54(3):221–261, 2005.

[11] Stephan Herminghaus. *Wet Granular Matter: A Truly Complex Fluid*. World Scientific, 2013.

[12] Namiko Mitarai and Hiizu Nakanishi. Bagnold scaling, density plateau, and kinetic theory analysis of dense granular flow. *Physical Review Letters*, 94(12):128001, 2005.

[13] Namiko Mitarai and Franco Nori. Wet granular materials. *Advances in Physics*, 55(1-2):1–45, 2006.

[14] Namiko Mitarai and Hiizu Nakanishi. Simple model for wet granular materials with liquid clusters. *Europhysics Letters*, 88(6):64001, 2010.

[15] Adam J Forsyth, SR Hutton, Charles F Osborne, and Martin J Rhodes. Effects of interparticle force on the packing of spherical granular material. *Physical Review Letters*, 87(24):244301, 2001.

[16] Yeonsu Jung, Sohyun Jung, Wonjung Kim, Ho-Young Kim, et al. Avian mud nest architecture by self-secreted saliva. *Proceedings of the National Academy of Sciences*, 118(3), 2021.

[17] J Heierli, P Gumbsch, and M Zaiser. Anticrack nucleation as triggering mechanism for snow slab avalanches. *Science*, 321(5886):240–243, 2008.

[18] P. Arató, E. Besenyei, A. Kele, and F. Wéber. Mechanical properties in the initial stage of sintering. *Journal of Materials Science*, 30(7):1863–1871, apr 1995.

[19] Jack Dvorkin, Gary Mavko, and Amos Nur. The effect of cementation on the elastic properties of granular material. *Mechanics of Materials*, 12(3-4):207–217, 1991.

[20] Ekin Dogus Cubuk, RJS Ivancic, Samuel S Schoenholz, DJ Strickland, Anindita Basu, ZS Davidson, Julien Fontaine, Jyo Lyn Hor, Y-R Huang, Y Jiang, et al. Structure-property relationships from universal signatures of plasticity in disordered solids. *Science*, 358(6366):1033–1037, 2017.

[21] Matt Harrington and Douglas J Durian. Anisotropic particles strengthen granular pillars under compression. *Physical Review E*, 97(1):012904, 2018.

[22] D Lockner. The role of acoustic emission in the study of rock fracture. In *International Journal of Rock Mechanics and Mining Sciences & Geomechanics Abstracts*, volume 30, pages 883–899. Elsevier, 1993.

[23] Takayuki Hirata, Takashi Satoh, and Keisuke Ito. Fractal structure of spatial distribution of microfracturing in rock. *Geophysical Journal International*, 90(2):369–374, 1987.

[24] Niels Hansen and CY Barlow. Plastic deformation of metals and alloys. In *Physical Metallurgy*, pages 1681–1764. Elsevier, 2014.

[25] Raymond C Fletcher and David D Pollard. Anticrack model for pressure solution surfaces. *Geology*, 9(9):419–424, 1981.

[26] Kurt R Sternlof, John W Rudnicki, and David D Pollard. Anticrack inclusion model for compaction bands in sandstone. *Journal of Geophysical Research*, 110(B11), 2005.

[27] Hamid Roshan, Hossein Masoumi, Yihuai Zhang, Ahmed Zarzor Al-Yaseri, Stefan Iglauer, Maxim Lebedev, and Mohammad Sarmadivaleh. Microstructural effects on mechanical properties of shaly sandstone. *Journal of Geotechnical and Geoenvironmental Engineering*, 144(2):06017019, 2018.

[28] MS Paterson. Experimental deformation and faulting in Wombeyan marble. *Geological Society of America Bulletin*, 69(4):465–476, 1958.

[29] Thomas W Barraclough, Jane R Blackford, Stefan Liebenstein, Stefan Sandfeld, Tim J Stratford, Gerhard Weinländer, and Michael Zaiser. Propagating compaction bands in confined compression of snow. *Nature Physics*, 13(3):272–275, 2017.

[30] Ivan Iordanoff, Nicolas Fillot, and Yves Berthier. Numerical study of a thin layer of cohesive particles under plane shearing. *Powder Technology*, 159(1):46–54, 2005.

[31] E Schlangen and JGMi Van Mier. Experimental and numerical analysis of micromechanisms of fracture of cement-based composites. *Cement and Concrete Composites*, 14(2):105–118, 1992.

[32] Francois de Larrard and Albert Belloc. The influence of aggregate on the compressive strength of normal and high-strength concrete. *Materials Journal*, 94(5):417–426, 1997.

[33] IJ Merchant, Donald E Macphee, Howard William Chandler, and RJ Henderson. Toughening cement-based materials through the control of interfacial bonding. *Cement and Concrete Research*, 31(12):1873–1880, 2001.

[34] Edward J Tarbuck, Frederick K Lutgens, Dennis Tasa, and Dennis Tasa. *Earth: an introduction to physical geology*. Pearson Prentice Hall Upper Saddle River, 2005.

[35] A Benhamida, F Bouchelaghem, and H Dumontet. Effective properties of a cemented or an injected granular material. *International Journal for Numerical and Analytical Methods in Geomechanics*, 29(2):187–208, 2005.

[36] Jean-Yves Delenne, Moulay Saïd El Youssoufi, Fabien Cherblanc, and Jean-Claude Bénet. Mechanical behaviour and failure of cohesive granular materials. *International Journal for Numerical and Analytical Methods in Geomechanics*, 28(15):1577–1594, 2004.

[37] Jean-Yves Delenne, Vincent Topin, and Farhang Radjai. Failure of cemented granular materials under simple compression - Experiments and numerical simulations. *Acta Mechanica*, 205:9–21, 2009.

[38] Arnaud Hemmerle, Matthias Schröter, and Lucas Goehring. A cohesive granular material with tunable elasticity. *Scientific Reports*, 6(1):1–11, 2016.

[39] Alexander Schmeink, Lucas Goehring, and Arnaud Hemmerle. Fracture of a model cohesive granular material. *Soft Matter*, 13(5):1040–1047, 2017.

[40] Ferenc Kun, Imre Varga, Sabine Lennartz-Sassinek, and Ian G Main. Approach to failure in porous granular materials under compression. *Physical Review E*, 88(6):062207, 2013.

[41] Ferenc Kun, Imre Varga, Sabine Lennartz-Sassinek, and Ian G Main. Rupture cascades in a discrete element model of a porous sedimentary rock. *Physical Review Letters*, 112(6):065501, 2014.

[42] Frédéric Da Cruz, Sacha Emam, Michaël Prochnow, Jean-Noël Roux, and François Chevoir. Rheophysics of dense granular materials: Discrete simulation of plane shear flows. *Physical Review E*, 72(2):021309, 2005.

[43] Mehdi Bouzid, Martin Trulsson, Philippe Claudin, Eric Clément, and Bruno Andreotti. Nonlocal rheology of granular flows across yield conditions. *Physical Review Letters*, 111(23):238301, 2013.

[44] Mehdi Bouzid, Adrien Izzet, Martin Trulsson, Eric Clément, Philippe Claudin, and Bruno Andreotti. Non-local rheology in dense granular flows. *The European Physical Journal E*, 38(11):1–15, 2015.

[45] Ehsan Irani, Pinaki Chaudhuri, and Claus Heussinger. Impact of attractive interactions on the rheology of dense athermal particles. *Physical Review Letters*, 112(18):188303, 2014.

[46] Ehsan Irani, Pinaki Chaudhuri, and Claus Heussinger. Athermal rheology of weakly attractive soft particles. *Physical Review E*, 94(5):052608, 2016.

[47] Gregg Lois, Jerzy Blawzdziewicz, and Corey S O'Hern. Jamming transition and new percolation universality classes in particulate systems with attraction. *Physical Review Letters*, 100(2):028001, 2008.

[48] Pinaki Chaudhuri, Ludovic Berthier, and Lydéric Bocquet. Inhomogeneous shear flows in soft jammed materials with tunable attractive forces. *Physical Review E*, 85(2):021503, 2012.

[49] Lee Aarons and Sankaran Sundaresan. Shear flow of assemblies of cohesive and non-cohesive granular materials. *Powder Technology*, 169(1):10–21, 2006.

[50] Yile Gu, Sebastian Chialvo, and Sankaran Sundaresan. Rheology of cohesive granular materials across multiple dense-flow regimes. *Physical Review E*, 90(3):032206, 2014.

[51] PG Rognon, J-N Roux, D Wolf, M Naaïm, and F Chevoir. Rheophysics of cohesive granular materials. *Europhysics Letters*, 74(4):644, 2006.

[52] Abhinendra Singh, Vanessa Magnanimo, Kuniyasu Saitoh, and Stefan Luding. Effect of cohesion on shear banding in quasistatic granular materials. *Physical Review E*, 90(2):022202, 2014.

[53] Satoshi Takada, Kuniyasu Saitoh, and Hisao Hayakawa. Simulation of cohesive fine powders under a plane shear. *Physical Review E*, 90(6):062207, 2014.

[54] Zhuang Cheng and Jianfeng Wang. Estimation of contact forces of granular materials under uniaxial compression based on a machine learning model. *Granular Matter*, 24(1):1–14, 2022.

[55] Andreas Mayr, Sebastian Lehner, Arno Mayrhofer, Christoph Kloss, Sepp Hochreiter, and Johannes Brandstetter. Learning 3d granular flow simulations. *arXiv preprint arXiv:2105.01636*, 2021.

[56] Liqiang Lu, Xi Gao, Jean-François Dietiker, Mehrdad Shahnam, and William A Rogers. Machine learning accelerated discrete element modeling of granular flows. *Chemical Engineering Science*, 245:116832, 2021.

[57] Gang Ma, Jiangzhou Mei, Ke Gao, Jidong Zhao, Wei Zhou, and Di Wang. Machine learning bridges microslips and slip avalanches of sheared granular gouges. *Earth and Planetary Science Letters*, 579:117366, 2022.

[58] Bertrand Rouet-Leduc, Claudia Hulbert, Nicholas Lubbers, Kipton Barros, Colin J Humphreys, and Paul A Johnson. Machine learning predicts laboratory earthquakes. *Geophysical Research Letters*, 44(18):9276–9282, 2017.

[59] Christopher X Ren, Omid Dorostkar, Bertrand Rouet-Leduc, Claudia Hulbert, Dominik Strebel, Robert A Guyer, Paul A Johnson, and Jan Carmeliet. Machine learning reveals the state of intermittent frictional dynamics in a sheared granular fault. *Geophysical Research Letters*, 46(13):7395–7403, 2019.

[60] P. A. Cundall and O. D. L. Strack. A discrete numerical model for granular assemblies. *Géotechnique*, 29(1):47–65, 1979.

[61] Dennis C Rapaport. *The art of molecular dynamics simulation*. Cambridge University Press, 2004.

[62] Thorsten Pöschel and Thomas Schwager. *Computational granular dynamics: models and algorithms*. Springer Science & Business Media, 2005.

[63] Denis J Evans and Gary P Morriss. *Statistical mechanics of nonequilbrium liquids*. ANU Press, 2007.

[64] Lanru Jing and Ove Stephansson. *Fundamentals of discrete element methods for rock engineering: theory and applications*. Elsevier, 2007.

[65] Michael P Allen and Dominic J Tildesley. *Computer simulation of liquids*. Oxford University Press, 2017.

[66] Andrés A Peña, Sean McNamara, Pedro G Lind, and Hans J Herrmann. Avalanches in anisotropic sheared granular media. *Granular Matter*, 11(4):243–252, 2009.

[67] Frederick M Chester, James P Evans, and Ronald L Biegel. Internal structure and weakening mechanisms of the San Andreas fault. *Journal of Geophysical Research: Solid Earth*, 98(B1):771–786, 1993.

[68] Renée Heilbronner and Nynke Keulen. Grain size and grain shape analysis of fault rocks. *Tectonophysics*, 427(1-4):199–216, 2006.

[69] Kuo-Fong Ma, Hidemi Tanaka, Sheng-Rong Song, Chien-Ying Wang, Jih-Hao Hung, Yi-Ben Tsai, Jim Mori, Yen-Fang Song, Eh-Chao Yeh, Wonn Soh, et al. Slip zone and energetics of a large earthquake from the Taiwan Chelungpu-fault Drilling Project. *Nature*, 444(7118):473–476, 2006.

[70] Paul W Cleary and Mark L Sawley. DEM modelling of industrial granular flows: 3D case studies and the effect of particle shape on hopper discharge. *Applied Mathematical Modelling*, 26(2):89–111, 2002.

[71] Paul W Cleary. Large scale industrial dem modelling. *Engineering Computations*, 2004.

[72] Mikio Sakai and Seiichi Koshizuka. Large-scale discrete element modeling in pneumatic conveying. *Chemical Engineering Science*, 64(3):533–539, 2009.

[73] Fatih Göncü and Stefan Luding. Effect of particle friction and polydispersity on the macroscopic stress–strain relations of granular materials. *Acta Geotechnica*, 8(6):629–643, 2013.

[74] Patrick Mutabaruka, Mahdi Taiebat, Roland J-M Pellenq, and Farhang Radjai. Effects of size polydispersity on random close-packed configurations of spherical particles. *Physical Review E*, 100(4):042906, 2019.

[75] Urs Gasser, Eric R Weeks, Andrew Schofield, PN Pusey, and DA Weitz. Real-space imaging of nucleation and growth in colloidal crystallization. *Science*, 292(5515):258–262, 2001.

[76] Vikram Prasad, Denis Semwogerere, and Eric R Weeks. Confocal microscopy of colloids. *Journal of Physics: Condensed Matter*, 19(11):113102, 2007.

[77] John Edward Jones. On the determination of molecular fields.—I. From the variation of the viscosity of a gas with temperature. *Proceedings of the Royal Society of London. Series A, Containing Papers of a Mathematical and Physical Character*, 106(738):441–462, 1924.

[78] John Edward Jones. On the determination of molecular fields.—II. From the equation of state of a gas. *Proceedings of the Royal Society of London. Series A, Containing Papers of a Mathematical and Physical Character*, 106(738):463–477, 1924.

[79] John E Lennard-Jones. Cohesion. *Proceedings of the Physical Society (1926-1948)*, 43(5):461, 1931.

[80] Philip M Morse. Diatomic molecules according to the wave mechanics. II. Vibrational levels. *Physical Review*, 34(1):57, 1929.

[81] Boris V Derjaguin, Vladimir M Muller, and Yu P Toporov. Effect of contact deformations on the adhesion of particles. *Journal of Colloid and Interface Science*, 53(2):314–326, 1975.

[82] VM Muller, BV Derjaguin, and Yu P Toporov. On two methods of calculation of the force of sticking of an elastic sphere to a rigid plane. *Colloids and Surfaces*, 7(3):251–259, 1983.

[83] Kenneth Langstreth Johnson, Kevin Kendall, and A. D. Roberts. Surface energy and the contact of elastic solids. *Proceedings of the Royal Society of London. A. Mathematical and Physical Sciences*, 324(1558):301–313, 1971.

[84] Heinrich Hertz. On the contact of elastic solids. *The Journal für die Reine und Angewandte Mathematik*, 92:156–171, 1881.

[85] J Coaplen, WJ Stronge, and B Ravani. Work equivalent composite coefficient of restitution. *International Journal of Impact Engineering*, 30(6):581–591, 2004.

[86] Kuanmin Mao, Michael Yu Wang, Zhiwei Xu, and Tianning Chen. Simulation and characterization of particle damping in transient vibrations. *The Journal of Vibration and Acoustics*, 126(2):202–211, 2004.

[87] CX Wong, MC Daniel, and JA Rongong. Energy dissipation prediction of particle dampers. *Journal of Sound and Vibration*, 319(1-2):91–118, 2009.

[88] T Kawaguchi. Numerical simulation of fluidized bed using the discrete element method. *Transactions of the Japan Society of Mechanical Engineers Series B*, 58:79–85, 1992.

[89] Christian Jakob and H Konietzky. Particle methods. *An Overview Freiberg*, 24, 2012.

[90] Raehee Han, Takehiro Hirose, Toshihiko Shimamoto, Youngmin Lee, and Jun-ichi Ando. Granular nanoparticles lubricate faults during seismic slip. *Geology*, 39(6):599–602, 2011.

[91] AW Lees and SF Edwards. The computer study of transport processes under extreme conditions. *Journal of Physics C: Solid State Physics*, 5(15):1921, 1972.

[92] Yuliang Jin and Hernán A Makse. A first-order phase transition defines the random close packing of hard spheres. *Physica A: Statistical Mechanics and its Applications*, 389(23):5362–5379, 2010.

[93] Frank Rietz, Charles Radin, Harry L Swinney, and Matthias Schröter. Nucleation in sheared granular matter. *Physical Review Letters*, 120(5):055701, 2018.

[94] M Abdel-Ghani, JG Petrie, JPK Seville, R Clift, and MJ Adams. Mechanical properties of cohesive particulate solids. *Powder Technology*, 65(1-3):113–123, 1991.

[95] Renwei Mei, Hong Shang, Otis R Walton, and James F Klausner. Concentration non-uniformity in simple shear flow of cohesive powders. *Powder Technology*, 112(1-2):102–110, 2000.

[96] AS Clarke and JD Wiley. Numerical simulation of the dense random packing of a binary mixture of hard spheres: Amorphous metals. *Physical Review B*, 35(14):7350, 1987.

[97] Andrew S Clarke and Hannes Jónsson. Structural changes accompanying densification of random hard-sphere packings. *Physical Review E*, 47(6):3975, 1993.

[98] MR Hoare. Packing models and structural specificity. *Journal of Non-Crystalline Solids*, 31(1-2):157–179, 1978.

[99] Augustin Cauchy. Méthode générale pour la résolution des systemes d'équations simultanées. *Comptes Rendus Hebdomadaires des Séances de l'Académie des Sciences*, 25(1847):536–538, 1847.

[100] Jonathan Richard Shewchuk. An introduction to the conjugate gradient method without the agonizing pain, 1994.

[101] KL Mills, Xiaoyue Zhu, Shuichi Takayama, and MD Thouless. The mechanical properties of a surface-modified layer on polydimethylsiloxane. *Journal of Materials Research*, 23(1):37, 2008.

[102] J Chopin, A Prevost, A Boudaoud, and M Adda-Bedia. Crack front dynamics across a single heterogeneity. *Physical Review Letters*, 107(14):144301, 2011.

[103] Herman Heine Goldstine. *A History of Numerical Analysis from the 16th through the 19th Century*, volume 2. Springer Science & Business Media, 2012.

[104] C William Gear. Numerical initial value problems in ordinary differential equations. *Prentice-Hall Series in Automatic Computation*, 1971.

[105] Loup Verlet. Computer "experiments" on classical fluids. I. Thermodynamical properties of Lennard-Jones molecules. *Physical Review*, 159(1):98, 1967.

[106] Daan Frenkel, Berend Smit, Jan Tobochnik, Susan R McKay, and Wolfgang Christian. Understanding molecular simulation. *Computers in Physics*, 11(4):351–354, 1997.

[107] Arnaud Hemmerle, Yuta Yamaguchi, Marcin Makowski, Oliver Bäumchen, and Lucas Goehring. Measuring and upscaling micromechanical interactions in a cohesive granular material. *Soft Matter*, 17(23):5806–5814, 2021.

[108] Yuta Yamaguchi, Soumyajyoti Biswas, Takahiro Hatano, and Lucas Goehring. Failure processes of cemented granular materials. *Physical Review E*, 102:052903, Nov 2020.

[109] A Neveu, R Artoni, P Richard, and Y Descantes. Fracture of granular materials composed of arbitrary grain shapes: A new cohesive interaction model. *Journal of the Mechanics and Physics of Solids*, 95:308–319, 2016.

[110] Johan Gaume, Henning Löwe, Shurun Tan, and Leung Tsang. Scaling laws for the mechanics of loose and cohesive granular materials based on baxter's sticky hard spheres. *Physical Review E*, 96(3):032914, 2017.

[111] Yuta Yamaguchi, Satoshi Takada, and Takahiro Hatano. Rheology of cohesive granular particles under constant pressure. *Journal of the Physical Society of Japan*, 87(9):094802, 2018.

[112] Misaki Ozawa, Ludovic Berthier, Giulio Biroli, Alberto Rosso, and Gilles Tarjus. Random critical point separates brittle and ductile yielding transitions in amorphous materials. *Proceedings of the National Academy of Sciences*, 115(26):6656–6661, 2018.

[113] Jialiang Wang, Baoguo Han, Zhen Li, Xun Yu, and Xufeng Dong. Effect investigation of nanofillers on csh gel structure with si nmr. *Journal of Materials in Civil Engineering*, 31(1):04018352, 2019.

[114] Ashivni Shekhawat, Stefano Zapperi, and James P. Sethna. From damage percolation to crack nucleation through finite size criticality. *Physical Review Letters*, 110:185505, 2013.

[115] Michelle M. Driscoll, Bryan Gin-ge Chen, Thomas H. Beuman, Stephan Ulrich, Sidney R. Nagel, and Vincenzo Vitelli. The role of rigidity in controlling material failure. *Proceedings of the National Academy of Sciences*, 113(39):10813–10817, September 2016.

[116] Estelle Berthier, Jonathan E. Kollmer, Silke E. Henkes, Kuang Liu, J. M. Schwarz, and Karen E. Daniels. Rigidity percolation control of the brittle-ductile transition in disordered networks. *Physical Review Materials*, 3(7):075602, July 2019.

[117] Shehla Arif, Jih-Chiang Tsai, and Sascha Hilgenfeldt. Spontaneous Brittle-to-Ductile Transition in Aqueous Foam. *Journal of Rheology*, 56(3):485–499, May 2012.

[118] Wenbin Li, Jennifer M. Rieser, Andrea J. Liu, Douglas J. Durian, and Ju Li. Deformation-driven diffusion and plastic flow in amorphous granular pillars. *Physical Review E*, 91(6):062212, June 2015.

[119] L. Jing. A review of techniques, advances and outstanding issues in numerical modelling for rock mechanics and rock engineering. *International Journal of Rock Mechanics and Mining Sciences*, 40(3):283–353, April 2003.

[120] W A Olsson and D J Holcomb. Compaction localization in porous rock. *Geophysical Research Letters*, 27(21):3537–3540, 2000.

[121] Patrick Baud, Emmanuelle Klein, and Teng-fong Wong. Compaction localization in porous sandstones: spatial evolution of damage and acoustic emission activity. *Journal of Structural Geology*, 26(4):603–624, 2004.

[122] Edward Townend, Ben D. Thompson, Philip M. Benson, Philip G. Meredith, Patrick Baud, and R. Paul Young. Imaging compaction band propagation in Diemelstadt sandstone using acoustic emission locations. *Geophysical Research Letters*, 35:L15301, 2008.

[123] Pedro M Reis, F Corson, A Boudaoud, and B Roman. Localization through surface folding in solid foams under compression. *Physical Review Letters*, 103(4):045501, 2009.

[124] Mingjing Jiang, Wangcheng Zhang, Yugang Sun, and Stefano Utili. An investigation on loose cemented granular materials via DEM analyses. *Granular Matter*, 15(1):65–84, February 2013.

[125] Mingjing Jiang, Zhifu Shen, and Jianfeng Wang. A novel three-dimensional contact model for granulates incorporating rolling and twisting resistances. *Computers and Geotechnics*, 65:147–163, 2015.

[126] Matilda Backholm and Oliver Bäumchen. Micropipette force sensors for in vivo force measurements on single cells and multicellular microorganisms. *Nature Protocols*, 14(2):594–615, February 2019.

[127] Angelina Müller, Matthias C. Wapler, and Ulrike Wallrabe. A quick and accurate method to determine the poisson's ratio and the coefficient of thermal expansion of pdms. *Soft Matter*, 15:779–784, 2019.

[128] Robyn H. Pritchard, Pascal Lava, Dimitri Debruyne, and Eugene M. Terentjev. Precise determination of the poisson ratio in soft materials with 2d digital image correlation. *Soft Matter*, 9:6037–6045, 2013.

[129] L Brendel, J Török, R Kirsch, and U Bröckel. A contact model for the yielding of caked granular materials. *Granular Matter*, 13(6):777–786, 2011.

[130] F. A. Gilabert, J.-N. Roux, and A. Castellanos. Computer simulation of model cohesive powders: Plastic consolidation, structural changes, and elasticity under isotropic loads. *Physical Review E*, 78:031305, 2008.

[131] Patrick Baud, Teng-Fong Wong, and Wei Zhu. Effects of porosity and crack density on the compressive strength of rocks. *International Journal of Rock Mechanics and Mining Sciences*, 67:202–211, 2014.

[132] Saikat Roy and Mahesh S. Tirumkudulu. Yielding in a strongly aggregated colloidal gel. Part I: 2D simulations. *Journal of Rheology*, 60:559, 2016.

[133] Jessica McBeck, Karen Mair, and François Renard. How porosity controls macroscopic failure via propagating fractures and percolating force chains in porous granular rocks. *Journal of Geophysical Research: Solid Earth*, 124(9):9920–9939, 2019.

[134] I Penskiy, A P Gerratt, and S Bergbreiter. Friction, adhesion and wear properties of PDMS films on silicon sidewalls. *Journal of Micromechanics and Microengineering*, 21(10):105013, sep 2011.

[135] Gergő Pál, Zoltán Jánosi, Ferenc Kun, and Ian G Main. Fragmentation and shear band formation by slow compression of brittle porous media. *Physical Review E*, 94(5):053003, 2016.

[136] G. E. P. Box and Mervin E. Muller. A note on the generation of random normal deviates. *Annals of Mathematical Statistics*, 29(2):610–611, June 1958.

[137] B Lawn. *Fracture of brittle solids*. Cambridge University Press, 1993.

[138] David Amitrano, Jean-Robert Grasso, and Didier Hantz. From diffuse to localised damage through elastic interaction. *Geophysical Research Letters*, 26(14):2109–2112, 1999.

[139] DiA Lockner, J. D Byerlee, V Kuksenko, A Ponomarev, and A Sidorin. Quasi-static fault growth and shear fracture energy in granite. *Nature*, 350(6313):39–42, 1991.

[140] P. R. Sammonds, P. G. Meredith, and I. G. Main. Role of pore fluid in the generation of seismic precursors to shear failure. *Nature*, 359:228–230, 1992.

[141] Arno Zang, F Christian Wagner, Sergei Stanchits, Christoph Janssen, and Georg Dresen. Fracture process zone in granite. *Journal of Geophysical Research*, 105(B10):23651–23661, 2000.

[142] Jérôme Fortin, Sergei Stanchits, Georg Dresen, and Yves Guéguen. Acoustic emission and velocities associated with the formation of compaction bands in sandstone. *Journal of Geophysical Research*, 111(B10), 2006.

[143] François Renard, Dominique Bernard, Jacques Desrues, and Audrey Ougier-Simonin. 3D imaging of fracture propagation using synchrotron X-ray microtomography. *Earth and Planetary Science Letters*, 286(1-2):285–291, 2009.

[144] François Renard, Jérôme Weiss, Joachim Mathiesen, Yehuda Ben-Zion, Neelima Kandula, and Benoît Cordonnier. Critical evolution of damage toward system-size failure in crystalline rock. *Journal of Geophysical Research*, 123(2):1969–1986, 2018.

[145] Eduard Ilin, Yaofa Li, Eugene V Colla, Kenneth T Christensen, Muhammad Sahimi, Maxim Marchevsky, Scott M Frailey, and Alexey Bezryadin. Nanoscale detection of metastable states in porous and granular media. *Journal of Applied Physics*, 127(2):024901, 2020.

[146] Pedro O Castillo-Villa, Jordi Baró, Antoni Planes, Ekhard K H Salje, Pathikumar Sellappan, Waltraud M Kriven, and Eduard Vives. Crackling noise during failure of alumina under compression: the effect of porosity. *Journal of Physics: Condensed Matter*, 25(29):292202, 2013.

[147] E K H Salje, G I Lampronti, D E Soto-Parra, J Baró, A Planes, and E Vives. Noise of collapsing minerals: Predictability of the compressional failure in goethite mines. *American Mineralogist*, 98:609, 2013.

[148] Th V Karman. Festigkeitsversuche unter allseitigem Drunk. *Z. Ver. Deu. Ing.*, 55:1749, 1911.

[149] H. C. Heard. Transition from brittle fracture to ductile flow in Solenhofen limestone as a function of temperature, confining pressure, and interstitial fluid pressure. *Geological Society of America*, 79:193–226, 1960.

[150] John Handin and Rex V Hager Jr. Experimental deformation of sedimentary rocks under confining pressure: Tests at room temperature on dry samples. *The American Association of Petroleum Geologists Bulletin*, 41(1):1–50, 1957.

[151] John Handin, Rex V Hager Jr., Melvin Friedman, and James N Feather. Experimental deformation of sedimentary rocks under confining pressure: pore pressure tests. *The American Association of Petroleum Geologists Bulletin*, 47(5):717–755, 1963.

[152] L. H. Robinson. The effect of pore and confining pressure on the failure process in sedimentary rock. In *The 3rd US Symposium on Rock Mechanics*. American Rock Mechanics Association, 1959.

[153] D Tönnies, R Maaß, and C A Volkert. Room temperature homogeneous ductility of micrometer-sized metallic glass. *Advanced Materials*, 26:5715, 2014.

[154] C A Volkert and E T Lilleodden. Size effects in the deformation of sub-micron Au columns. *Philosophical Magazine A*, 86:5567, 2006.

[155] Robin Eugene Hill. Analysis of deformation bands in the Aztec sandstone, Valley of Fire State Park, Nevada. Master's thesis, University of Nevada, Las Vegas, 1989.

[156] P N Mollema and M A Antonellini. Compaction bands: a structural analog for anti-mode I cracks in aeolian sandstone. *Tectonophysics*, 267(1-4):209–228, 1996.

[157] Peter Eichhubl, John N Hooker, and Stephen E Laubach. Pure and shear-enhanced compaction bands in Aztec Sandstone. *Journal of Structural Geology*, 32(12):1873–1886, 2010.

[158] Richard A Schultz, Chris H Okubo, and Haakon Fossen. Porosity and grain size controls on compaction band formation in Jurassic Navajo Sandstone. *Geophysical Research Letters*, 37(22), 2010.

[159] Haakon Fossen, Richard A Schultz, and Anita Torabi. Conditions and implications for compaction band formation in the Navajo Sandstone, Utah. *Journal of Structural Geology*, 33(10):1477–1490, 2011.

[160] William A Olsson. Theoretical and experimental investigation of compaction bands in porous rock. *Journal of Geophysical Research*, 104(B4):7219–7228, 1999.

[161] Kathleen A Issen and John W Rudnicki. Conditions for compaction bands in porous rock. *Journal of Geophysical Research*, 105(B9):21529–21536, 2000.

[162] Teng-fong Wong, Patrick Baud, and Emmanuelle Klein. Localized failure modes in a compactant porous rock. *Geophysical Research Letters*, 28(13):2521–2524, 2001.

[163] Patrick Baud, Philip Meredith, and Edward Townend. Permeability evolution during triaxial compaction of an anisotropic porous sandstone. *Journal of Geophysical Research*, 117(B5), 2012.

[164] R Katsman, E Aharonov, and H Scher. Numerical simulation of compaction bands in high-porosity sedimentary rock. *Mechanics of Materials*, 37(1):143–162, 2005.

[165] G Marketos and M D Bolton. Compaction bands simulated in discrete element models. *Journal of Structural Geology*, 31(5):479–490, 2009.

[166] Seiiti Kinosita. Compression of snow at constant speed. *Physics of Snow and Ice : Proceedings*, 1(2):911–927, 1967.

[167] K. R. Sternlof, M. Karimi-Fard, D. D. Pollard, and L. J. Durlofsky. Flow and transport effects of compaction bands in sandstone at scales relevant to aquifer and reservoir management. *Water Resources Research*, 42(7):W07425, 2006.

[168] Kevin Kendall, N McN Alford, and James Derek Birchall. Elasticity of particle assemblies as a measure of the surface energy of solids. *Proceedings of the Royal Society of London. A. Mathematical and Physical Sciences*, 412(1843):269–283, 1987.

[169] Kevin Kendall and Carl Stainton. Adhesion and aggregation of fine particles. *Powder Technology*, 121:223–229, 2001.

[170] Wei-Heng Shih, Wan Y. Shih, Seong-Il Kim, Jun Liu, and Ilhan A. Aksay. Scaling behavior of the elastic properties of colloidal gels. *Physical Review A*, 42:4772–4779, 1990.

[171] Jan Mewis and Norman J Wagner. *Colloidal suspension rheology*. Cambridge University Press, 2012.

[172] K. Walton. The effective elastic moduli of a random packing of spheres. *Journal of the Mechanics and Physics of Solids*, 35:213–216, 1987.

[173] Martin P.J. Schöpfer, Steffen Abe, Conrad Childs, and John J. Walsh. The impact of porosity and crack density on the elasticity, strength and friction of cohesive granular materials: Insights from DEM modelling. *International Journal of Rock Mechanics and Mining Sciences*, 46:250–261, 2009.

[174] C. G. Sammis and M. F. Ashby. The failure of brittle porous solids under compressive stress states. *Acta Metallurgica*, 34(3):511–526, 1986.

[175] Alexis Cartwright-Taylor, Maria-Daphne Mangriotis, Ian Main, Ian B Butler, Florian Fusseis, Martin Ling, Edward Ando, Andrew Curtis, Andrew Bell, Alyssa Crippen, et al. Seismic events miss important grain-scale mechanisms governed by kinematics during shear failure of porous rock. 2021.

[176] Angel Garcimartin, Alessio Guarino, Ludovic Bellon, and Sergio Ciliberto. Statistical properties of fracture precursors. *Physical Review Letters*, 79(17):3202, 1997.

[177] A Guarino, A Garcimartin, and S Ciliberto. An experimental test of the critical behaviour of fracture precursors. *The European Physical Journal B*, 6(1):13–24, 1998.

[178] C. Lu, Y.-W. Mai, and H. Xie. A sudden drop of fractal dimension: a likely precursor of catastrophic failure in disordered media. *Philosophical Magazine Letters*, 85(1):33–40, 2005.

[179] F Reurings and MJ Alava. Damage growth in random fuse networks. *The European Physical Journal B*, 47(1):85–91, 2005.

[180] T Matcharashvili, T Cheldize, J Gogiashvili, and Z Tsertsvadze. Difference in dynamics of distribution and variation of nonlinear correlations in earthquakes temporal, spatial and energetic domains. *Journal of Georgian Geophysical Society A*, 7:39–44, 2002.

[181] L Telesca, V Lapenna, and M Lovallo. Information entropy analysis of seismicity of Umbria-Marche region (Central Italy). *Natural Hazards and Earth System Sciences*, 4:691–695, 2004.

[182] Simanchal Padhy. Intermittent criticality on a regional scale in Bhuj. *Geophysical Journal International*, 158(2):676–680, 2004.

[183] Angelo De Santis, Gianfranco Cianchini, Paolo Favali, Laura Beranzoli, and Enzo Boschi. The Gutenberg–Richter law and entropy of earthquakes: two case studies in Central Italy. *Bulletin of the Seismological Society of America*, 101(3):1386–1395, 2011.

[184] G Bressan, C Barnaba, S Gentili, and G Rossi. Information entropy of earthquake populations in northeastern Italy and western Slovenia. *Physics of the Earth and Planetary Interiors*, 271:29–46, 2017.

[185] G Voronoi. New parametric applications concerning the theory of quadratic forms-second announcement. *The Journal für die Reine und Angewandte Mathematik*, 134:198–287, 1908.

[186] Tomaso Aste, T Di Matteo, Mohammad Saadatfar, Tim J Senden, Matthias Schröter, and Harry L Swinney. An invariant distribution in static granular media. *Europhysics Letters*, 79(2):24003, 2007.

[187] Chris Rycroft. Voro++: A three-dimensional voronoi cell library in c++. Technical report, Lawrence Berkeley National Lab.(LBNL), Berkeley, CA (United States), 2009.

[188] Teng-fong Wong and Patrick Baud. The brittle-ductile transition in porous rock: A review. *Journal of Structural Geology*, 44:25–53, 2012.

[189] Patrick Baud, Veronika Vajdova, and Teng-Fong Wong. Shear-enhanced compaction and strain localization: Inelastic deformation and constitutive modeling of four porous sandstones. *Journal of Geophysical Research*, 111:B12401, 2006.

[190] Leo Breiman. Random forests. *Machine Learning*, 45(1):5–32, 2001.

[191] Rafik Affes, J-Y Delenne, Yann Monerie, Farhang Radjai, and Vincent Topin. Tensile strength and fracture of cemented granular aggregates. *The European Physical Journal E*, 35(11):117, 2012.

[192] JD Birchall, AJ Howard, and K Kendall. Flexural strength and porosity of cements. *Nature*, 289(5796):388–390, 1981.

[193] Jerome H Friedman. *The elements of statistical learning: Data mining, inference, and prediction*. springer open, 2017.

[194] Soumyajyoti Biswas et al. Prediction of imminent failure using supervised learning in fiber bundle model. *arXiv preprint arXiv:2111.09713*, 2021.

[195] Fabian Pedregosa, Gaël Varoquaux, Alexandre Gramfort, Vincent Michel, Bertrand Thirion, Olivier Grisel, Mathieu Blondel, Peter Prettenhofer, Ron Weiss, Vincent Dubourg, et al. Scikit-learn: Machine learning in python. *the Journal of Machine Learning Research*, 12:2825–2830, 2011.

[196] Niko Speybroeck. Classification and regression trees. *International journal of public health*, 57(1):243–246, 2012.

[197] Soumyajyoti Biswas et al. Prediction of imminent failure using supervised learning in a fiber bundle model. *Physical Review E*, 106(2):025003, 2022.

[198] Jérémie Vasseur, Fabian B Wadsworth, Yan Lavallée, Andrew F Bell, Ian G Main, and Donald B Dingwell. Heterogeneity: the key to failure forecasting. *Scientific Reports*, 5(1):1–7, 2015.

[199] Takahiro Hatano. Power-law friction in closely packed granular materials. *Physical Review E*, 75(6):060301, 2007.

[200] Peter Olsson and Stephen Teitel. Critical scaling of shear viscosity at the jamming transition. *Physical Review Letters*, 99(17):178001, 2007.

[201] Ralph Alger Bagnold. Experiments on a gravity-free dispersion of large solid spheres in a Newtonian fluid under shear. *Proceedings of the Royal Society of London. Series A. Mathematical and Physical Sciences*, 225(1160):49–63, 1954.

[202] J Javier Brey, James W Dufty, Chang Sub Kim, and Andrés Santos. Hydrodynamics for granular flow at low density. *Physical Review E*, 58(4):4638, 1998.

[203] V Garzó and JW Dufty. Dense fluid transport for inelastic hard spheres. *Physical Review E*, 59(5):5895, 1999.

[204] Vicente Garzó and José María Montanero. Shear viscosity for a moderately dense granular binary mixture. *Physical Review E*, 68(4):041302, 2003.

[205] Nikolai V Brilliantov and Thorsten Pöschel. *Kinetic theory of granular gases*. Oxford University Press on Demand, 2004.

[206] James F Lutsko. Transport properties of dense dissipative hard-sphere fluids for arbitrary energy loss models. *Physical Review E*, 72(2):021306, 2005.

[207] Vicente Garzó, James W Dufty, and Christine M Hrenya. Enskog theory for polydisperse granular mixtures. I. Navier-Stokes order transport. *Physical Review E*, 76(3):031303, 2007.

[208] Vicente Garzó, Christine M Hrenya, and James W Dufty. Enskog theory for polydisperse granular mixtures. II. Sonine polynomial approximation. *Physical Review E*, 76(3):031304, 2007.

[209] Namiko Mitarai and Hiizu Nakanishi. Velocity correlations in dense granular shear flows: Effects on energy dissipation and normal stress. *Physical Review E*, 75(3):031305, 2007.

[210] Sebastian Chialvo and Sankaran Sundaresan. A modified kinetic theory for frictional granular flows in dense and dilute regimes. *Physics of Fluids*, 25(7):070603, 2013.

[211] E DeGiuli, G Düring, E Lerner, and M Wyart. Unified theory of inertial granular flows and non-brownian suspensions. *Physical Review E*, 91(6):062206, 2015.

[212] E DeGiuli, JN McElwaine, and M Wyart. Phase diagram for inertial granular flows. *Physical Review E*, 94(1):012904, 2016.

[213] Thomas Barker, DG Schaeffer, Michael Shearer, and JMNT Gray. Well-posed continuum equations for granular flow with compressibility and $\mu$ (I)-rheology. *Proceedings of the Royal Society A: Mathematical, Physical and Engineering Sciences*, 473(2201):20160846, 2017.

[214] Richard H Heist and Honghai He. Review of vapor to liquid homogeneous nucleation experiments from 1968 to 1992. *Journal of Physical and Chemical Reference Data*, 23(5):781–805, 1994.

[215] R Strey, PE Wagner, and Y Viisanen. The problem of measuring homogeneous nucleation rates and the molecular contents of nuclei: Progress in the form of nucleation pulse measurements. *The Journal of Physical Chemistry*, 98(32):7748–7758, 1994.

[216] Kenji Yasuoka and Mitsuhiro Matsumoto. Molecular dynamics of homogeneous nucleation in the vapor phase. I. Lennard-Jones fluid. *The Journal of Chemical Physics*, 109(19):8451–8462, 1998.

[217] Kuniyasu Saitoh, Satoshi Takada, and Hisao Hayakawa. Hydrodynamic instabilities in shear flows of dry cohesive granular particles. *Soft Matter*, 11(32):6371–6385, 2015.

[218] Micha-Klaus Müller and Stefan Luding. Homogeneous cooling with repulsive and attractive long-range potentials. *Mathematical Modelling of Natural Phenomena*, 6(4):118–150, 2011.

[219] Eric Murphy and Shankar Subramaniam. Freely cooling granular gases with short-ranged attractive potentials. *Physics of Fluids*, 27(4):043301, 2015.

[220] Satoshi Takada, Kuniyasu Saitoh, and Hisao Hayakawa. Kinetic theory for dilute cohesive granular gases with a square well potential. *Physical Review E*, 94(1):012906, 2016.

[221] TS Majmudar, M Sperl, Stefan Luding, and Robert P Behringer. Jamming transition in granular systems. *Physical Review Letters*, 98(5):058001, 2007.

[222] Dimo Kashchiev. *Nucleation*. Elsevier, 2000.

[223] E Smith and JT Barnby. Crack nucleation in crystalline solids. *Metal Science Journal*, 1(1):56–64, 1967.